Development of an Aeroservoelastic Research Platform

From Concept to Final Product

R.R.M. Schildkamp

Delft University of Technology

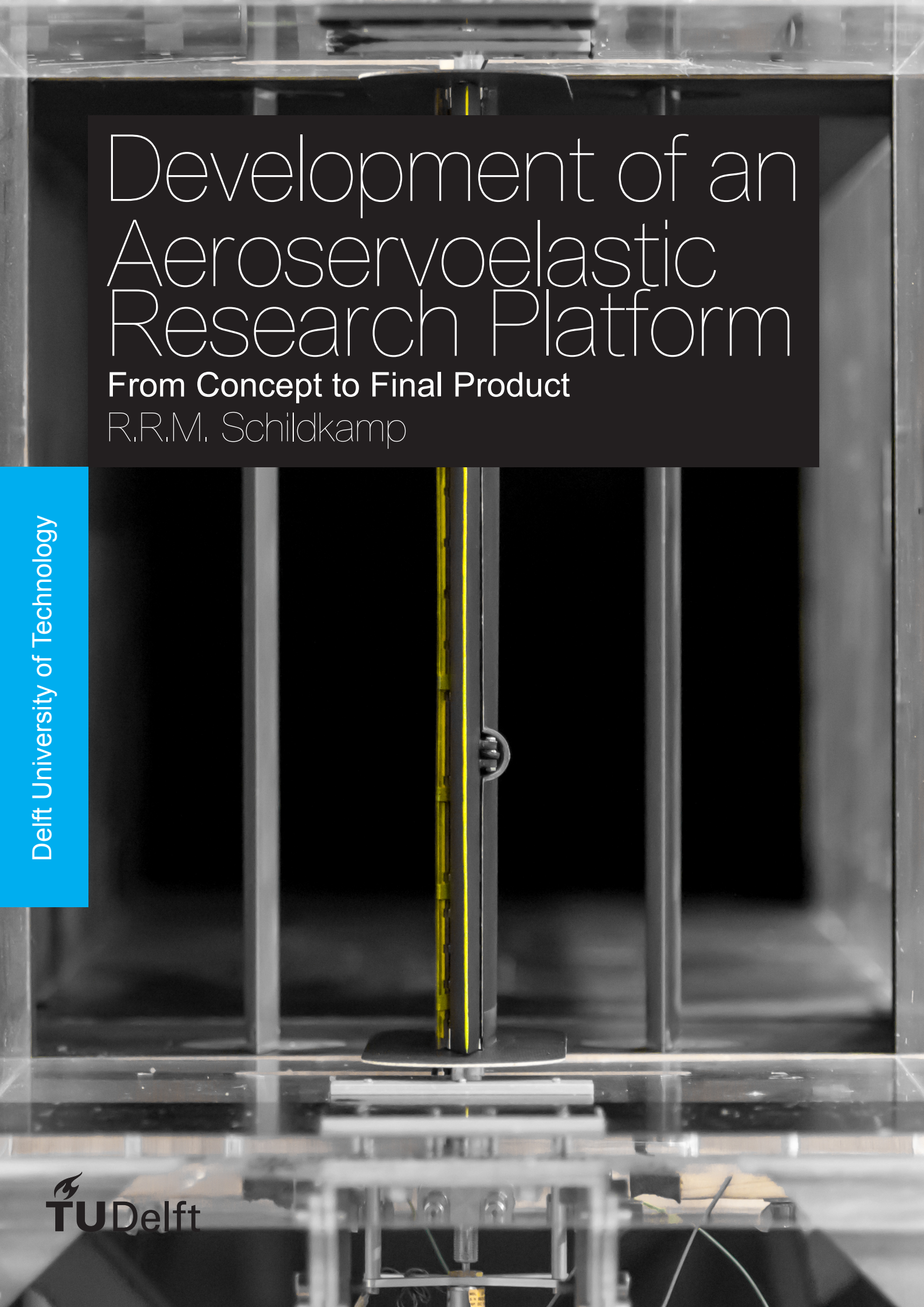

TU Delft

This page is intentionally left blank.

Development of an Aeroservoelastic Research Platform

From Concept to Final Product

by

R.R.M. Schildkamp

to obtain the degree of Master of Science
at the Delft University of Technology,
to be defended publicly on Thursday January 27, 2022 at 14:00.

Student number: 4079663
Project duration: January 1, 2021 – January 27, 2022
Thesis committee:

Dr.ir. R. De Breuker,	TU Delft, chairman
Dr. J. Sodja,	TU Delft, supervisor
Prof.dr.ing. G. Eitelberg,	TU Delft
X. Wang,	TU Delft

TU Delft

This page is intentionally left blank.

Preface

This work is the product of a long journey that started many, many years ago. A journey that started out as a “Plan B” for a high school student who actually wanted to fly. However, as time progressed, I started to enjoy and appreciate the field of aerospace engineering more and more. This “Plan B” has brought me to many aerospace related placed across the western world, meeting dedicated and inspiring people everywhere I went. I was fortunate enough to be granted the opportunity to work on manufacturing of a small sports aircraft and to intern at Lockheed Martin, working on the F-35 program, certainly two highlights of this journey.

I am grateful for the opportunity, given to me by my supervisor, Jurij Sodja, and Roeland De Breuker to do this thesis. Though the work was challenging at times, developing, manufacturing and testing of a new wind tunnel model was a truly all-encompassing project, bringing together different disciplines such as aerodynamics, structures and control. Additionally, valuable insights and experiences were gained regarding practical subjects such as the manufacturing of composites, detailed design of components and mechanisms and tolerances in general. It was an educational journey I can highly recommend to all future students.

Of course, this thesis could not have been completed without the help of others. First and foremost, I would like to thank Jurij for his daily supervision, his time and enthusiasm and most of all his endless patience. I look forward to continue to work with you and Sherry in the near future. Furthermore, I would like to thank Eddy for his help and advice with the CATIA model of the wing, which certainly optimised the workflow. The wing model could not have been build so well without the help of the technicians in the lab; thanks to the guys at DEMO, Ed and Peter, for their advice and awesome machined parts. Thanks to Victor and Fred in the composites lab for helping with my first real endeavor in the manufacturing of composites and of course thanks to Johan for his help and advice during the final assembly and finishing of the model.

A very special thanks to George and Michiel, whose regular check-ups and sanity checks have kept me going in difficult times. Both of you went above and beyond, for which I am ever grateful! I have fond memories of my time working with you on the wing box project, what fun we had building stuff to break it again, all for educational purposes.

Last but most certainly not least I would like to express my gratitude to two special folks, my parents. The last couple of years have not been easy on all of us, taking care of not only Martijn, but also grandma and grandpa. Especially the last two years were incredibly tough, both physically and mentally, with Martijn’s weak health and what seemed like never-ending hospital visits. Nevertheless you guys have shown me to never back down and never gave up. I realise we certainly have had our differences and I am not without flaws, but I am forever grateful for your unconditional support. Without your support I could not have finished this work. And remember: *alles komt goed!*

Roderick Schildkamp
Bodegraven, January 2022

This page is intentionally left blank.

Summary

With the increased focus on sustainability, aircraft are designed to reduce their emissions. One way to accomplish this is by increasing the wing aspect ratio, thereby increasing the aerodynamic efficiency, however this is not without consequences. Increased aspect ratio wings have a higher structural mass, are more susceptible to gust and maneuver loads and generally flutter at lower velocities. Due to the advent of both passive and active control techniques these issues can fortunately be solved by using gust load allevation (GLA), maneuver load alleviation (MLA) and flutter suppression.

Aeroelastic research on these topics dates back to early in the previous century. Applications of GLA can be traced back to the 1960s, where flight tests were performed using the B-52 and C-5A in order to reduce wing root bending moments and to increase the fatigue life of the wings. GLA has been performed using both conventional flight control surfaces, such as ailerons, elevators and spoilers, as well as by dedicated control surfaces or even by morphing wings. On a more fundamental level of aeroelastic research, wind tunnel experiments have been performed using wing sections typically equipped with an aileron. Few examples have been found of experimental configurations with spoilers.

Current aeroelastic testing facilities at Delft University of Technology include a gust generator and aeroelastic apparatus, used to suspend a passive wing section in the wind tunnel. The need for additional research on aeroelastic control in order to improve the sustainability and safety of aviation necessitates the development of a new wing section with aileron and spoiler control surfaces that is compatible with current facilities. The development, manufacturing and initial characterization and testing of this wing section is the subject of the present work.

As the new wing section includes a spoiler, a literature review is performed on this subject. Spoilers function by deflecting into the flow, causing separation aft of the spoiler and creating a large turbulent wake, resulting in a drastic decrease of lift. A linear potential flow model for spoiler aerodynamics developed by Brown and Parkinson was implemented in MATLAB with the intent of implementing this in future aeroelastic models. Verification of this model showed good agreements with original data presented in the paper describing the model.

The passive wing section was chosen as a basis for the new design. The position and size of the control surfaces are determined based on a review of experimental and operational applications. The new wing section was designed, resulting in a self-contained model, including a single-board computer, sensors and power supply. Actuation mechanisms were developed for the control surfaces, with a parametric device for control surface free play included in the aileron actuation mechanism. To mount the new wing section in the aeroelastic apparatus, a new mounting mechanism was designed. This mechanism allows the pitch axis of the wing section to be mounted over a range of chordwise positions, influencing the stability of the system. The new wing section was manufactured successfully and control software was implemented using Simulink.

A series of tests were performed to characterize the dynamic behavior of the wing section. Using a ground vibration test, the first bending, pitching and rocking modes were identified at 3.55 Hz, 6.39 Hz and 11.10 Hz. Due to a combination of higher inertia and kinematics of the actuation mechanism, the usable bandwidth of the aileron is shown to be lower than that of the spoiler. Aerodynamic results show that the combined use of aileron and spoiler result in a reduction or reversal of the aerodynamic response of the wing. Deflecting the spoiler beyond 60 deg does not lead to a further change in lift coefficient. Gust load alleviation results with proportional control show an increase in damping by 1300% and a reduction in peak amplitude of 50% when using the spoiler. Results for the aileron are noticeably less, with a decrease in amplitude of 15% and an increase of damping of 145%. The differences are attributed to both the differences in kinematics of the mechanisms as well as the greater absolute

change in lift coefficient obtainable by the spoiler. As the empirical pressure data necessary for the spoiler validation has not been obtained, the validation of the aerodynamic model remains inconclusive. The initial wind tunnel campaign was successful, however several points of improvement for the wing section have been identified, in addition to subjects requiring additional research.

This page is intentionally left blank.

Contents

List of Symbols

α	Angle of attack	deg
β	Aileron deflection angle	deg
δ	Spoiler deflection angle	deg
$\dot{\theta}$	Pitch rate	deg/s
ω	Angular frequency	rad/s
ω_{pco}	Phase crossover frequency	rad/s
ϕ	Acceleration potential	-
$\phi(\omega)$	Phase frequency response	deg
ρ	Density	kg/m^3
θ	Pitch angle	deg

a	Mapping variable	
b	Mapping variable	
b	Semi-chord/span	m
B_0	Constant in the cavity termination term	-
c	Chord length/airfoil separation point	m
C_0	Constant in the leading edge term	-
c_a	Aileron chord	m
C_L	Lift coefficient	-
C_l	Lift coefficient per unit span	m^{-1}
C_p	Pressure coefficient	-
c_s	Spoiler chord length	m
F	Complex acceleration potential	
f	Frequency	Hz
h	Heave displacement	m

i	Imaginary unit, $\sqrt{-1}$	-
K	Cavitation number	-
k	Reduced frequency	-
K_θ	Torsional stiffness	Nm/deg
K_d	Differential gain	
K_h	Bending stiffness	N/m
K_i	Integral gain	
K_p	Proportional gain	
L	Lift	N
l	Wake cavity length	m
L_g	Gust length	m
$M(\omega)$	Magnitude frequency response	-
M_n	Camber Fourier series coefficient	-
n	Aileron hinge location	
N_n	Thickness Fourier series coefficient	
q	Velocity vector	m/s
s	Spoiler base location	m
t	Spoiler separation point	m
U	Freestream velocity	m/s
u	Velocity perturbation along the x-axis	-
v	Velocity perturbation along the y-axis	-
w_g	Gust velocity	m/s
w_{g0}	Constant/peak gust velocity	m/s
x	Coordinate along the horizontal axis in the physical plane	m
x_g	Distance w.r.t. the initial gust encounter point	m
x_s	Spoiler location	m
y	Coordinate along the vertical axis in the physical plane	m
z	Complex variable	

List of Figures

List of Tables

1 Introduction

After a steep decline in air travel due to COVID-19, passenger air travel is projected to grow between 1.5% and 3.8% per year, over the next 20 years [5]. This prospect combined with the goal outlined in the Paris Agreements [6] to limit the rise of global temperature to two degrees above pre-industrial levels, require a solution to make aircraft less polluting. One such solution is increasing the aspect ratio of the wing. Increased aspect ratio wings however come with disadvantages such as increased susceptibility to gusts and an increase of the structural mass of the wing. Fortunately, these issues can be solved through gust load alleviation (GLA) and maneuver load alleviation (MLA) using both passive or active control techniques. To help investigate active aeroelastic control at Delft University of Technology, a new wind tunnel model is required.

The objective of this work is to design and develop a parametric experimental wing section with aileron and spoiler control surfaces. The wing section is to be used in research on aeroelastic topics such as gust load alleviation or flutter suppression and is designed for use in the M- or W-tunnel of the Low-Speed Lab at Delft University of Technology. Equipping the wing section with both spoiler and aileron control surfaces allows for the comparison of the effectiveness of these control surfaces in the various aeroservoelastic tests. After designing and building the wing section, a series of tests are performed to characterise the model. Finally, as a proof of concept a series of GLA tests using PID control are performed.

The outline of this work is as follows: First, the topic of gust load alleviation is discussed in chapter 2. The aerodynamics of spoilers is treated in chapter 3. Then, chapter 4 gives an insight in the process of designing and developing the experimental wing section, followed by the experimental setup in chapter 5. Results of the wind tunnel tests are shown and discussed in chapter 6. Based on the results, conclusions are drawn and recommendations are given in the final chapter, chapter 7.

2

Gust Load Alleviation

GLA has been the subject of numerous research projects spanning from roughly halfway the previous century until the present day. Originally starting out as a way to increase aircraft service life, nowadays research is performed on GLA to reduce structural weight, thus creating more sustainable aircraft. This chapter will first discuss the background of GLA in section 2.1. This is followed by a review of the state of the art in GLA in section 2.2.

2.1. Background

Before delving into GLA, it is necessary to get an understanding of gusts and the loads they induce in aircraft. The concepts of turbulence and gusts and their resulting loads on the aircraft will be dealt with in this section.

Anyone who has flown before has most likely encountered a patch of “rough air”. This is called turbulence, and can be described as the movement of the air mass through which an aircraft travels. Sources of turbulence vary from natural phenomena, e.g. clouds, wind shear or convection, to human-made. A common source of the latter is wake turbulence, caused by aircraft leaving disturbed air behind as it travels forward. The severity of turbulence also varies from low to extreme. Low intensity turbulence may cause minor nuisance to passengers, whereas high to extreme intensity turbulence can cause severe damage (as seen in fig. 2.1) or injuries [7] or even loss of aircraft and life [8, 9].

Figure 2.1: *A Boeing B-52 having lost the majority of its vertical tail due to wind shear. The aircraft successfully landed, was restored and flew again. The aircraft remained in service with the USAF until 2008.*

When talking about turbulence or gusts, a distinction is often made between discrete gusts and continuous turbulence. The former are commonly idealized as discrete velocity increments and solved

for in the time domain, whereas turbulence is idealized as a continuous velocity profile and analyzed in the frequency domain using Power Spectral Density (PSD) methods [10]. Commonly used turbulence models are for example the Dryden turbulence model and the Von Kármán turbulence model. A graphic comparison of gusts and turbulence is seen in fig. 2.2.

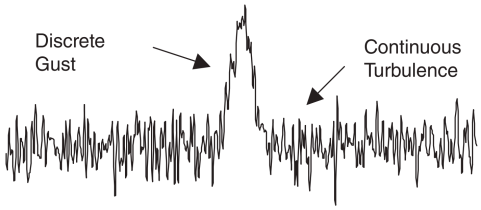

Figure 2.2: *The difference between discrete gusts and continuous turbulence. Taken from Wright and Cooper [10].*

In this work, only discrete gusts will be considered. Three common types of discrete gusts are pictured in fig. 2.3. These are the sharp-edged, sine and 1-minus-cosine gusts. The first type, as the name implies, introduces an instantaneous and constant gust velocity when the aircraft hits the gust. The gust velocity is given by eq. (2.1), where w_g, w_{g0} and x_g are the gust velocity, the constant gust velocity and the distance with respect to the initial gust encounter point. The sine gust - fig. 2.3b where w_{g0} is the peak gust velocity and L_g the gust length - has both a positive and negative component. The final type, the 1-minus-cosine gust given by eq. (2.3), gradually increases in magnitude, peaking at half of the total gust length, before returning back to zero.

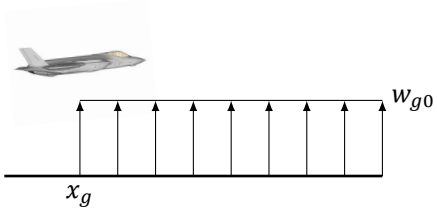

$$w_g(x_g) = \begin{cases} 0 & \text{for } x_g < 0 \\ w_{g0} & \text{for } x_g \geq 0 \end{cases} \tag{2.1}$$

(a) *Sharp edged gust.*

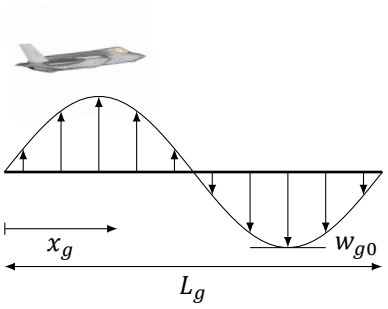

$$w_g(x_g) = w_{g0} \sin \frac{2\pi x_g}{L_g} \tag{2.2}$$

(b) *Sine gust.*

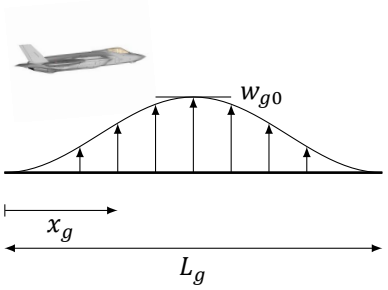

$$w_g(x_g) = \frac{w_{g0}}{2}\left(1 - \cos \frac{2\pi x_g}{L_g}\right), \; 0 \geq x_g \geq L_g \tag{2.3}$$

(c) *1-minus-cosine gust.*

Figure 2.3: *Velocity profiles of discrete gusts.*

Now that gusts have been explained, the next step is to look at the loads induced by gusts. To do this, a two-dimensional slice of the wing is taken. Flying under steady conditions at freestream velocity V_∞, lift force L is generated by that section of the wing. When the wing hits a gust with a vertical velocity V_g, this increases the velocity vector and angle of the attack encountered by the wing. In turn, the lift increases by ΔL, giving the total lift $L + \Delta L$. This situation is shown in fig. 2.4. The increase in lift translates to increased shear and bending loads along the span of the wing. Maximum shear and bending loads are encountered at the wing root.

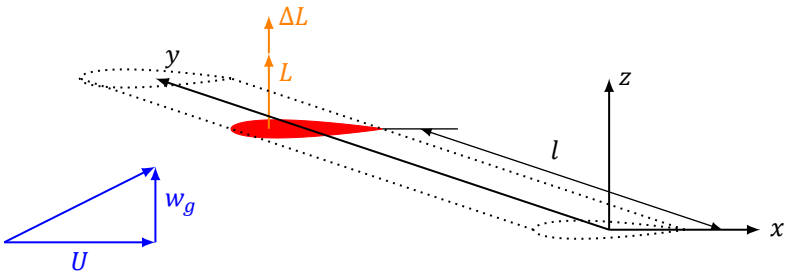

Figure 2.4: *The change in lift on a wing due to a gust encounter.*

The gust loads that a large transport aircraft is required to withstand for certification are documented in CS 25.341/FAR Part 25 §25.341 [11]. Per CS 25, the aircraft must be designed to withstand the critical case for a range of gust gradients (half the gust length) and operating altitudes and velocities. In addition it must also be able to withstand continuous turbulence loads based on the Von Kármán turbulence model. In practice this leads to a reinforced, and therefore heavier, wing structure. In a day and age where climate change and sustainability are the subject of daily headlines, aviation is frequently looked at as a major polluter. The development and implementation of active control systems can contribute to a reduction in mass of the wing, while still ensuring safety.

2.2. State of the Art

With the principles of gust and gust loads discussed, history and state of the art in GLA will be reviewed. Numerous examples of the past and current application of GLA are available. Regan and Jutte give an overview of both military and civilian systems, where applications of active control technology to reduce aircraft weight is emphasized [12]. This data is shown in table 2.1.

Table 2.1: *Overview of aircraft using GLA. The following abbreviations are used: aerodynamic (AERO), inertial (IN), load alleviation (LA), ride quality (RQ), fatigue life extension (FLE). Taken from Regan and Jutte [12].*

Aircraft	First Flight	Objective	Sensors	Actuation	Metric
Lockheed C-5A	1968	LA, FLE	IN	Symmetric aileron	5.5% empty weight reduction
Lockheed L-1011-500	1978	RQ	IN	Symmetric aileron, outboard spoilers	1.25% empty weight reduction, 3% drag reduction
Rockwell B-1	1974	RQ	IN	Canard-like vanes on nose	4.7% empty weight reduction
Northrop Grumman B-2	1989	LA, RQ	AERO, IN	Inboard elevons, dedicated GLA flap	50% reduced gust load
Airbus A320	1987	LA	IN	Aileron, spoilers, elevators	N/A
Airbus A330/A340	1992/1991	LA, RQ	IN	Rudders, elevators	N/A
Airbus A380	2005	LA, RQ	N/A	N/A	N/A
Boeing 787	2009	LA, RQ	AERO	Ailerons, spoilers, elevators	N/A

In the next subsection some of examples from table 2.1, in addition to others, will be further reviewed. These are all examples of GLA on actual aircraft, be it one-offs for flight test purposes or mass produced applications. In section 2.2.2, experimental applications of GLA, such as for example computational or wind tunnel models will be reviewed.

2.2.1. Applications of GLA on Aircraft

The Boeing B-52 was used for various GLA investigations. In support of the Load Alleviation and Mode Stabilization (LAMS) program in the 1960s, GLA was achieved using the ailerons, elevators and outer spoilers. A nose-mounted probe measured gusts, and the accelerations were recorded at three separate locations along the fuselage [13]. The B-52 for the LAMS program is seen in fig. 2.5. The Control Configured Vehicle (CCV) program followed the LAMS program. Existing flaps were replaced with flaperons and additional outboard ailerons, horizontal and vertical canards were installed. The B-52 in configuration for the CCV program is seen in fig. 2.6. Compared to the baseline aircraft, a reduction of approximately 25-30% in RMS bending moment was obtained.

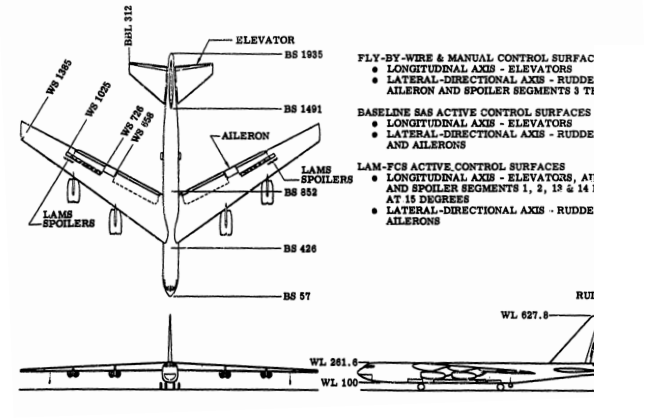

Figure 2.5: *Layout of the B-52 and explanation of the different flight control systems. Taken from Burris and Bender [13].*

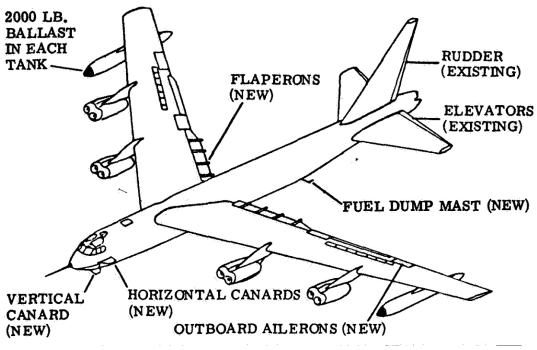

Figure 2.6: *Control surface layout of the B-52 CCV. Taken from Arnold and Murphy [14].*

Shortly after being introduced, the need for a load reduction system for the Lockheed C-5A Galaxy became clear. This led to the Lift Distribution Control System (LDCS) and Active LDCS (ALDCS) programs. [15–17]

The Rockwell B-1 is a supersonic bomber with variable geometry wings and is designed for low level, high speed flight, where it can encounter heavy turbulence. The motion of the crew compartment - located towards the front of the aircraft and connected to the main body by a relatively long and narrow fuselage section - induced by the turbulence negatively impacts both crew efficiency and handling qualities. To counter these issues the aircraft uses an active control system called Structural Mode Control System (SMCS) [1, 18]. It consists of two vanes, indicated in fig. 2.7, mounted near the crew compartment in combination with accelerometers mounted near the vanes and center of gravity. Accelerations at the crew compartment showed a decrease of 64% [19]. Implementation of the SMCS cost “only” 180 kg versus the structural modifications weighing in at 4800 kg for a similar level of ride quality.

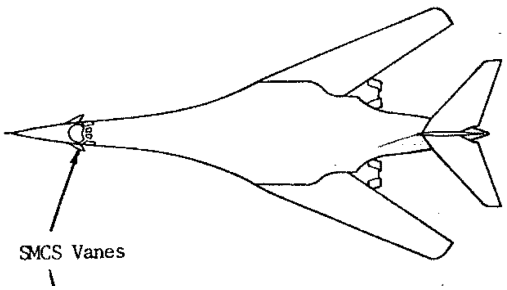

Figure 2.7: *SCMS vanes on the B-1 in high-speed configuration. Adapted from Wykes [1].*

As part of the Advanced Fighter Technology Integration (AFTI) program, a General Dynamics F-111 was fitted with a Mission Adaptive Wing (MAW) [20]. This morphing wing uses a so-called smooth variable camber concept, seen in fig. 2.8, where the LE and TE of the wing can be optimally shaped for each phase of flight. Additionally, this system can be used for maneuver load and maneuver enhancement/gust load control. The former allows for a reduction of the root bending moment by 15% at constant g or an increase in acceleration (i.e. “pulling more g’s”) at the same bending root moment. In the latter mode, for GLA, the morphing of the wing enables the aircraft to achieve the command load factor more quickly as well as reducing vertical changes in flight path by 20% to 40%.

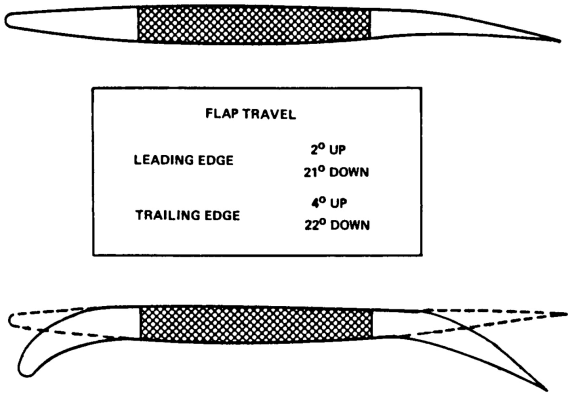

Figure 2.8: *The smooth variable camber concept. Taken from Bonnema and Smith [20].*

The Northrop Grumman B-2 stealth bomber is an aircraft with a flying wing configuration. For pitch control, the B-2 uses a centerline body flap called the Gust Load Alleviation Surface (GLAS). This flap is seen in the overview flight control system (FCS) architecture in fig. 2.9. GLA is achieved by quickly pitching the aircraft into the gust, minimizing accelerations and loads. Compared to the open-loop model, that is without any control augmentation in place, the implementation of the GLA control in the FCS reduces gust loads by up to 50 %.

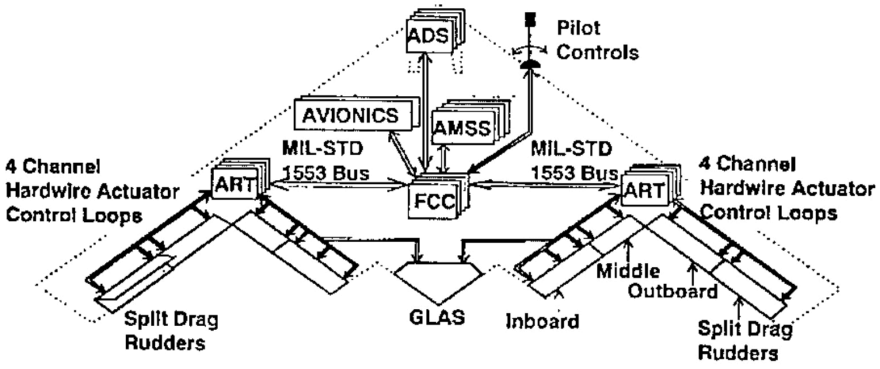

Figure 2.9: *Overview of the B-2 flight control system. The Gust Load Alleviation Surface is seen at the center of the leading edge. Taken from Britt et al. [2].*

The previous examples have shown a diverse range of methods to deal with gust loads. The reasons to investigate these methods range from improving fatigue life of a wing to preventing a decline in handling qualities. While conventional, preexisting, flight control surfaces can be used for GLA, control surfaces dedicated to GLA also exist. Even the use of wing morphing has been proven for GLA.

2.2.2. Experimental Applications of GLA

Where the previous subsection dealt with several applications of GLA on real-life aircraft, the current subsection will go into experimental applications of GLA. Since the current work deals with GLA in

wind tunnel testing, the applications reviewed here are more in line with this thesis, both in scale and complexity.

In 1998, Vipperman et al. [21] tested active control of typical section with trailing edge flap, using a similar setup as the one used for this work. The work was done using a 25.35 cm x 52 cm rectangular wing section with a NACA0012 airfoil and equipped with 6.35 cm flap. The wing is mounted to support blocks by an axle. A spring connected to this axle provides stiffness to the pitch DoF. The heave DoF is provided by a pair of leaf springs, connecting the support blocks to the wind tunnel. Results show substantial increase in damping of the closed-loop system, with the closed-loop system decaying in a quarter or the time of the open-loop system.

Few examples of research on active aeroelastic control using spoilers are available. One of these examples is the research performed by Cassaro, Nágy et al. [22] and Cassaro, Battipede et al. [23]. An experimental wing section with pitch and heave DoFs was developed, with a chord of 0.2 m, a span of 0.3175 m and a NACA0024 profile. Five spoilers of $0.05c$ were fitted near the leading edge at $0.15c$, along the entire span of the wing. A cross-sectional schematic of the wing section is seen in fig. 2.10. Research showed the spoiler in combination with a model reference adaptive control (MRAC) is highly effective for GLA, with the majority of disturbances damped out within two seconds.

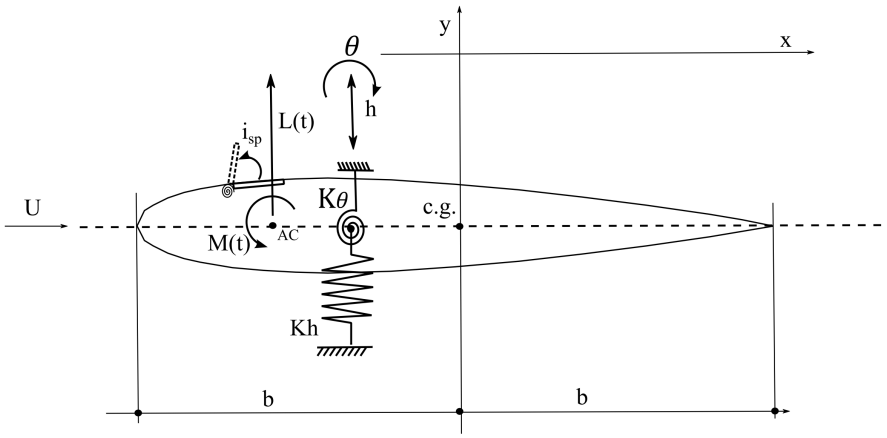

Figure 2.10: *Overview of the two DoF aeroelastic model with spoilers. The spoiler is divided into five separate control surfaces. Taken from Cassaro et al. [23].*

Another example of the use of spoilers for GLA is by Lancelot and De Breuker [24]. In this conceptual study, a NACA0010 airfoil with a 1 m chord length is equipped with a $0.1c$ spoiler located at $0.65c$, as seen in fig. 2.11. A passive deployment mechanism based on a linear spring and magnets is used. The spring is pre-loaded and aids the deployment of the spoiler, due to the build-up of aerodynamic forces upon deployment. The magnets ensure the spoiler stays in the retracted position when no gusts are present. The main advantage of a passive system like this is the quick reaction time of the mechanism when subjected to a gust, with little delay and no (complex) active control systems involved. Results show a reduction in loads of up to 9%.

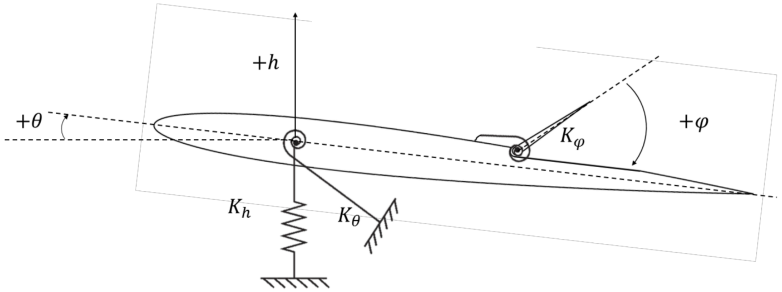

Figure 2.11: *Overview of the three DoF aeroelastic model with spoiler. K_h is the bending stiffness of the wing, K_θ the torsional stiffness of the wing, and K_ϕ the torsional stiffness of the spoiler. Taken from Lancelot and De Breuker [24]*

Quenzer et al. and Barzgaran et al. [25, 26] developed a low-cost model to investigate active control

techniques for GLA. This model is half-span aircraft model with a wing and tail, seen in fig. 2.12. The structural components consist of a fuselage, wing and tail beam. The lifting surfaces are composed of several aerodynamic shells with a NACA0012 profile. These shells can be active or inactive, the former containing a control surface and actuator. Experiments were run using both linear-quadratic regulator (LQR) and model predictive control (MPC). While the LQR results closely follow the open-loop loads, a reduction in peak loads of about 40% is achieved.

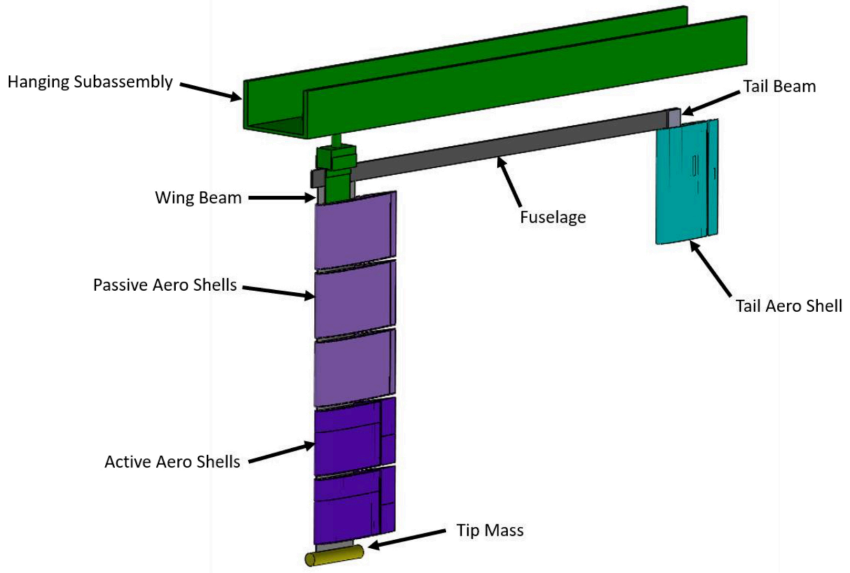

Figure 2.12: *Low-cost wing/fuselage/tail configuration model. Taken from Quenzer et al [25].*

A final example of experimental GLA is the folding wingtip. Research was done by Cheung et al. [27] on a cantilever wing where the wingtip is freely hinged, with the hinge line at an angle with respect to the flow. Due to the angle of the hing with respect to the flow, the effective angle of attack decreases as the wingtip folds upwards due to a gust. Compared to the results with the hinge locked, a reduction in peak root bending moment of 6% was found for shorter gust lengths. For longer gusts, this reduction increased to 11%.

The presented models highlight typical implementations for aero(servo)elastic research, such as GLA or flutter suppression. The models consist of an wing section of a symmetric NACA airfoil, connected to a mechanisms providing heave and pitch degrees of freedom. While wing sections equipped with an aileron are most common, two models equipped with a spoiler have been found. The implemented control methods for these models range from passive control using magnets and springs to the classical linear-quadratic-Gaussian/regulator (LQG/LQR) control or online methods such as MRAC and MPC, where the latter method show great potential, decreasing peak loads by up to 40%.

The different models have all shown to reduce gust loads. It is however not clear how the use of ailerons compares to the use spoiler for GLA, as a comparison has not been found. In addition, tried and tested aeroelastic models are available for a wing section with an aileron, this is not the case wing sections with spoilers. These cases have shown to generally depend on either experimentally obtained data or data from computational fluid dynamics (CFD), known to be computationally expensive. In order to bridge these gaps in knowledge, an aerodynamic model for spoilers for use with aeroelastic models will be introduced in chapter 3. This is followed by the development of an experimental wing section equipped with both an aileron and a spoiler to perform comparative aeroelastic studies on GLA and flutter suppression in chapter 4.

3

Aerodynamics of Spoiler Type Control Surfaces

One of the main objectives of the current work is to investigate the effectiveness of spoilers for GLA. To this end, the experimental wing section used for the wind tunnel tests will be outfitted with a spoiler. Before the wing section can be built and any tests can be performed, the design and placement of the spoiler needs to be considered, as well as the impact of the design on its aerodynamic response.

The aerodynamics of spoilers is treated in this chapter. First, the geometry of spoiler type devices is reviewed in section 3.1. After this, in section 3.2, the flow around airfoils with spoilers and its response is discussed. In the final part of this chapter, section 3.3, a method is presented to model the aerodynamics of an airfoil with spoiler.

3.1. Spoiler Functions and Geometry

Before discussing the aerodynamics of spoilers, their function must first be understood. This is discussed in section 3.1.1. Closely related to their function, is the geometry of spoilers, treated in section 3.1.2.

3.1.1. Functions of a Spoiler

Spoilers are one of the different types of control devices found on aircraft. Whereas, in a classical sense, elevators and ailerons generally serve only one specific purpose, spoilers are employed for multiple purposes. These functions can be [28–30] lift dumping (Direct Lift Control - DLC), air braking or providing roll control.

Found on top of the wings of most commercial wide-body aircraft, spoilers are commonly deployed upon landing, i.e. 'weight on wheels'. Deployment of the spoilers, as the name suggests, spoils the lift created by the wings, ensuring the weight of the aircraft rests completely on the landing gear, ensuring effective braking. Additionally, spoilers may be used prior to landing to increase rate of descent.

Besides spoiling, or dumping lift, spoilers can also be used as speed brakes. To accomplish this, spoilers are deployed symmetrically. Flow over the wing detaches and generates a significant amount of drag. This is used both in-flight as well as during rollout, where its effectiveness however decreases, due to decreasing air speed.

The final function of a spoiler is roll control. By asymmetrically deploying the spoilers, lift is reduced on one side of the aircraft. This induces a rolling moment to the side of the deployed spoiler. A benefit of using spoilers for roll control is proverse yaw, i.e. a yawing moment in the same direction as the

rolling moment, due to the increase in drag. This is in contrast to the more conventional roll control method, differential aileron deflection, which produces adverse yaw [30].

This method is commonly applied to variable-sweep aircraft, where trailing edge control surfaces cannot be used when the wing is (fully) swept, due to proximity of the trailing edge to the fuselage. Examples are the Grumman F-14 [31], the General Dynamics F-111 and North American Rockwell B-1.

3.1.2. Spoiler Geometry

With the functions of a spoiler now clear, their geometry can be studied. The typical spoiler is a plate attached along the surface of a lifting body and upon activation is deflected into the free stream. However, parameters such as length, span, and placement differ per application. In addition to these parameters, two different types of kinematics can be identified; The normal or vertical spoiler is a spoiler commonly seen on sail planes. The kinematics of this spoiler are such that the spoiler extends perpendicular to the wing surface. An example of this type of spoiler is shown in fig. 3.1a. The flush spoiler is a skin panel mounted flush with the surrounding wing skins. This type is connected to the main wing structure by one or several brackets and rotates when deployed as seen in fig. 3.1b.

(a) *Normal or vertical spoilers on a glider aircraft. Adapted from [32].*

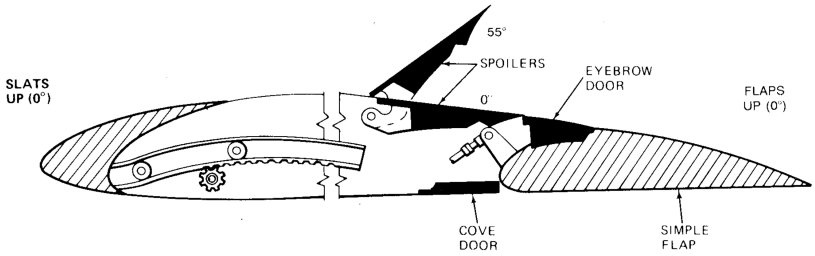

(b) *Cross-section of the wing of an F-14 showing the flush spoiler in its stowed and deployed positions. Taken from [31].*

Figure 3.1: *The two main different types of spoilers.*

To give an overview of the bounds on geometrical parameters such as length, span and placement of the spoiler, the spoiler geometry used on several aircraft is tabulated in table 3.1. Similar data for spoilers used in numerous wind tunnel and numerical experiments is found in table 3.2.

The data summarized in table 3.1, shows a clear lack of available data on the geometry of operational aircraft. Sufficient data is however available on experimentally used wing sections with spoilers. In these experiments, spoilers are typically located around 0.7c and have a length of 0.10c or 0.15c. Spoiler deflection angles range from small deflections of around 20 degrees up to large deflections of 90 degrees. The majority of the maximum deflections lies between 70 and 90 degrees. The greatest outlier in this data is the setup by Cassaro et al. [22, 23], where the spoiler is actually located near the leading edge of the wing. The choice by Cassaro et al. to place the spoilers near the leading edge was based on earlier research, indicating placement of an actuator near the leading edge is highly effective in controlling the flow over the entire airfoil.

Besides these parameters, other parameters can also be considered in the design of the spoiler. Wentz et al. experimentally investigated the effect of several parameters such as hingeline gap, spoiler porosity, trailing edge geometry, lower surface venting and a lower surface deflector on the control effectiveness and hinge moment of an airfoil with spoiler [53].

Table 3.1: *Overview of different spoiler geometries used on aircraft.*

		Location [x/c]	Span [2y/b]	Length [c_s/c]	Deflection Angle [deg]
Boeing B-52	[33]	0.6	0.4-0.7	N/A	N/A
KU Redhawk [1]	[34, 35]	N/A	0.5-0.635[2]	0.087[2]	N/A
			0.645-0.965[3]	0.138[3]	N/A
F-111A	[36]	N/A	N/A	N/A	43
Grumman F-14	[37, 38]	0.60	N/A	N/A	59
Boeing 737 NG	[39]	N/A	N/A	N/A	33/38 [4]

[1] The Redhawk is a Cessna 177 Cardinal, modified by the University of Kansas.
[2] Inboard spoiler.
[3] Outboard spoiler.
[4] Maximum deflection in-flight; 33 deg for spoilers 2, 3, 10, and 11, 38 deg for spoilers 4, 5, 8, and 9.

Table 3.2: *Overview of different spoiler geometries used in wind tunnel experiments.*

		Location [x/c]	Span [b_s/b]	Length [c_s/c]	Deflection Angle [deg]
GA(W)-2	[40, 41]	0.775	N/A	0.10	60
LS(1)-0413	[42]	0.775	N/A	0.10	60
0.113 t/c Boeing	[42]	0.733	N/A	0.157	60
Unspecified airfoil	[43]	0.733	N/A	0.1554	60
0.113 t/c Boeing	[44, 45]	0.733	N/A	0.1554	60
0.16 t/c supercritical	[46]	0.52	N/A	0.15	40
NACA 0015	[47]	0.70	N/A	0.10	45
	[48]	0.70	N/A	0.084	90
	[49]	0.70	N/A	0.10	22.5 - 75
Clark Y-14	[47]	0.70	N/A	0.05, 0.10	45
	[50]	0.70	N/A	0.10	90
	[51]	0.70	N/A	0.10	20, 30, 45
NACA 0024	[22, 23]	0.15	N/A	0.05	85
NACA 0010	[24]	0.65	N/A	0.10	N/A
DLR-F15DS	[52]	0.745	0.214	0.15	85

Since this work relates to aeroelastic and not aerodynamic research, in addition to the practicality at this scale, details such as control surface porosity, lower surface venting and trailing edge geometry will not be considered. Only the effect of the hingeline gap is looked at for the purpose of this work, as it may not be possible to create a gapless spoiler due to practical limits with respect to the manufacturing of the wing section such as tolerances and material thicknesses.

The hingeline gap is the gap between the top surface of the airfoil/wing and the leading edge of the deflected spoiler. To investigate the effect of this gap on control effectiveness, spoilers with a 0.0%, 0.5%, 2.0%, and 4.5% chord gap were tested. Control effectiveness ΔC_l is plotted versus normalized spoiler projection height $\Delta h/c$ for $\alpha = 0$ deg and $\alpha = 14$ deg in figs. 3.2 and 3.3. For a gap size of 0.5% of the chord, the control effectiveness shows little difference when no gap is present. However the control effectiveness is improved in the specific case of high angle of attack and low spoiler deflection. A drawback of this gap is the decreased maximum spoiler control effectiveness. This can be attributed to the fact that for the larger gap sizes, a significant portion of the boundary layer flows between the spoiler and the skin, preventing flow separation behind the spoiler.

3.2. Flow Characteristics around Airfoils with Spoilers

Multiple experiments have been performed to investigate the flow field around airfoils with spoilers. One of these studies was performed by Mack et al. [41] on a GA(W)-2 airfoil of 13% thickness. This airfoil was equipped with 0.1c spoiler located at 0.775c and a 0.25c slotted flap [40]. Wind tunnel tests were run at angles of attack (AOA) between 8 deg and 12 deg, at Mach 0.13 and a Reynold's number of 2.2E6. Data was obtained using pressure probes of two different types, and split film anemometers

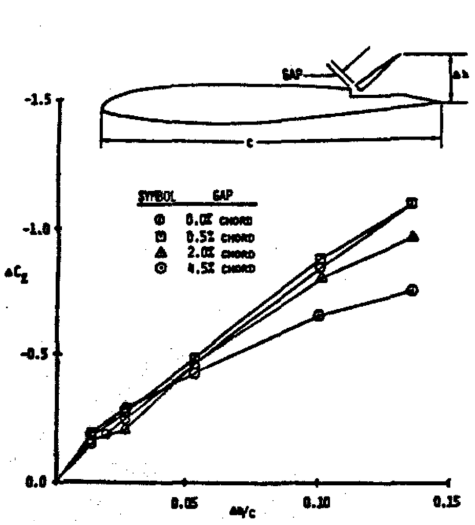

Figure 3.2: *Spoiler effectiveness for different gap sizes at $\alpha = 0°$. Taken from Wentz et al. [53].*

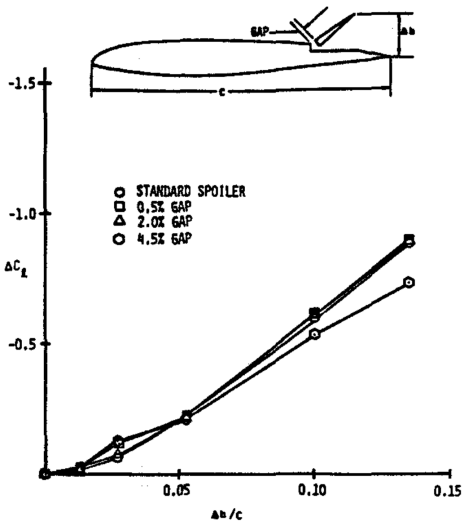

Figure 3.3: *Spoiler effectiveness for different gap sizes at $\alpha = 14°$. Taken from Wentz et al. [53].*

(single and dual types). At 8 deg AOA, the spoiler was deflected from 0 deg to 20 deg and 60 deg At 20 deg, the region of reverse flow extends downstream to between $0.2c$ and $0.4c$ of the trailing edge of the flap.

Interestingly, at 60 deg the flow not only separates aft of the spoiler, but also in front of the spoiler, forming a so-called “hinge bubble”. This is seen in fig. 3.4. The increase in pressure is directly related to the size of the region of reverse flow, with greater regions of reverse flow resulting in larger increases of pressure [54]. In turn, this increase in pressure creates an adverse pressure gradient, resulting in separated flow.

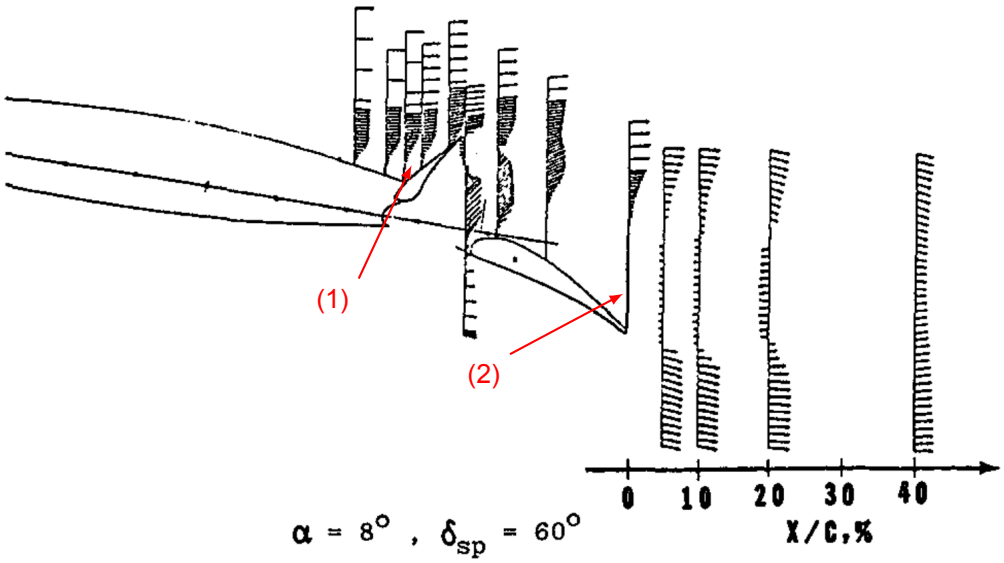

Figure 3.4: *Velocity plot showing regions of separated flow. 1) Hinge bubble in front of the spoiler. 2) Region of reversed flow behind the spoiler. Adapted from Mack et al. [41].*

Additional experiments by McLachlan et al. [43] as well as Consigny et al. [46] show regions of separated and reversed flow in the wake. When the angle of attack is increased beyond the stall angle, separation occurs far in front of the the spoiler. This results in spoiler being positioned in the developed wake, completely negating the effect of the deflected spoiler on the pressure distribution.

Summarizing, the following general trends are observed; for low spoiler deflection angles flow de-

taches from the spoiler, later reattaching to the rear of the airfoil, creating a region of reversed flow behind the spoiler. Upon further increasing the deflection, the flow fully separates without reattaching, enlarging the region of reversed flow. At high deflection angles a separation bubble can also form in front of the spoiler. For a constant spoiler deflection, a generally constant ΔC_L is created for changing angle of attack until the airfoil stalls. Once the airfoil has stalled, the spoiler has little effect.

3.3. Aerodynamic Model for the Flow around Airfoils with Spoilers

With the advent of computers, the complex flow around spoilers is nowadays modelled using computational fluid dynamics (CFD) [24, 55]. This method however is computationally expensive and has not always been available. Before the advent of CFD, other methods such as (unsteady) two-dimensional [45, 47–51, 56–58] and (hybrid) three-dimensional [59, 60] vortex panel methods were used to calculate the flow around spoilers.

While less computationally expensive than CFD, these panel methods still require the discretization of the geometry and large systems of equations to be solved, especially in the case of unsteady panel methods, where the system of equations will need to be solved at each time-step and change in state and control variable. Theodorsen [61] introduced a method for the aeroelastic analysis of airfoils with an aileron control surface using unsteady aerodynamics, requiring little input and no discretization of the geometry. Since this method is still commonly used in the field of aeroelasticity, a model matching that of Theodorsen is sought.

Some of the first work on modelling spoiler aerodynamics can be traced back to the 1950s, when Woods [62] presents a first model for spoiler aerodynamics. The method presented by Woods serves as a basis for the work of Barnes [63]. Both methods primarily deal with static, normal spoilers and require empirical input in the form of the wake pressure.

In 1973 Brown and Parkinson present an aerodynamic model for spoilers of arbitrary geometry, including both flush and normal spoilers, in the form of a linearized potential flow model using a combination of thin-airfoil theory to predict the forces and moments on the airfoil and constant-cavity-pressure model used in hydrodynamics. Contrary to Woods and Barnes, this method is also extended to include transient response after spoiler actuation. As this method can be traced back to an adaptation of the method by Theodorsen, it is deemed a good candidate for this work and will be presented below.

3.3.1. Linearized Potential Flow Model for Spoiler Aerodynamics

Figure 3.5 shows an airfoil with aileron and spoiler in the physical plane, around which the flow is to be solved. An airfoil of chord length c is placed in the physical (x, y) plane with its leading edge at origin $\mathcal{O}$ and is subjected to a flow with freestream velocity U at angle of attack α. The flow is assumed to be steady, incompressible, inviscid and irrotational. Furthermore, the airfoil is equipped with a spoiler positioned at s and an aileron positioned at n.

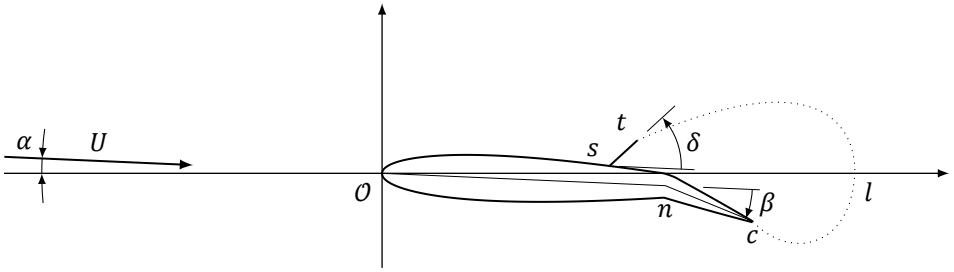

Figure 3.5: *Airfoil geometry in the physical plane. The points indicated are the following: spoiler base location s, spoiler separation point t, aileron hinge location n, aileron separation point c and cavity length l. The leading edge of the airfoil coincides with origin $\mathcal{O}$. Adapted from Parkinson and Brown [3] and Bernier [4].*

Due to the deflection of the spoiler, a closed cavity develops from spoiler separation point t at the upper side of the airfoil to the aileron separation point c at the trailing edge of the airfoil. The pressure inside the cavity, P_c, can be related to the static pressure in the free stream, P_∞ by cavitation number K and the base pressure coefficient C_{p_b}, as defined by eq. (3.1).

$$K = \frac{p_\infty - p_c}{\frac{1}{2}\rho U^2} = -C_{p_b} \tag{3.1}$$

The velocity vector q at any point in the flow can be expressed as eq. (3.2), where U is the freestream velocity and u, v are the dimensionless velocity perturbations in x- and y-direction respectively. Assuming small perturbations, the problem can be linearized, making the slope of the airfoil equal to the velocity perturbation in y-direction .

$$q = U\left((1+u), v\right)) \tag{3.2}$$

Introducing the complex variable $z = x + iy$, the complex acceleration potential can be defined by eq. (3.3), where ϕ is the acceleration potential - defined as zero on the cavity - and ψ is its complex conjugate, the acceleration stream function.

$$F(z,t) = \phi(x,y,t) + i\psi(x,y,t) \tag{3.3}$$

The velocity perturbations can be related to the acceleration potential and acceleration stream function by combining the Euler and Cauchy-Riemann equations, giving eqs. (3.4) and (3.5). Applying the case of steady flow ($\delta\delta t = 0$), these expressions can be integrated to eqs. (3.6) and (3.7).

$$\frac{\partial u}{\partial t} + U\frac{\partial u}{\partial x} = U\frac{\partial \phi}{\partial x} \tag{3.4}$$

$$\frac{\partial v}{\partial t} + U\frac{\partial v}{\partial x} = -U\frac{\partial \psi}{\partial x} \tag{3.5}$$

$$u = \phi + \frac{1}{2}K \tag{3.6}$$

$$v = -\psi \tag{3.7}$$

The pressure in the cavity created by the spoiler is related to the freestream pressure p_∞ by cavitation number K according to eq. (3.1).

$$C_p = -2\phi - K \tag{3.8}$$

With the Blasius theorem, eq. (3.9), the lift L and drag D can be determined by integrating along the closed boundary formed by the airfoil and cavity. In terms of lift and drag coefficient C_l and C_d eq. (3.9) can be expressed as eq. (3.10).

$$D - iL = i\rho U^2 \oint F^2(z)dz \tag{3.9}$$

$$C_d - iC_l = \frac{2i}{c} \oint F(z)dz \tag{3.10}$$

To calculate the flow around the airfoil with spoiler and aileron depicted in fig. 3.5, this method uses a series of conformal transformations. Figures 3.6a to 3.6d show the (intermediate) transformations of the airfoil in the physical plane to the upper half of the unit circle in the complex ζ-plane. For the mapping of the airfoil contour in front of the wake, contour $s\mathcal{O}c$, from the linearized physical plane to the complex ζ-plane, eqs. (3.11) to (3.13) are used, where a and b are mapping constants.

$$z = \frac{la^{-2}\left[\frac{1}{4}(b+1)\left(\zeta + \zeta^{-1}\right) - \frac{1}{2}(1-b)\right]^2}{1 + a^{-2}\left[\frac{1}{4}(b+1)\left(\zeta + \zeta^{-1}\right) - \frac{1}{2}(1-b)\right]^2} \tag{3.11}$$

$$a = \sqrt{\frac{l-c}{c}} \tag{3.12}$$

$$b = a\sqrt{\frac{t}{l-t}} \tag{3.13}$$

The locations indicated in fig. 3.6d by θ_0, θ_1 and θ_2 correspond to the origin $\mathcal{O}$, spoiler base location s and the aileron hinge location n in fig. 3.5 and are defined by eqs. (3.14) to (3.16).

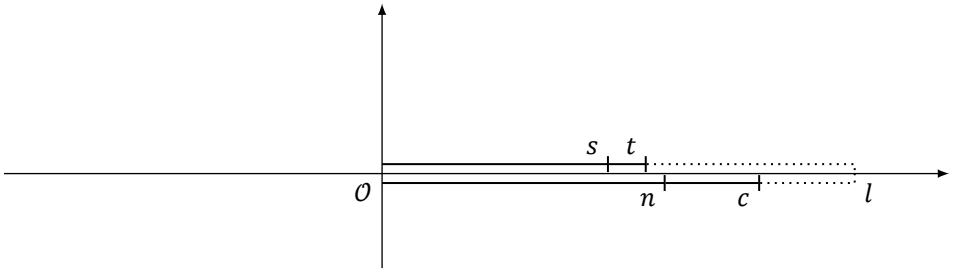

(a) *Z-plane, the linearized physical plane.*

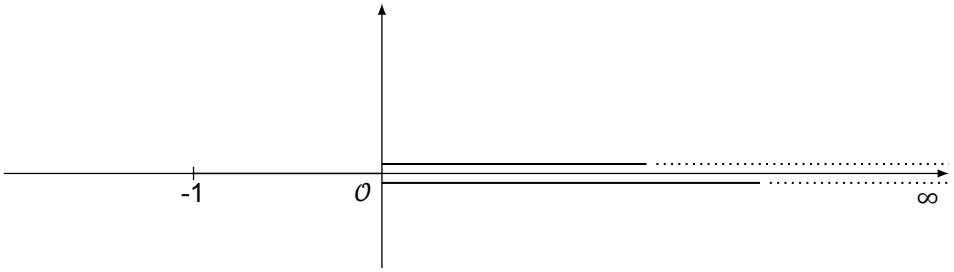

(b) *Z'-plane. Here the cavity is extended to infinity.*

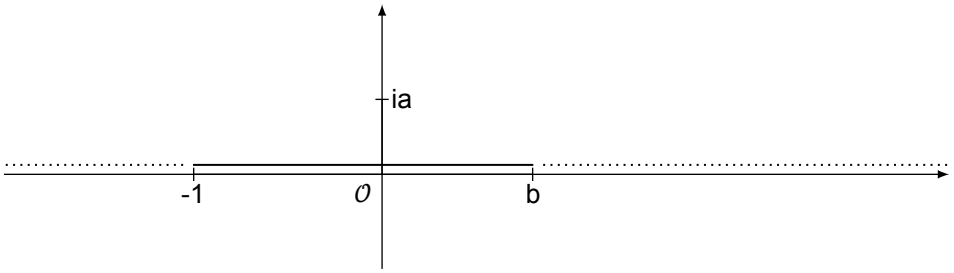

(c) ν*-plane. The flow field is mapped to the upper half of the complex plane by unfolding the real positive axis.*

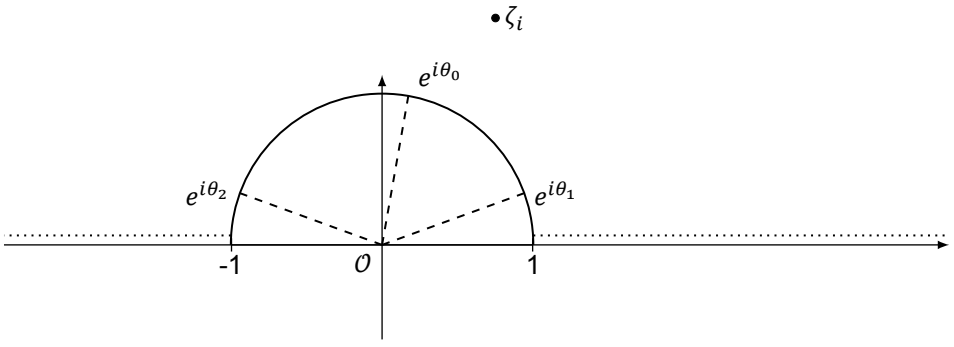

(d) ζ*-plane, the final transformed plane. The airfoil is mapped to the upper half of the unit circle. Angular positions* θ_0, θ_1 *and* θ_2 *are respectively the airfoil leading edge, spoiler base and flap hinge in the* ζ*-plane.*

Figure 3.6: *Complex transformation planes. Adapted from Parkinson and Brown [3] and Bernier [4].*

$$\theta_0 = \cos^{-1}\frac{1-b}{1+b} \tag{3.14}$$

$$\theta_1 = \cos\left[\frac{2}{1+b}\left\{a\sqrt{\frac{s}{l-s}} + \frac{1-b}{2}\right\}\right] \tag{3.15}$$

$$\theta_2 = \cos\left[\frac{2}{1+b}\left\{\frac{1-b}{2} - a\sqrt{\frac{c-c_f}{l-c+c_f}} + \right\}\right] \tag{3.16}$$

To be able to calculate the complex acceleration potential F, the following boundary conditions are applied to the linearized airfoil:

1. The real part of the complex acceleration potential $\phi = \mathrm{Re}\,F$ is zero on the cavity, that is $\phi = 0$ for $t \leq x \leq l$ on the upper surface of the linearized airfoil and $\phi = 0$ for $c \leq x \leq l$ on the lower surface of the linearized airfoil.
2. The Kutta condition should be satisfied, that is the flow shall smoothly leave the airfoil at spoiler separation point t and aileron separation point c, therefore making the acceleration potential ϕ continuous.
3. No normal flow through the airfoil surface, where the airfoil surface is given by (x, y). From eq. (3.7) this gives $v = -\psi = dy/dx$ for $0 < x < t$ on the upper surface of the linearized airfoil and $0 < x < c$ on the lower surface of the linearized airfoil.
4. From eq. (3.8), at infinity the acceleration potential is defined as $F = -\frac{1}{2}K$
5. The system consisting of the airfoil and cavity must be a closed body, giving $\mathrm{Im}\oint F(z)dz = 0$.

A thin airfoil theory-like method is used to calculate the flow around the model. The complex acceleration potential is calculated for the cases of airfoil incidence, camber and thickness and the spoiler and flap independently. As this is a linearized model, these individual solutions can be added together using the principle of superposition to get to total complex acceleration potential.

The acceleration potential due to incidence is given by eq. (3.17), where B_0, C_0 and D_0 are real constants which will be determined later. Since ζ is real and $|\zeta| \geq 1$ on the cavity, F_{in} is imaginary, satisfying boundary condition 1. Boundary condition 2 is satisfied as $\mathrm{Re}\,F_{in}(\zeta)$ is continuous on the unit circle, with $\zeta = e^{i\theta}$ at the spoiler, $\theta = 0$, and at the trailing edge, $\theta = \pi$.

$$F_{in}(\zeta) = iC_0\left[\frac{1}{\zeta e^{i\theta_0} - 1} + \frac{1}{\zeta e^{-i\theta_0} - 1}\right] + iB_0\left(\zeta - \frac{1}{\zeta}\right) + iD_0 \tag{3.17}$$

The camber solution is given by eq. (3.18). In this equation, M_n are real constants defined by eq. (3.19), given by combining boundary condition 3 and the cosine Fourier series expansion for the slope of the airfoil camber line, $(dy/dx)_c$.

$$F_c(\zeta) = -i\sum_1^\infty \frac{M_n}{\zeta_n} \tag{3.18}$$

$$M_n = \frac{2}{\pi}\int_0^\pi \left(\frac{dy}{dx}\right)_c \cos n\theta d\theta \tag{3.19}$$

Equation (3.20) is the contribution of the airfoil thickness to the complex acceleration potential, again satisfying the free stream and Kutta boundary condition. The real constants N_n are given by eqs. (3.21) and (3.22) and similar to the camber case, the constants are a combination of boundary condition 3 and a cosine Fourier series expansion of the slope of the thickness distribution line, $(dy/dx)_t$.

$$F_t(\zeta) = \frac{i\zeta}{\left(\zeta - e^{i\theta_0}\right)\left(\zeta - e^{-i\theta_0}\right)}\sum_0^\infty \frac{N_n}{\zeta^n} \tag{3.20}$$

$$N_n = \frac{4}{\pi}\int_0^{\pi}\left(\frac{dy}{dx}\right)_t(\cos\theta_0 - \cos\theta)\cos n\theta\, d\theta, n \geq 1 \tag{3.21}$$

$$N_0 = \frac{4}{\pi}\int_0^{\pi}\left(\frac{dy}{dx}\right)_t(\cos\theta_0 - \cos\theta)\, d\theta \tag{3.22}$$

The spoiler produces a step change in the normal velocity component, v, passing the airfoil contour at the spoiler base location s. This step change is accounted for by the logarithm in eq. (3.23). As can also be seen in this equation is the use of $\sin\delta$ instead of δ. Though the use of this trigonometric term violates the assumption of linear theory, it expands the useful range from only small angles to spoiler deflections of up to 90 degrees. Application of boundary condition 3 again gives the normal velocity along the airfoil according to eq. (3.24).

$$F_s(\zeta) = \frac{\sin\delta}{\pi}\left[\frac{i\theta_1}{\zeta e^{i\theta_0} - 1} + \frac{i\theta_1}{\zeta e^{i\theta_0} - 1} + \ln\left\{\frac{\zeta - e^{i\theta_1}}{\zeta - e^{-i\theta_1}}\right\}\right] \tag{3.23}$$

$$v = \begin{cases} 0, & \text{for } \pi > \theta > \theta_1 \\ \sin\delta, & \text{for } \theta_1 > \theta > 0 \end{cases} \tag{3.24}$$

The final component to the acceleration potential is that of the aileron, eq. (3.25). Similar to the spoiler, when deployed the aileron creates a step change in normal velocity. Therefore, the form of this component is identical to that of the spoiler, with the exception of the deflection angle. For the aileron this stays true to the small angle approximation where $\sin\beta \approx \beta$. And again, similar to the spoiler, application of boundary condition 3 gives the normal velocity along the airfoil. Equation (3.26) shows that for a positive (downward) aileron deflection, a normal velocity in negative direction is created.

$$F_a(\zeta) = \frac{\beta}{\pi}\left[\frac{i\,(\theta_2 - \pi)}{\zeta e^{i\theta_0} - 1} + \frac{i\,(\theta_2 - \pi)}{\zeta e^{-i\theta_0} - 1} + \ln\left\{\frac{\zeta - e^{i\theta_2}}{\zeta - e^{-i\theta_2}}\right\}\right] \tag{3.25}$$

$$v = \begin{cases} 0, & \text{for } \theta_2 > \theta > 0 \\ -\beta, & \text{for } \pi > \theta > \theta_2 \end{cases} \tag{3.26}$$

The individual components of the complex acceleration potential have now been determined. All components satisfy boundary conditions 1 through 3, however conditions 4 and 5 are still to be satisfied. Boundary condition 4, the acceleration potential at infinity can be expressed as eq. (3.27), with ζ_i, the point at infinity in the ζ-plane given by eq. (3.28).

$$F_{in}(\zeta_i) + F_c(\zeta_i) + F_t(\zeta_i) + F_s(\zeta_i) + F_f(\zeta_i) = -\frac{K}{2} \tag{3.27}$$

$$\zeta_i = \frac{2}{1+b}\left[ia + \frac{1-b}{a}\right] + \sqrt{\left(\frac{2}{1+b}\right)^2\left\{ia + \frac{1-b}{2}\right\}^2 - 1} \tag{3.28}$$

Of eq. (3.27), the incidence term is still unknown and the known terms can be grouped into variable E, giving eq. (3.29). To solve for B_0 and C_0, rewritten as eq. (3.30), where λ_1 and λ_2 are given by eqs. (3.31) and (3.32). Finally, eq. (3.30) is solved for constants B_0 and C_0 in eqs. (3.33) and (3.34).

$$E = -F_c(\zeta_i) - F_t(\zeta_i) - F_s(\zeta_i) - F_f(\zeta_i) \tag{3.29}$$

$$C_0\lambda_1 + B_0\lambda_2 = E - i\left(\alpha - \frac{M_0}{2}\right) - \frac{K}{2} \tag{3.30}$$

$$\lambda_1 = i\left[\frac{1}{\zeta e^{i\theta_0} - 1} + \frac{1}{\zeta e^{-i\theta_0} - 1}\right] \tag{3.31}$$

$$\lambda_2 = i\left(\zeta - \frac{1}{\zeta}\right) \tag{3.32}$$

$$B_0 = \frac{\operatorname{Re}\lambda_1\,(\operatorname{Im}E - \alpha + 0.5M_0) - \operatorname{Im}\lambda_1\operatorname{Re}E + 0.5K\operatorname{Im}\lambda_1}{\operatorname{Re}\lambda_1\operatorname{Im}\lambda_2 - \operatorname{Im}\lambda_1\operatorname{Re}\lambda_2} \tag{3.33}$$

$$C_0 = \frac{\operatorname{Re}E - B_0\operatorname{Re}\lambda_2 - 0.5K}{\operatorname{Re}\lambda_1} \tag{3.34}$$

Finally, boundary condition 5 can be used to express the cavitation number K in terms of wake length l leading to eq. (3.35). However, K is provided as empirical input and the points of interest on the unit circle, θ_0, θ_1 and θ_2 are complex functions of l, eq. (3.35) is solved for a range of l, after which the corresponding cavity length is determined by interpolation of the cavity lengths and their calculated cavitation number.

$$\begin{aligned} K =& 2\operatorname{Re}\left\{ la_1\left(i\left(1+\frac{1}{a_0^2}\right)\left[\frac{\operatorname{Re}\lambda_1[\operatorname{Im}E-(\alpha-M_0/2)]-\operatorname{Im}\lambda_1 ReE}{\operatorname{Re}\lambda_1\operatorname{Im}\lambda_2-\operatorname{Im}\lambda_1\operatorname{Re}\lambda_2}\right]\right.\right. \\ & -i\left[\frac{e^{i\theta_0}}{(a_0e^{i\theta_0}-1)^2}+\frac{e^{-i\theta_0}}{(a_0e^{-i\theta_0}-1)^2}\right] \\ & \cdot\left[\frac{\operatorname{Re}\lambda_2[\operatorname{Im}E-(\alpha-M_0/2)]-\operatorname{Im}\lambda_2 ReE}{\operatorname{Re}\lambda_2\operatorname{Im}\lambda_1-\operatorname{Im}\lambda_2\operatorname{Re}\lambda_1}+\frac{\theta_1\sin\delta}{\pi}+\frac{\theta_2-\pi}{\pi}\eta\right] \\ & +\frac{\sin\delta}{\pi}\left[\frac{1}{a_0-e^{i\theta_1}}+\frac{1}{a_0-e^{-i\theta_1}}\right]+\frac{\beta}{\pi}\left[\frac{1}{a_0-e^{i\theta_2}}+\frac{1}{a_0-e^{-i\theta_2}}\right] \\ & \left.\left.+i\sum_1^\infty\frac{nM_n}{a_0^{n+1}}+i\sum_0^\infty N_n\frac{\left[\frac{1-n}{a_0}-\frac{e^{i\theta_0}}{a_0e^{i\theta_0}-1}-\frac{e^{-i\theta_0}}{a_0e^{-i\theta_0}-1}\right]}{a_0^{n-1}(a_0e^{i\theta_0}-1)(a_0e^{-i\theta_0}-1)}\right)\right\} \end{aligned} \tag{3.35}$$

With the complex acceleration potential and cavitation number defined, the pressure coefficient and lift coefficient can be calculated. The former is calculated using eq. (3.35) and summing the real values of eqs. (3.17), (3.18), (3.20), (3.23) and (3.25), leading to eq. (3.36).

$$\begin{aligned} C_p =& -2\left[C_0+\frac{\eta(\theta_2-\pi)}{\pi}+\frac{\theta_1\sin\delta}{\pi}\right]\frac{\sin\theta}{\cos\theta_0-\cos\theta}+4B_0\sin\theta \\ & -\frac{2\sin\delta}{\pi}\ln\left\{\frac{\sin\frac{1}{2}|\theta-\theta_1|}{\sin\frac{1}{2}(\theta+\theta_1)}\right\}-\frac{2\beta}{\pi}\ln\left\{\frac{\sin\frac{1}{2}|\theta-\theta_2|}{\sin\frac{1}{2}(\theta+\theta_2)}\right\} \\ & +2\sum_1^\infty\sin n\theta+\frac{\sum_1^\infty N_n\sin n\theta}{\cos\theta_0-\cos\theta}-K \end{aligned} \tag{3.36}$$

Finally, the lift coefficient is calculated using eq. (3.10), with the Laurent series expansion of $F(z)$, per boundary condition 5, giving eq. (3.37). The completed equation is given by eq. (3.38).

$$C_l = \frac{4\pi}{c}\operatorname{Im}\left\{\text{coefficient of }\frac{1}{z}\right\} \tag{3.37}$$

$$\begin{aligned} C_l =& \frac{4\pi}{c}\operatorname{Im}\left\{iB_0la_1\left(1+\frac{1}{a_0^2}\right)-\right. \\ & i\left[C_0+\frac{\theta_1\sin\delta}{\pi}+\frac{(\theta_2-\pi}{\pi}\eta\right]\cdot la_1\left[\frac{e^{i\theta_0}}{\left(a_0e^{i\theta_0}-1\right)^2}+\frac{e^{-i\theta_0}}{\left(a_0e^{-i\theta_0}-1\right)^2}\right]+ \\ & \frac{\sin\delta}{\pi}la_1\left[\frac{1}{a_0-e^{i\theta_1}}-\frac{1}{a_0-e^{-i\theta_1}}\right]+\frac{\beta}{\pi}la_1\left[\frac{1}{a_0-e^{i\theta_2}}-\frac{1}{a_0-e^{-i\theta_2}}\right]+ \\ & \left.ila_1\sum_1^\infty\frac{nM_n}{a_0^{n+1}}+ila_1\sum_0^\infty N_n\frac{\left[\frac{1-n}{a_0}-\frac{e^{i\theta_0}}{a_0e^{i\theta_0}}-\frac{e^{-i\theta_0}}{a_0e^{-i\theta_0}}\right]}{a_0^{n-1}(a_0e^{i\theta_0}-1)(a_0e^{-i\theta_0}-1)}\right\} \end{aligned} \tag{3.38}$$

3.3.2. Verification of the Spoiler Aerodynamic Model

The linearized potential flow model given in the previous section was solved for arbitrary input using MATLAB. To verify the correct implementation of the aerodynamic model in MATLAB, computed results are compared to results presented by Brown and Parkinson [3] and Bernier [4]. For their purpose, Brown and Parkinson presented data obtained using a 355.6 mm chord Clark Y airfoil of 14% thickness.

Figures 3.7 and 3.8 show the lift curve for the previously mentioned Clark Y airfoil equipped with a 10% normal spoiler located at 70% of the chord. The latter also has a 32.5% flap deflected by 15 degrees In addition to the experimental and theoretical results, theoretical results for the method developed by Woods [62] are also given. The two figures show good agreement between the different theories and experiment in terms of trend and order of magnitude. The experimentally obtained cavitation numbers used for these calculations are found in table 3.3.

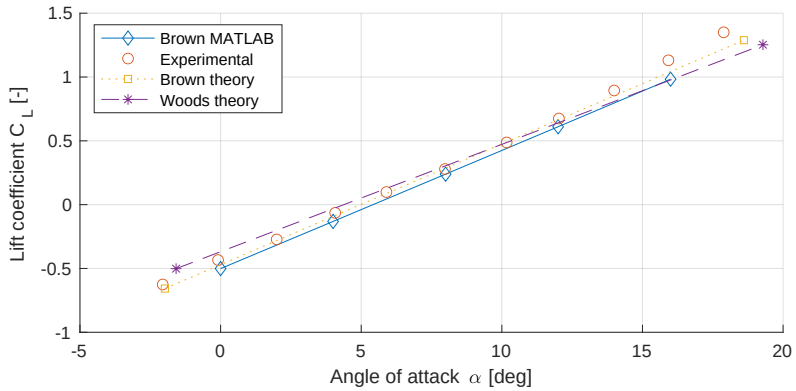

Figure 3.7: *Lift coefficient as a function of angle of attack for a Clark Y airfoil of 14% thickness with a normal spoiler of 10% chord located at 70% of the chord. Data taken from Brown and Parkinson [3].*

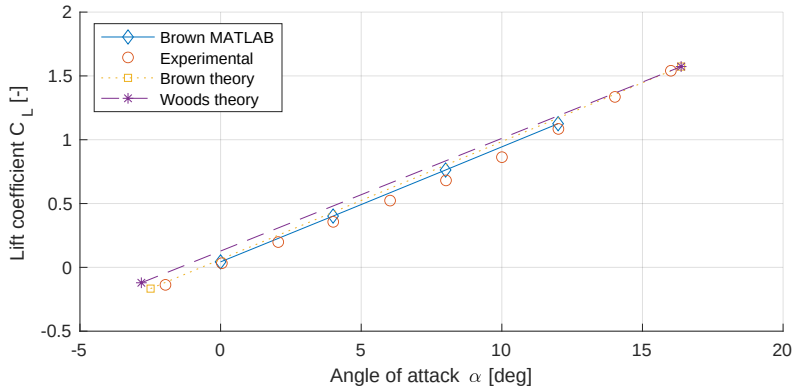

Figure 3.8: *Lift coefficient as a function angle of attack for a Clark Y airfoil of 14% thickness with a normal spoiler of 10% chord located at 70% of the chord and a 32.5% flap deflected by* 15 degrees. *Data taken from Brown and Parkinson [3].*

Table 3.3: *Experimentally obtained values for cavitation number K for figs. 3.7 and 3.8. Data obtained from Bernier [4].*

α [deg]		0	4	8	12	16
K [-]	$s/c = 0.7,\ h/c = 0.1$[1]	0.613	0.588	0.563	0.538	0.513
	$s/c = 0.7,\ h/c = 0.1,\ c_f/c = 0.325$[2]	0.742	0.693	0.644	0.595	0.546

[1] Used in fig. 3.7.
[2] Used in fig. 3.8.

The lift as a function of spoiler deflection angle is plotted in fig. 3.9. The cavitation numbers used for these calculations are given in table 3.4. Contrary to the previous two graphs, no data is given for

Woods' theory, since it only applies to normal spoilers. Both theoretical results show a similar trend compared to the experimental result. The theoretical data presented by Brown and Parkinson overestimates the experimental lift coefficient for lower spoiler deflections by approximately 20%, but the difference between the two decreases with increasing spoiler deflection, with the theory overestimating experimental data by 10% for a spoiler deflection of 90 deg.

The results are expected to closely match the theoretical results from Brown and Parkinson as they are obtained from a direct implementation of their theory, some differences are present however. The results obtained from the implemented model follow the same trend, but underestimate the lift coefficient compared to both theoretical and experimental results by Brown and Parkinson. The calculated lift coefficient is 4% smaller at 0 deg spoiler deflection and 13% smaller at a spoiler deflection of 90 deg, the maximum deviation of 30% occurs at 60 deg spoiler deflection.

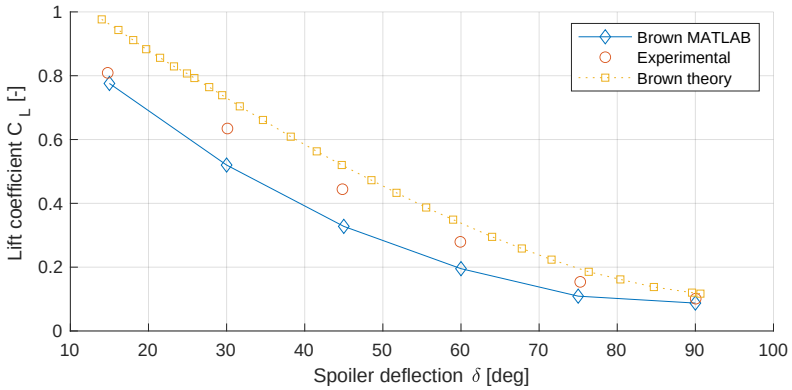

Figure 3.9: *Lift coefficient as a fuction of spoiler deflection angle at an angle of attack of* 6 degrees *for a Clark Y airfoil of 14% thickness with a 10% spoiler located at 70% of the chord. Data taken from Brown and Parkinson [3].*

Table 3.4: *Experimentally obtained values for cavitation number K for fig. 3.9, α =*6 deg*, $s/c = 0.7$ and $h/c = 0.1$. Data obtained from Bernier [4].*

δ [deg]	15	30	45	60	75	90
K [-]	0.290	0.388	0.420	0.503	0.550	0.576

4

Design and Development of the Experimental Wing Section

To investigate GLA, a wing section with control surfaces is required. Since the only available wing section for the aeroelastic test apparatus lacks any control surfaces, a new wing section had to be developed. This chapter details the design and development of the wing section with aileron and spoiler. Before the design is started, the design requirements will be defined in section 4.1. Section 4.2 lays out the design of the structural components of the wing section, followed by the mechanical and electrical systems and software design in sections 4.3 to 4.5 respectively. With all the design work shown, the final section of this chapter, section 4.6, deals with the production and final assembly of the wing section.

4.1. Design Requirements and Constraints

As with any design project, a clear overview of the design space is necessary. Requirements and constraint should be identified, such that at the end of the process, the delivered product will be able to fulfill its intended purpose. The following should be taken into account; since the wing section is intended for use with existing facilities, it must be compatible with the aeroelastic apparatus, such that the model can be tested in the M- and W-tunnels. The aeroelastic apparatus is used to mount the wing in the wind tunnel, providing the heave DoF through a pair of cantilever leaf springs on the top and bottom of the apparatus. A mechanism connected to the free ends of the springs connects to the wing section by means of an axle, providing the pitch DoF. A more detailed explanation of the aeroelastic apparatus is given in section 5.2.

To enable research on active control, the wing section shall be equipped with both aileron and spoiler control surfaces. The wing section shall be equipped with parametric devices, a free play mechanism in the aileron actuation mechanism and pitch axis location that can be changed along the chordwise direction. The former is included to investigate the effect of control surface free play on aeroelastic phenomena, the latter allows for the testing of different wing configurations, where the pitch axis is moved with respect to the center of mass and aerodynamic center, changing the stability of the system. Finally, the wing section shall be a self-contained unit, being equipped with instrumentation and a power supply. This limits the amount of external devices necessary for testing, enabling a quick setup time.

The current wing used with the aeroelastic apparatus has a NACA0012 profile, a 160 mm chord and 360 mm span. This is chosen as a starting point for the design, as its form factor has already been proven to work for the current setup. Based on the presented requirements, the wing should - at least - be able to fit a single-board computer, battery, two servo actuators and a freeplay mechanism. Looking

at the available options for the first three of these components, the BeagleBone Blue, two 550 mAh 1S LiPo batteries and the Blue Bird Model BMS-A10V were chosen. These components will be elaborated on in sections 4.4.1, 4.4.2 and 4.4.5.

Using 3D models of these components, it was quickly found that a NACA0012 profile, with a maximum thickness of 19.2 mm provided insufficient space for the components to be placed internally. In particular, the most crucial here being sufficient clearance for the movement of the servo horns. A NACA0014 was therefore chosen, providing an additional thickness of 3.2 mm.

Further driving the design is the size and placement of the control surfaces. Table 3.2 in section 3.1.2 provides an overview of used spoiler locations and lengths. Common lengths for spoilers used in experiments range between 10% and 15% of the wing chord and are located between 65% and 75% of the wing chord. Typical aileron chord sizes are between 20% and 25% of the wing chord. Taking these locations and dimensions into consideration, together with practical limitations such as tolerances, component size (bearings, axles, etc) and finite dimensions (i.e. skin thicknesses), a 25% chord aileron was chosen, together with a 13.5% chord spoiler, located at 60% of the chord length. The spoiler deflection angles ranges from 0 deg to 90 deg, the aileron ranges deflection from ±25 deg. An overview of the various relevant dimensions is given in table 4.1.

Table 4.1: *Wing model parameters.*

Wing chord length	c	160 mm
Wing span	b	378 mm
Aileron length	c_a	$0.25c$
Aileron deflection	β	±25 deg
Spoiler length	c_s	$0.135c$
Spoiler deflection	δ	0 deg-90 deg
Spoiler location	x_s	$0.60c$
Profile		NACA0014

4.2. Design of the Wing Structure

The main structure of the wing is designed using CATIA V5. It can be split in two primary components, the frame and skins, which are discussed in this section. First, the design of the wing skins covering the frames is treated. This is followed by the design of the frames of the wing, aileron and spoiler.

4.2.1. Wing Skins

The skeleton of the wing is clad with composite skins. The skins are made out of fiberglass and have a thickness of 0.5 mm. To facilitate sufficient access to the internal components of the wing, the rear part of the bottom skin is removable. To this end, magnets and a 0.2 mm steel shim are respectively laminated into the bottom leading edge and bottom cover, shown in fig. 4.1. In total, the skin has five unique components: the top skin, the bottom leading edge skin, the bottom cover, the spoiler and the aileron skins (top and bottom), all seen in fig. 4.2.

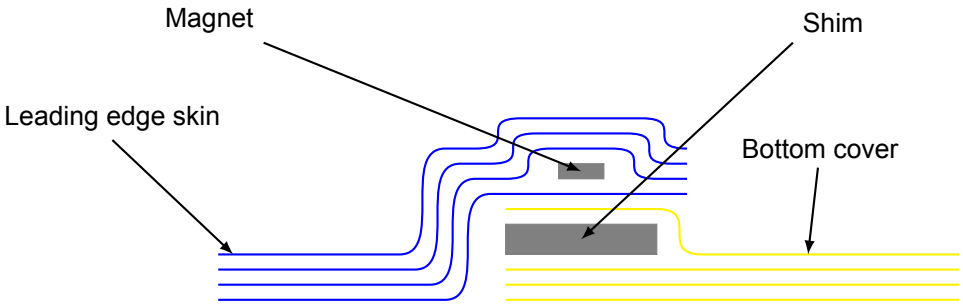

Figure 4.1: *Schematic of the connection between the bottom leading edge skin and bottom cover. The yellow and blue colored lines are the individual layers of fiberglass. N.B. for illustrative purpose only, schematic not to scale.*

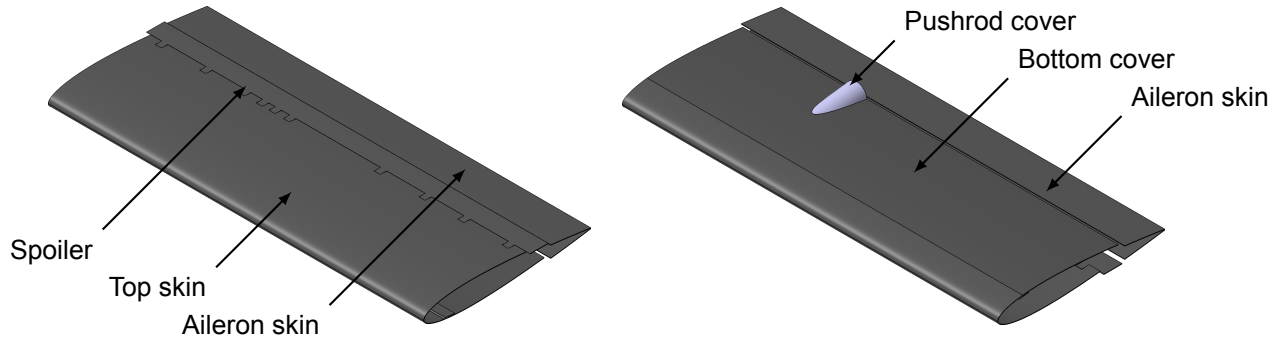

(a) *Top side of the skins.* **(b)** *Bottom side of the skins.*

Figure 4.2: *Renders of the wing skins.*

4.2.2. Wing, Spoiler and Aileron Frames

The wing frame is the main structure of the wing. When combined with the skins, the frames are the load-bearing structure. As a large part of the bottom skin is removable, the frame structure of the wing should provide sufficient stiffness to prevent deformation of the wing section.

The wing section has three separate frames, for the main wing, the aileron and for the spoiler, all seen in fig. 4.3. Each frame consist of chordwise ribs - in the shape of an airfoil for the main wing and aileron - and spanwise spars. Besides determining the outer shape of the wing section, the ribs are also modified accommodate the different internal components. For example, the outer ribs contain slots into which the mounting mechanisms are inserted on either side and the middle ribs provide a mounting point for the single-board computer of the wing, such that its inertial measurement unit measures the acceleration close to the center of mass of the wing. Spanwise, the ribs are distributed to accommodate the symmetric placement of the internal components as much as possible, preventing unwanted rocking motion of the wing section.

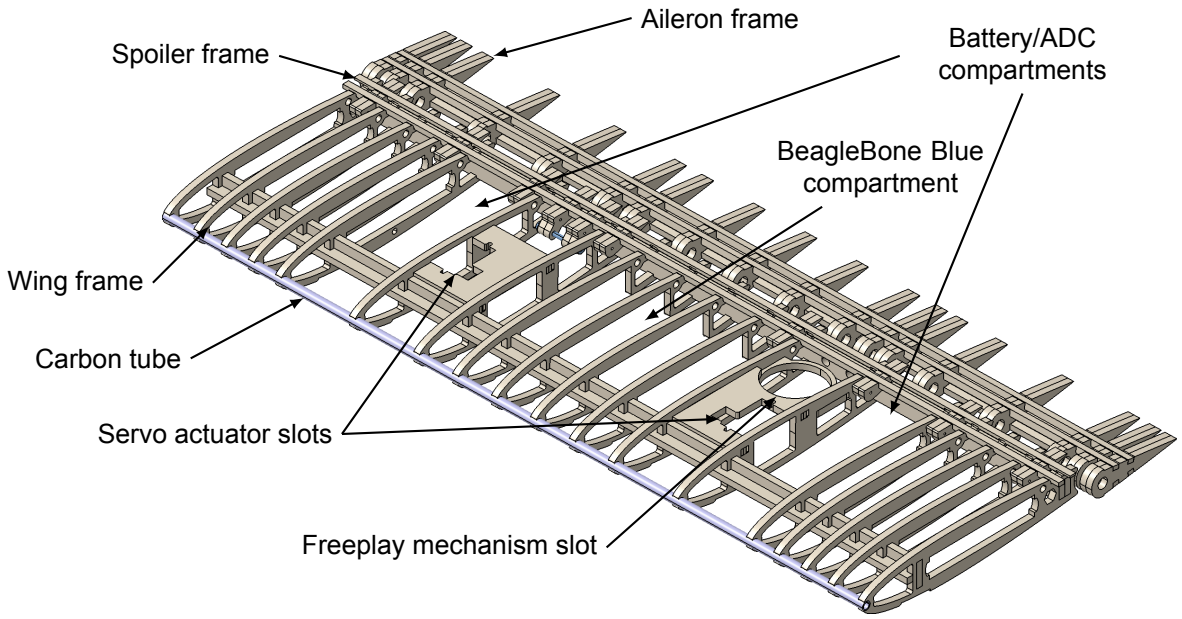

Figure 4.3: *Render of the wing, spoiler and aileron frames.*

Also visible in fig. 4.3 is a tube at the leading edge. This tube is made from extruded carbon fiber and serves both a structural member in addition to providing a convenient surface to attach the top and bottom skin to. The final noteworthy components of the main wing frame are the horizontal plates to which both servo actuators and the freeplay mechanism are mounted to.

4.3. Design of the Mechanical Systems

The three different mechanical systems present in the wing are discussed in this section. The first is the aileron actuation and freeplay mechanism. This is followed by the spoiler actuation mechanism. Finally, the suspension mechanism of the wing section is treated.

4.3.1. Aileron Actuation and Free Play Mechanism

The aileron actuation mechanism is shown in fig. 4.4. The wing section is equipped with a $0.25c$ aileron. The connection between the aileron and the main body of the wing section consists of a 3 mm diameter, spring steel axle, five rod end bearings and nine 5 mm outer diameter (OD) ball bearings. The rod end bearings are fixed in the rear spar of the wing, whereas the ball bearings are pressed into the wooden ribs of the aileron. This setup is chosen to ensure proper alignment of the aileron and limited rotational friction.

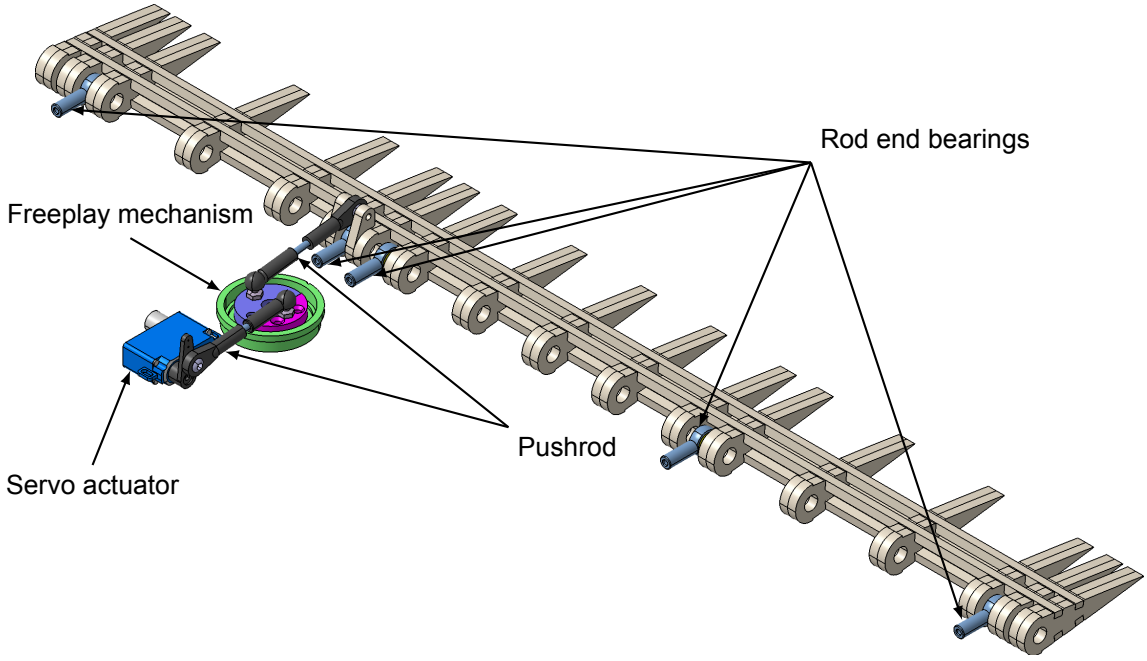

Figure 4.4: *Render of the aileron actuation mechanism.*

The aileron is connected to the servo actuator through two pushrods and a so-called freeplay mechanism (FPM). Free play is an important nonlinear aeroelastic phenomenon, which can be seen as a region of reduced or no stiffness in the control surface kinematics and trigger control surface limit cycle oscillations (LCO). In addition, it introduces an uncertainty with respect to the actual control surface position, where the actual control surface deflection is smaller or greater than the commanded deflection. Therefore tight tolerances are necessary in control surfaces, making free play a problematic issue when precise control is required, for example for GLA. To quantify the effects of free play on the different aeroelastic phenomena, the FPM is included in the wing section. The FPM can be seen in fig. 4.5. The mechanism consists of two semicircular blocks - input, connected to the servo and output, connected to the aileron - mounted in a casing. Both disks can rotate independently from each other and are connected to the casing using ball bearings, again to ensure limited friction.

The amount of free play in the mechanism is precisely controlled by the interchangeable input blocks. For 0 deg free play, the input block matches contour of the output block of the FPM. In principle the amount of free play is only limited by the screws holding the blocks in place, but up to that

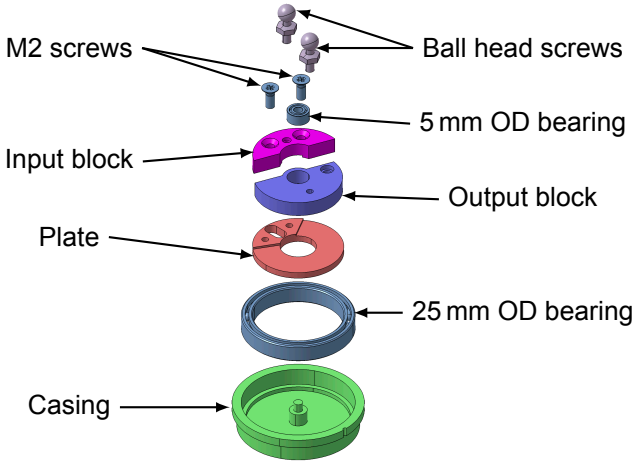

Figure 4.5: *Exploded view of the freeplay mechanism.*

limit any amount of free play is possible, including asymmetric amounts of free play if desired. Input blocks ranging from 0 deg to 20 deg in increments of 5 deg have been manufactured as a baseline set, but additional blocks may be manufactured in the future, depending on the experimental requirements. These blocks are shown in fig. 4.6.

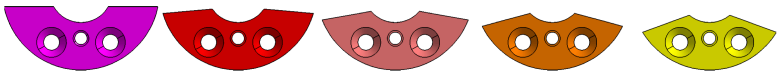

Figure 4.6: *FPM input blocks, from left to right: 0, 5, 10, 15 and 20 degrees freeplay.*

The pushrods are connected to the in- and output block of the FPM using ball-and-socket joints. The other end of the pushrods is connected to the aileron and servo horn respectively. Ball bearing ends are used for these joints, as the inclusion of the FPM introduces sideways motion in addition to the back-and-forth motion of the pushrods.

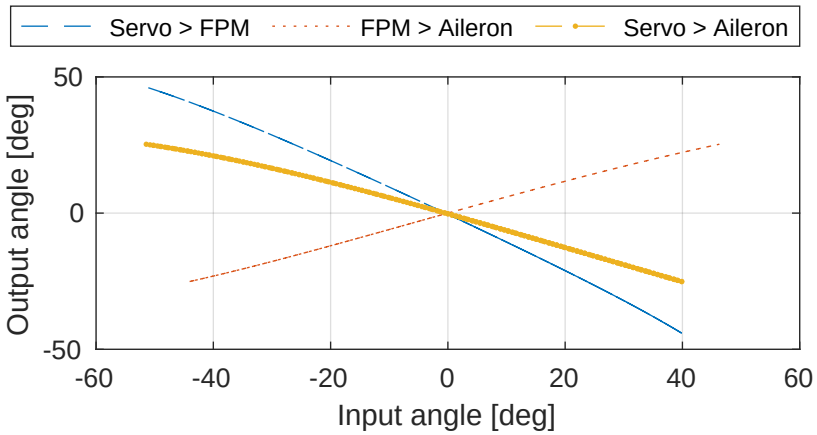

Figure 4.7: *Relation between input and output angles of the various components of the aileron actuation mechanism.*

The relations between the various input and output angles are plotted in fig. 4.7. The servo actuator input range from -51.4 deg to 39.9 deg maps to an aileron deflection of -25.1 deg to 25.3 deg. The curves mapping the servo actuator rotation to the FPM rotation and the FPM rotation to the aileron deflection show a nonlinear trend. The curve mapping the servo actuator deflection to aileron deflection shows mostly linear behavior for small deflections. For larger deflections the nonlinear behavior due to

the FPM becomes visible. This data is used later in the Simulink model to generate the correct servo actuator signal for the commanded aileron deflection.

4.3.2. Spoiler Actuation

A render of the spoiler actuation mechanism is seen in fig. 4.8. To prevent unwanted translations of the spoiler during its deployment, its rotational axis should be as close as possible to the wing skin. To accomplish this, while still ensuring minimal rotational friction, the spoiler is mounted to the wing using 3mm OD ball bearings, pressed into the wooden ribs of the wing. A 1 mm spring steel axle, passing through the bearings, is glued to the spoiler ribs.

As no FPM is included, this mechanism can be described as a planar, 3-bar link, consisting of the servo actuator arm, a pushrod and the spoiler arm. The relation between the servo actuator input angle and spoiler output angle is shown in fig. 4.9. The servo actuator input ranging from 0 deg to 61.8 deg maps to a spoiler deflection of 0 deg to 90deg. Similar to the aileron, this data is used in the Simulink model to generate the correct servo actuator signal for the commanded spoiler deflection.

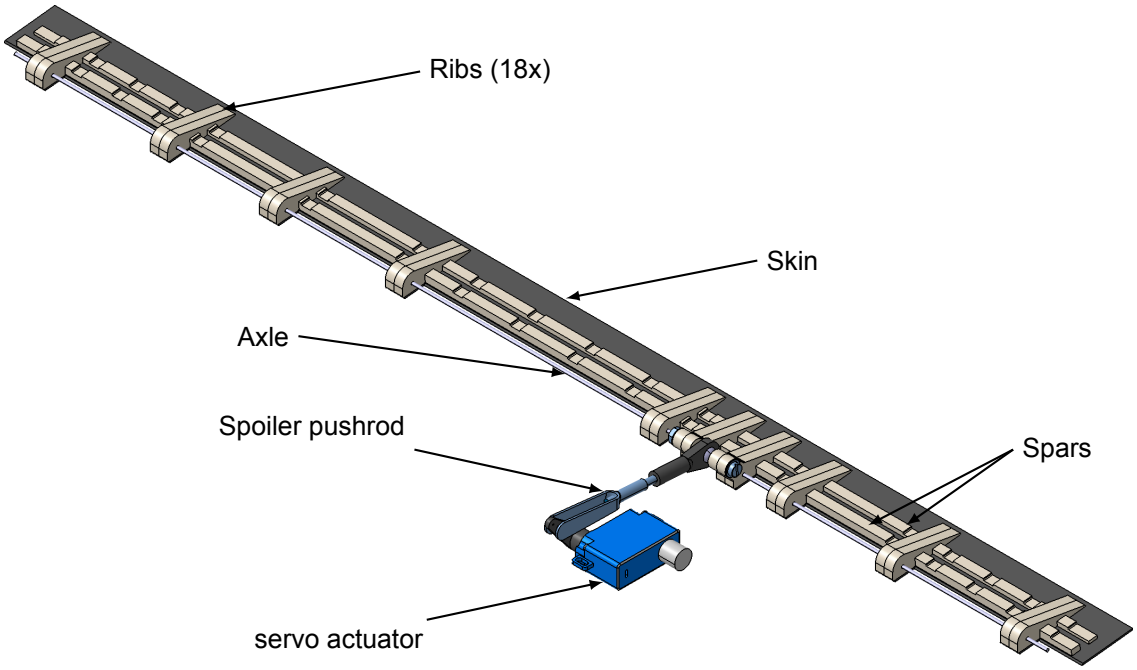

Figure 4.8: *Render of the spoiler actuation mechanism.*

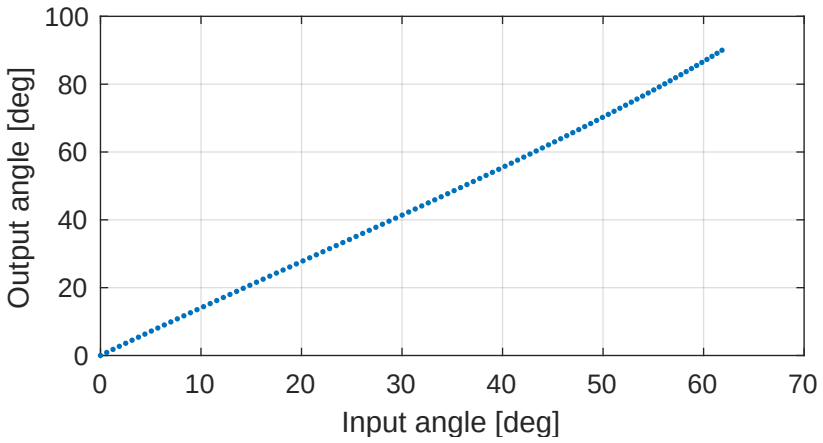

Figure 4.9: *Relation between the servo actuator angle and spoiler deflection angle.*

4.3.3. Wing Section Mounting

The wing section is designed for use with existing facilities. It is therefore desirable to reuse as much as possible of the suspension mechanism of the aeroelastic apparatus. The existing, passive wing is mounted to the pitch mechanism of the aeroelastic apparatus by an axle running through the entire wing. Due to the internal components of the new wing section, it is not possible to run an axle along its entire span, hence this part of the mounting is redesigned. An additional design goal was set for the mounting, to allow most of its parts to be reused with future wing sections.

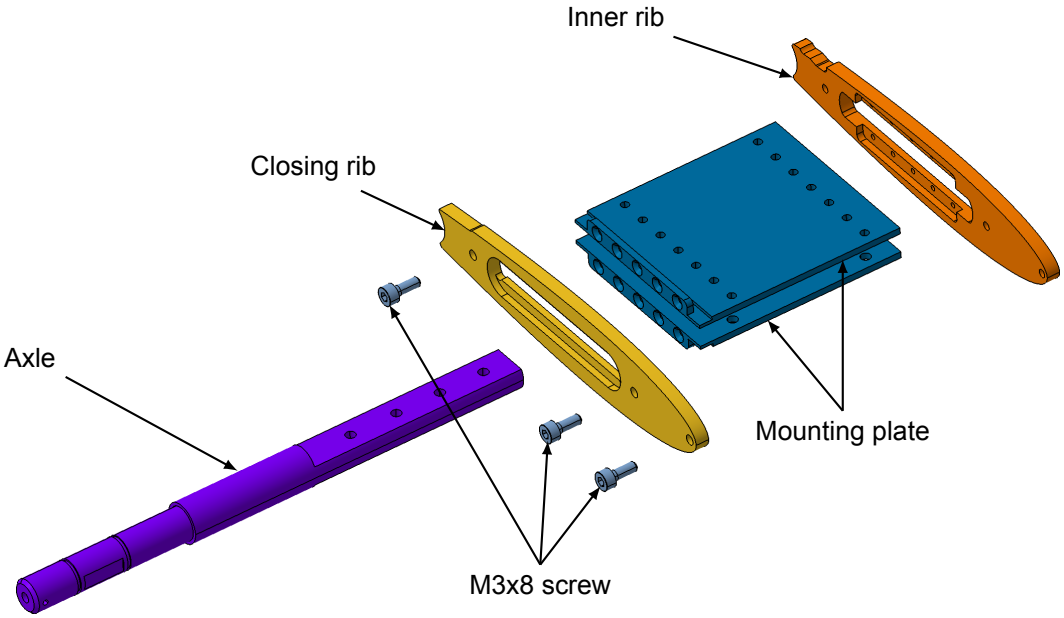

Figure 4.10: *Exploded view of the right-hand side mounting.*

Figure 4.10 shows the right-hand side of the new mounting assembly. The left-hand is identically mirrored, with the exception of the axle. The inner rib has the same airfoil outline as the wooden ribs. It is glued to the skin and outer wooden rib, making it the only component of the mounting assembly permanently fixed to the wing. A slot is machined on the top rear side of the rib to accommodate the spoiler structure and skin. To transfer the load from the axle to the wooden structure, two mounting plates are pushed into the wing, through slots in the inner rib and wooden ribs. The mounting plates are fixed to the inner rib using five countersunk M2 screws. Finally, a closing rib caps the wing off, connecting to the inner rib by means of three M3x8 screws. The closing rib has the a slot machined on its top rear surface to accommodate the spoiler skin.

The size of the mounting plates is driven by two primary factors: 1) the desired positions of the elastic axis, i.e. the axle and 2) the rigidity along the span of the wing section. The former was set to 25% to 55% of the chord in 5% increments, reflecting realistic positions for the elastic axis in a “real” aircraft wing. For the latter, the least amount of spanwise deformation is desired due to several reasons. First and foremost, deformation may damage the wing. Secondly the aerodynamic model relies on the assumption of two-dimensional aerodynamics, requiring the wing section to be as uniform as possible. Finally, any spanwise deformation of the wing may also deform the aileron and spoiler axle, increasing the friction in these mechanisms.

To see the impact of the span of the mounting plates, a rudimentary and conservative Finite Element Analysis (FEA) was performed. The maximum lift coefficient was determined in XFOIL for a flow velocity of 30 m/s at standard sea level conditions. This lift coefficient was then used to create a distributed load on a simple two-dimensional model with 1000 beam elements with fixed boundary conditions on both ends. For the sectional properties of the elements, only the front and rear spar and the plates themselves are taken into account. Area moments of inertia of the individual components are summed together for each beam element, the Young’s modulus is area-averaged. The FEA was performed for four different plate lengths, ranging from 19 mm (spanning two ribs) to 61 mm (spanning five ribs). The displacement along the span for these arrangements is plotted in fig. 4.11.

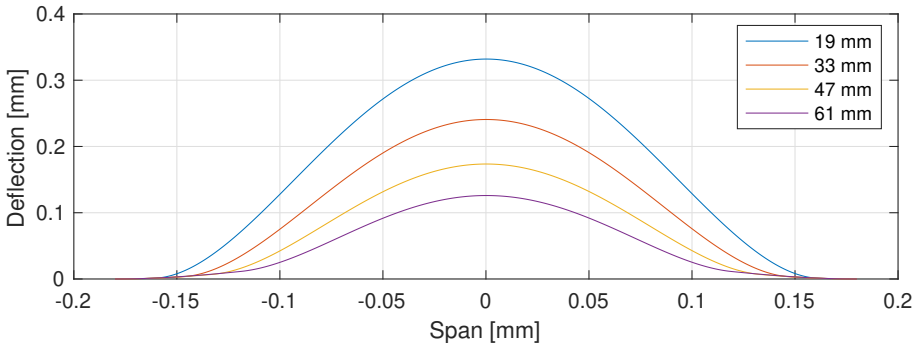

Figure 4.11: *Displacement along the span of the wing for mounting plate lengths ranging from* 19 mm *to* 61 mm.

4.4. Design of the Electrical System

The wing electrical system contains several different components outlined below. First the computer of the wing is discussed, then the servo actuators are treated. This is followed by the analog-to-digital converters (ADCs) and sensors. Finally, the wiring of the electrical system is discussed.

4.4.1. BeagleBone Blue

The BeagleBone Blue (BBBlue), seen in fig. 4.12, is a linux-based, single board computer, about the size of a credit card (88.9 mm x 54.61 mm). The BBBlue is specifically designed for robotics and educational applications. Compared to regular microcontrollers, the BBBLue is deemed an ideal candidate as the “central nervous system” of the wing as it incorporates the computer, a 9-axis inertial measurement unit and connectors for actuators and peripherals together with wireless communications into a compact package. Detailed specifications can be found below in table 4.2.

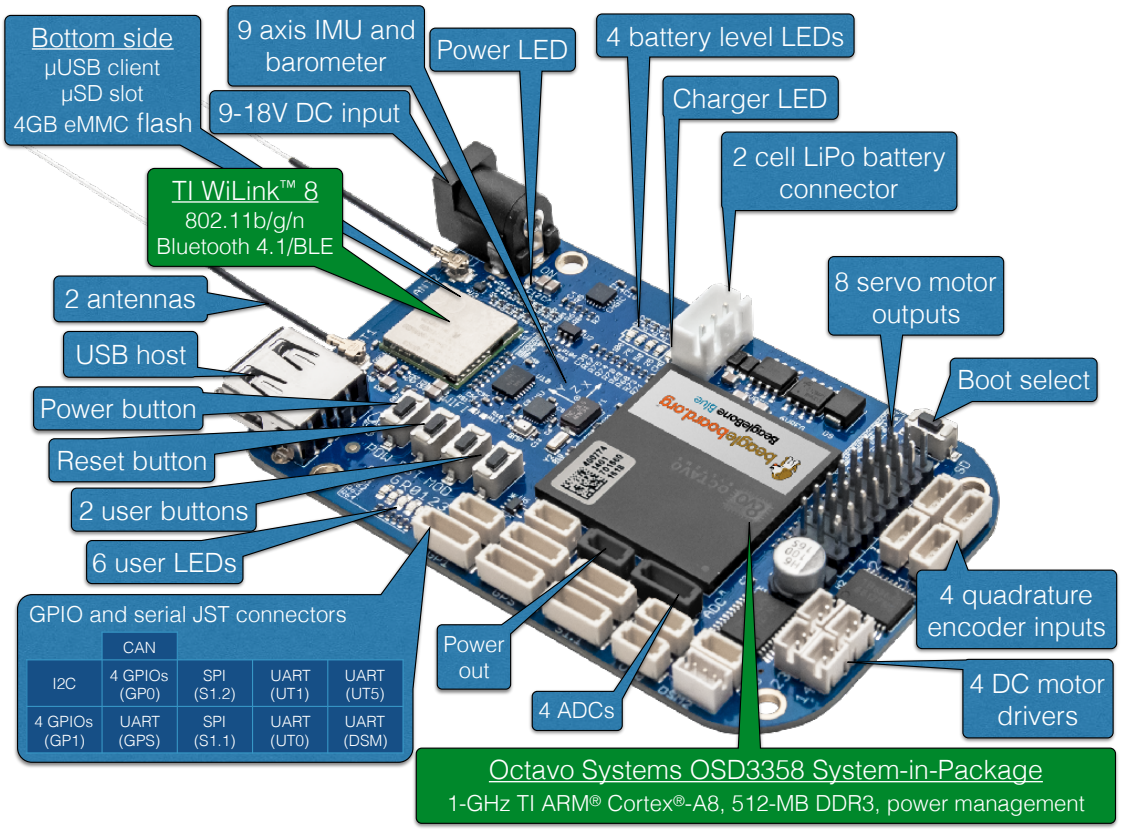

Figure 4.12: *Overview of the input/output connections on the BeagleBone Blue. Taken from [64].*

Table 4.2: *BeagleBone Blue specifications.*

Property	Specification
Processor	AM335x 1GHz ARM Cortex-A8
Memory	512MB DDR3 RAM
Storage	4GB
Programmable Realtime Unit (PRU)	2x 32 bit, 200Mhz
Power	2S LiPo/USB/9-18VDC 5mm barrel connector
Sensors	9-axis IMU, barometer, thermometer
Motor control	8x 6V servo channels, 4x DC motor, 4x quad encoder
I/O	USB, I2C, SPI, UART, CAN, GPS, GPIO, 1.8VDC ADC
Wireless	WiFi, Bluetooth

For this work, the following ports were used: A GPIO port is used to record the trigger signal generated by the gust generator. The I2C port connects to multiple ADCs, as detailed in section 4.4.3. The 9-axis inertial measurement unit (IMU) measures the movement of the wing. Two of the eight servo actuator channels are used to control the servo actuators.

The BBBLue can be powered through USB, a 5.5 mm DC barrel connector or a double cell (2S) lithium polymer (LiPo) battery. Only the latter options can be used when using servo actuators, also satisfying the design requirement for the new wing section to be a self-contained package. 2S LiPo batteries usable dimensions for the wing section can constitute up to 10% of the total weight of the wing and this mass cannot be placed near the center of mass as the IMU is placed here. To allow for a symmetric distribution of mass, two single cell (1S) LiPo batteries are used, placed on either side of the wing and connected in series to the BBBLue, giving the same performance as a 2S LiPo battery.

4.4.2. Servo Actuators

Servo actuator are electromechanical actuators with internal position control. They are used to actuate the control surfaces of the wing section. Two key performance parameters of a servo actuator are its torque and speed, which are inversely related. Larger servo actuators generally deliver higher torque and are able to operate at higher speeds due to the increased size of the motor.

The choice of a servo actuator for the wing section is a trade-off between size and performance. Ideally, the actuator has a high speed, as this increases the frequency bandwidth for control. The provided torque should be sufficient to keep the control surfaces deflected into the oncoming flow. Due to the limited available space inside the wing section, micro servo actuators were deemed suitable for this application, as these are commonly used in model aircraft. Several commercially available servo actuators are compared in table 4.3. Of the servo actuators with a deflection speed for 0.10 s per 60 deg, the BMS-A10V, seen in fig. 4.13, clearly has the best performance, having triple the amount of torque at the same speed compared to the HS-40, which has a comparable size. The BMS-A10V has 50% more torque compared to the S0009 MG, which is more than twice as large. Only the DITEX EL0315M outperformes the BMS-A10V, albeit this servo actuator is not only twice as large, but also slower. The specifications of the BMS-A10V are found in table 4.4.

Servo	Length [mm]	Width [mm]	Height [mm]	Torque [Ncm]	Speed [s/60 deg]
BMS-A10V	22	15.3	8	23.5	0.10
S0009 MG	32.7	30.9	12	15	0.10
DITEX EL0315M	29.7	23	12	37.3	0.13
Hitec HS-40	20	17	8.6	7.6	0.10

Table 4.3: *Comparison of commercially available servos. Torque and speed values given for* 6 V *input voltage.*

As becomes clear from the data presented in this table, servo actuator performance increases with increasing supplied voltage. The maximum charge of a 1S LiPo battery is 4.2 V, so with two 1S batteries connected in series, it can be determined from table 4.4 have a torque greater than 2.4 kgcm and a speed faster than 0.1 s/60 deg.

The position of the servo actuator is internally controlled, based on the external input signal. The position of a servo actuator is read by an internal sensor, for example with a potentiometer or with

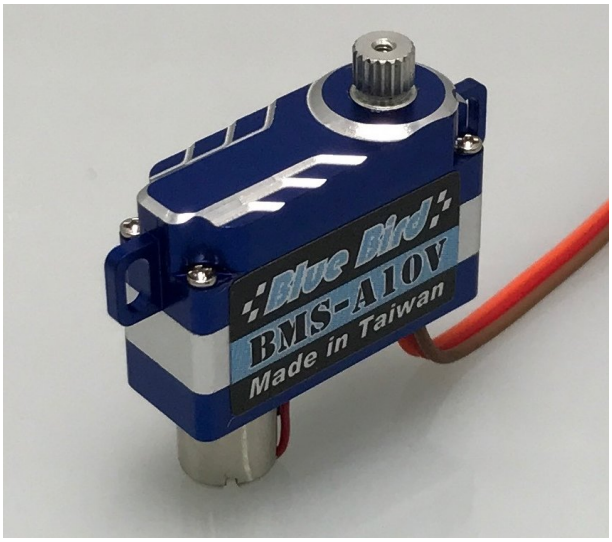

Figure 4.13: *The Blue Bird Model BMS-A10V servo actuator.*

Table 4.4: *Blue Bird BMS-A10V servo actuator specifications.*

Voltage [V]	Torque [kg cm]	Speed [s/60 deg]
3.7	1.6	0.15
6.0	2.4	0.10
7.4	2.9	0.08
8.4	3.2	0.07

a rotary encoder. In the case of the BMS-A10V, a potentiometer is used. It is important to monitor the position of the actuator in certain applications, such as for comparing the commanded position versus the actual position in control applications or for the purpose of system identification as detailed in section 5.3.1. To accomplish this, the servo actuators were modified such that their position can be monitored.

4.4.3. Analog-to-Digital Converters

As mentioned in section 4.4.1, the BBBlue is equipped with an onboard 12-bit ADC, limited to single-ended (i.e. single polarity) 1.8 VDC signals. The output signal of the servo actuator potentiometers ranges between approximately 2 VDC and 4 VDC, and is therefore incompatible with the BBBLue ADC without modification. One solution is to scale the output signal using a voltage divider, with a potential loss in signal resolution, the other option is to use an external ADC, connecting to one of the communication busses of the BBBLue. This latter option was chosen, using the Texas Instrument ADS1015 12-bit ADC chip, as this allows the raw signal from the servo actuator to be used without any scaling. Further benefits of this option are the additional user programmable settings (such as sampling rate and single-ended versus differential signals) and the availability of higher resolution ADCs, such as the 16-bit ADS1115 chip. Figure 4.14 shows the breakout board with the ADS1015 ADC chip, its specifications are given in table 4.5. The ADC is connected to the BBBLue through its I2C interface. In total two ADCs are positioned inside the wing, one per servo actuator, to read the actuator position. For this application, the ADCs were used in single-ended mode with the full-scale range set to ±4.096VDC.

During testing an external linear variable differential transformer (LVDT) was connected to the BB-Blue to monitor heave displacement and use this signal together with the acceleration to improve the accuracy of the determined heave h, heave rate $\dot{h}$ and heave acceleration $\ddot{h}$ states using sensor fusion. The BBBlue has a logic level of 3.3VDC, therefore limiting the analog input voltage to ±3.3VDC. A voltage divider, schematic in fig. 4.15, was placed between the ADC and LVDT to make the LVDT compatible with the ADC. As the output signal of the LVDT can also have reversed polarity, the ADC was configured for a differential input. The exact settings for the ADCs in single-ended and differential mode can be found in tables A.1 and A.2 respectively in appendix A.

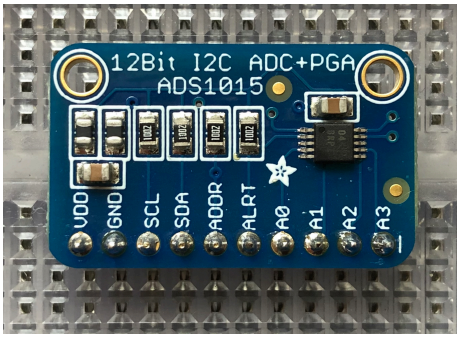

Figure 4.14: *Adafruit ADS1015 12-bit ADC breakout board.*

Table 4.5: *TI ADS1015 12-bit analog-to-digital converter specification.*

Property	Specification
Supply voltage VDD [VDC]	2-5.5
Analog input voltage range VAIN [VDC]	±0.256-±6.144
Sampling rate [SPS]	128-3300
Channels	2x differential/4x single-ended

4.4.4. Instrumentation

To detect and record the motion of the wing in response to a gust, a 9-axis IMU and a linear and rotational variable differential transformer (LVDT/RVDT). The data of the IMU is used as input for the control system and saved directly to the BBBLue, the LVDT/RVDT data was solely monitored and recorded on a separate computer. A summary of the used sensors is found in table 4.6. The 9-axis IMU is the MPU9250, capable of measuring the accelerations (in m/s^2) and magnetic field strength (in µT) along, and the angular rates (in deg/s) around the x-, y- and z-axis. The IMU is run in its digital motion processing (DMP) mode, providing the normal acceleration a_z and pitch rate $\dot{\theta}$ as measured inputs and pitch angle θ as derived input for the control system. The IMU is sampled internally at a rate of 200Hz in DMP mode.

The aeroelastic test apparatus is equipped with both an LVDT and RVDT. These are used to externally register the heave and pitch of the wing during testing. During testing, an attempt was made to use the LVDT as an input for the control system. Initial attempts performed with the wind tunnel not running showed promising results, however when the wind tunnel was turned on, electrical interference on the power grid caused the LVDT data to be corrupted to the extent that it was causing the BBBLue to crash constantly. This issue could not be resolved during the wind tunnel campaign.

4.4.5. Wiring

An overview of all the electrical connections between the BBBlue and other components can be seen in the wiring diagram in fig. 4.16. As mentioned before, the whole system is powered by two 1S LiPo batteries. The BBBlue itself provides only 6 VDC to servo actuators. As shown earlier in table 4.4, the servo actuators have greater performance when powered by a higher voltage signal and are therefore

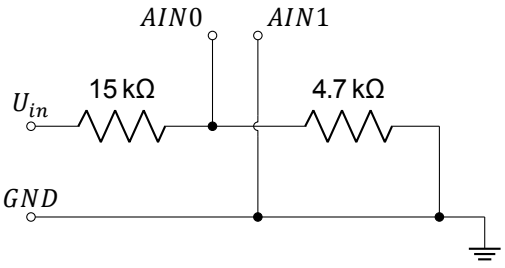

Figure 4.15: *Schematic of the voltage divider used for the LVDT. U_{in} and GND are taken from the LVDT, $AIN0$ and $AIN1$ are the analog inputs to the ADC.*

Table 4.6: *Overview of the sensors used in the experiment.*

Sensor		Measurement
MPU9250	9-axis IMU	a_z, $\dot{\theta}$
SenTech 75DC-1000	LVDT	h
Midori MAC QP-2HC	RVDT	θ

connected directly to the batteries, with only the servo actuator signal cable connecting directly to servo signal pins of the BBBLue. The final connection of each of the servo actuators is the measured position signal, which is connected to its respective ADC.

The two ADCs are connected to the single I2C port on the BBBlue. The ADC addresses are user-configurable, by connecting the ADDR pin to either VDD, GND, SCL or SDA pin. In this case, the VDD and GND are connected to the ADDR respectively.

As data is recorded on two separate systems, time-synchronization is necessary between the data sets. To facilitate the data synchronization, the gust generator generates a trigger signal that is recorded by both the BBBLue and external computer logging the LVDT/RVDT data. The trigger signal is recorded on the BBBLue by one of its digital input pins.

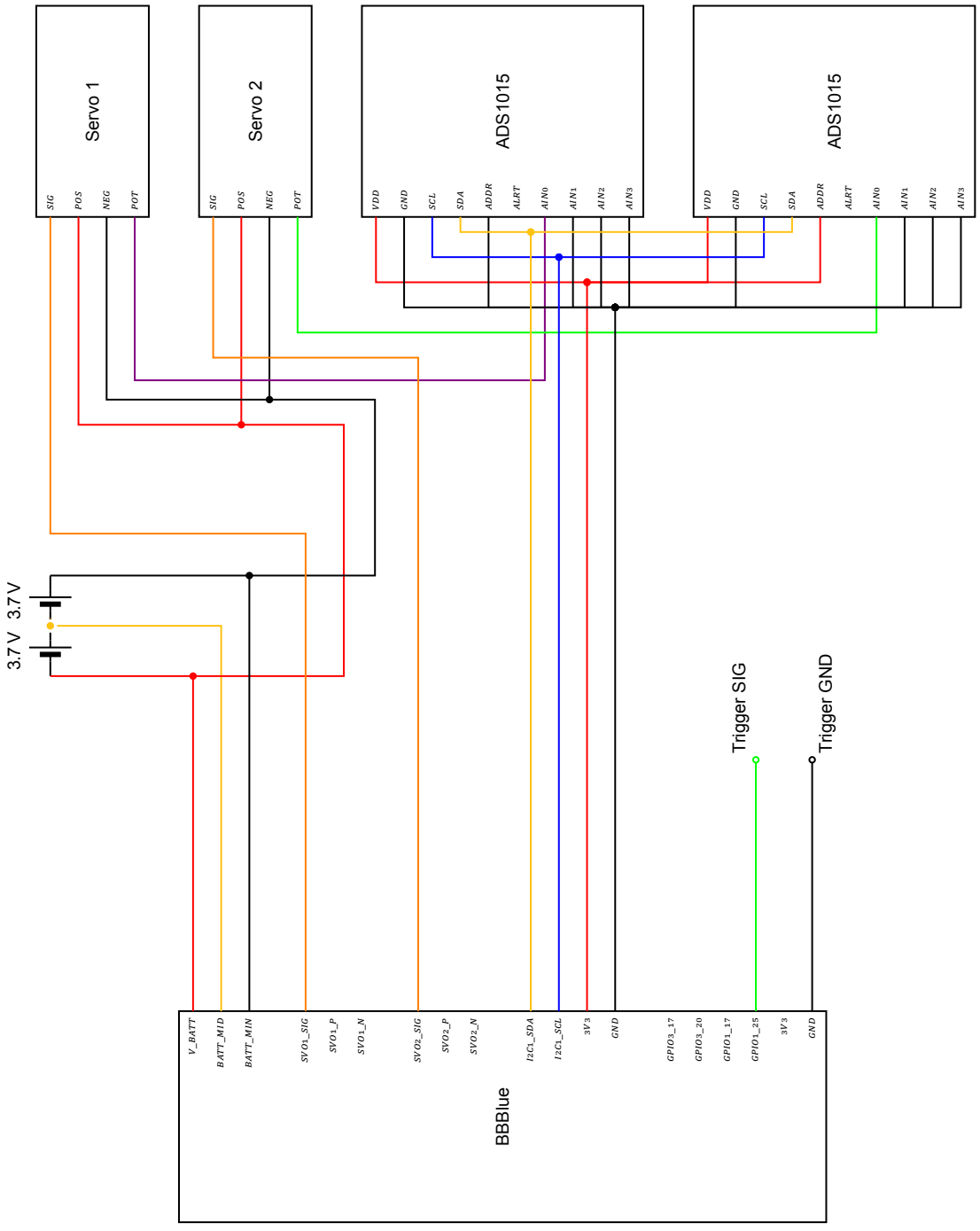

Figure 4.16: *Wiring diagram of the electrical parts in the wing. Note that the Trigger GND and Trigger SIG connect to the trigger signal generated by the gust generator.*

4.5. Software Development

The Beaglebone Blue runs on the *armhf* port of the Debian Linux distribution. Using *Debian 9.5 IoT 2018-10-07* release and the *Simulink Coder Support Package for BeagleBone Blue Hardware*, the BBBlue can be configured to run MATLAB/Simulink models. With this support package ANSI/ISO C/C++ code can be generated, compiled and executed on the BBBlue.

The major advantage of this method is the “plug-and-play” nature of Simulink’s block diagram models, allowing for impromptu changes to the control system. With Simulink’s extensive libraries containing mathematical, communication and control functions, models can be made quickly, without much - if any - manual programming.

The main block diagram, shown in fig. 4.17, is the program that is executed in Simulink. The program, together with its subsystems, is compiled and deployed upon execution. The function of this block diagram is to control the execution of the separate subsystems and relay the control signals generated by these subsystems to the aileron and spoiler servo actuator subsystems. The items indicated in (red) in fig. 4.17 are:

(1) The *enabled subsystems* (discussed under item 2.) are - as their name implies - enabled by a binary signal, which is generated based on the simulation time. The *unit delay* (2.1) combined with the *NOT* block (2.2) activate the *system initialization* subsystem during the first sample period of the execution. The *run system* subsystem is enabled between the end of the first sample period and the execution run time using the *AND* logical operator block (2.3). Finally, after the experiment run time has elapsed, the final subsystem is activated.

(2) Three *enabled subsystems* contain the block diagrams of the program in charge of data logging and generating the servo actuator control signals. Only one of these *enabled subsystems* can be operational at any given time.

(3) Each individual *enabled subsystem* generates its own control signals for the aileron and spoiler. The *merge* blocks are used to combine these three signals into a single signal per control surface actuator.

(4) The aileron and spoiler control signals are passed on to their respective servo actuator control subsystem, seen in detail in figs. 4.21 and 4.22.

All *enabled subsystems* have both aileron and spoiler *reference angle* as output. The respective outputs of the *enabled subsystems* are fed into *merge* blocks, to generate a continuous control signal for both aileron and spoiler throughout the entire run of the experiment. These single control signals are then fed to the aileron and spoiler *servo actuator subsystems*.

As mentioned before, the *system initialization* subsystem is enabled during the first sample period of the experiment. Upon activation, this subsystem, seen in fig. 4.18 performs two actions:

(1) *I2C master write* block writes a 16-bit value (see table A.1 in appendix A) to the configuration register of the two ADCs.

(2) *servo actuator position* sets the control surfaces to their respective non-deflected or zero positions.

The part of the program used to control the wing is the *run system* block. Figure 4.19 shows the block diagram of this subsystem. The indicated items are the following:

(1) *Digital read* block reads the trigger signal generated by the gust generator.

(2) *I2C master read* blocks read the value from the conversion register of the ADCs.

(3) *MPU9250* block controls the MPU-9250 IMU and outputs the accelerations, angular rates and Euler angles.

(4) *Constant* blocks give the reference values for the control system. Since stability is desired, the reference value is set to zero for both the acceleration and pitch rate.

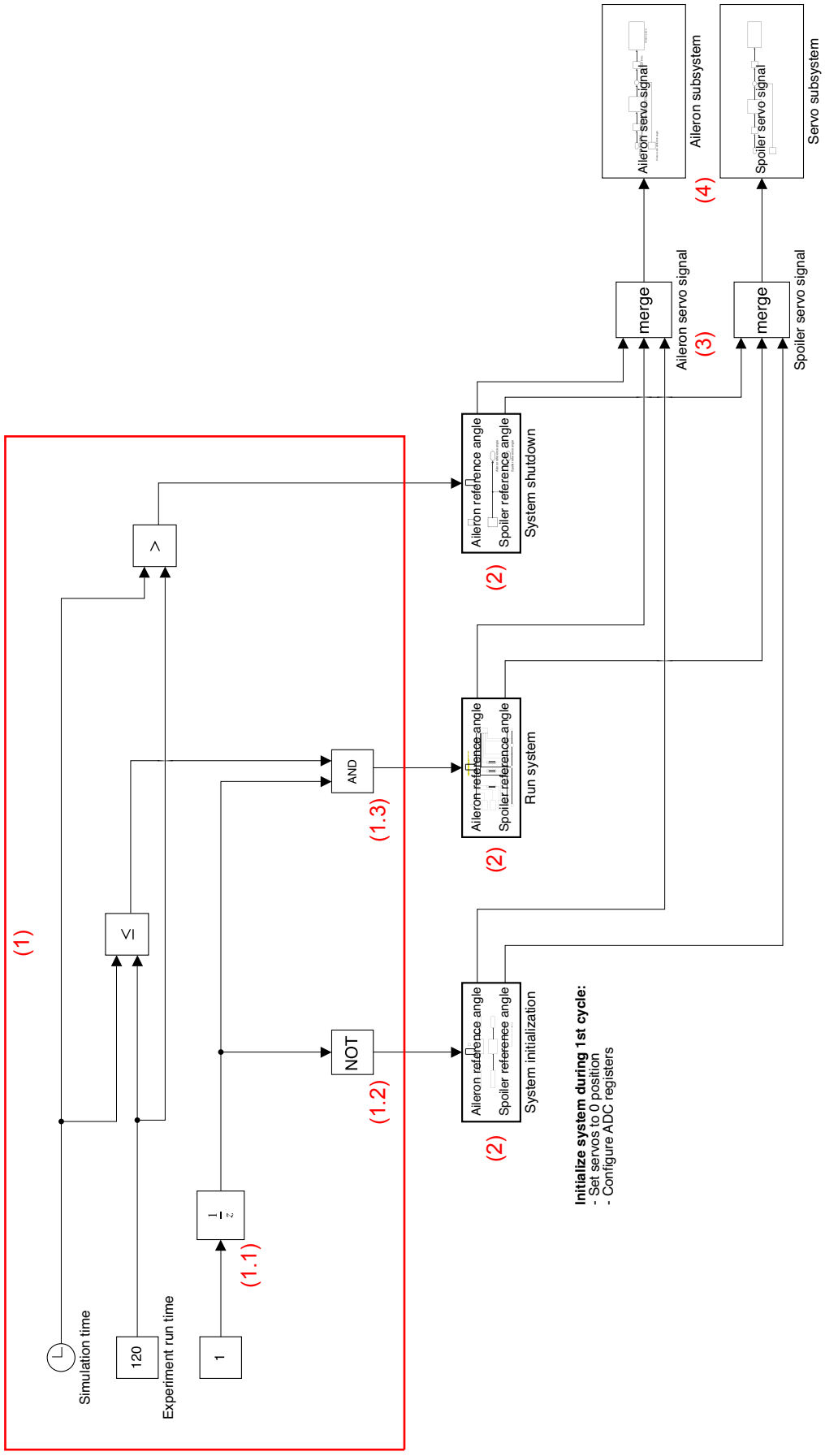

Figure 4.17: *Simulink block diagram of the main model.*

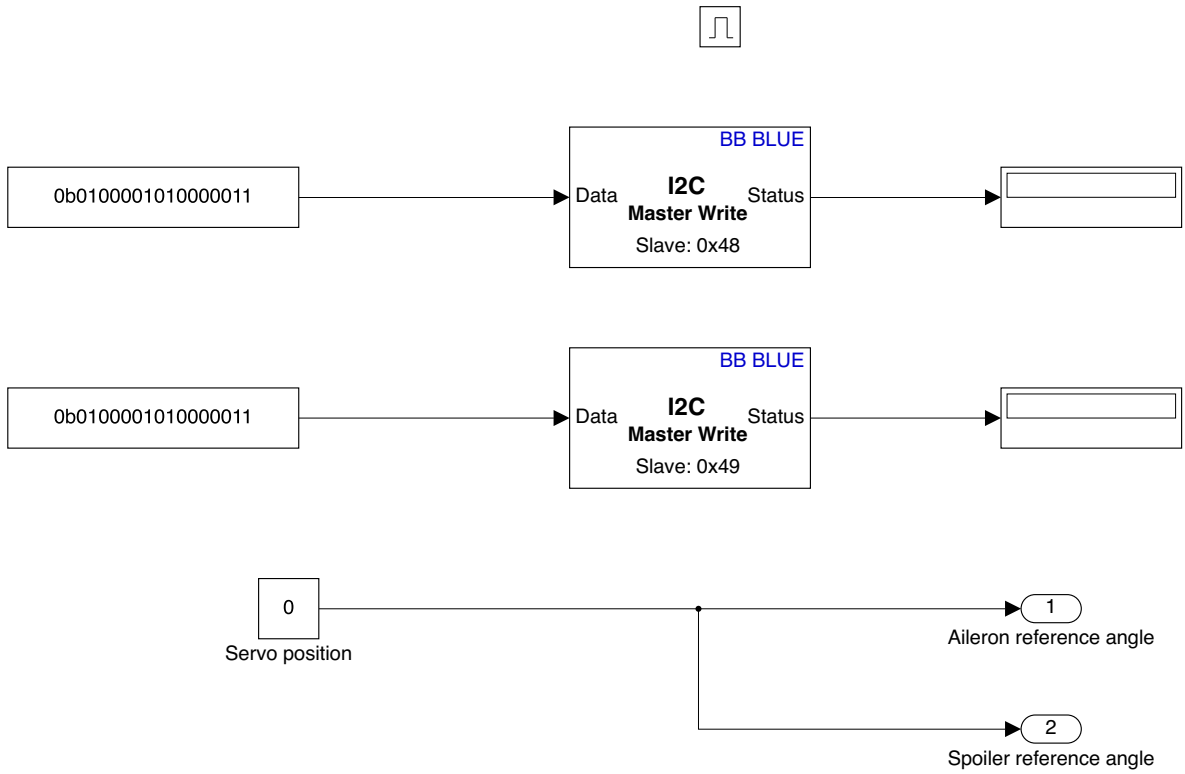

Figure 4.18: *Simulink block diagram of the initialization subsystem.*

(5) *Demux* (or demultiplexer) blocks split signals in their respective components. Any unused signals are capped with a terminator block, for example: the acceleration output of the IMU is a vector with accelerations in the x-, y- and z-direction. Only the z-direction is used, thus the accelerations in x- and y-directions are terminated.

(6) *PID controller* blocks contain the gains for aileron and servo actuator reference angle signals. Each control surface has each own PID control, as PID control is single-input single-output (SISO) process. Furthermore this allows for the gains to be independently set when using both the aileron and spoiler control surfaces.

(7) *Scope* block allows all connected signals to be viewed in (near) real-time. Additionally, the scope block also logs the connected signals to a MAT-file, the data container format used by MATLAB.

After the experiment run time has elapsed, the *system shutdown* subsystem, fig. 4.20 is executed. This subsystem resets the control surfaces back to their zero position.

The output of the enabled subsystems is routed, through the merge blocks, to the aileron and servo actuator subsystems, figs. 4.21 and 4.22. As these blocks operate under the same principles, the following description applies to both figures:

(1) A *lookup table* block maps the desired control surface deflection to the required servo actuator deflection. Nonlinearities are introduced due to the mechanisms connecting the control surfaces to the servo actuators, necessitating this mapping. The mapping data is obtained using the kinematics workbench in CATIA V5 and was shown earlier in figs. 4.7 and 4.9 for the aileron and spoiler respectively.

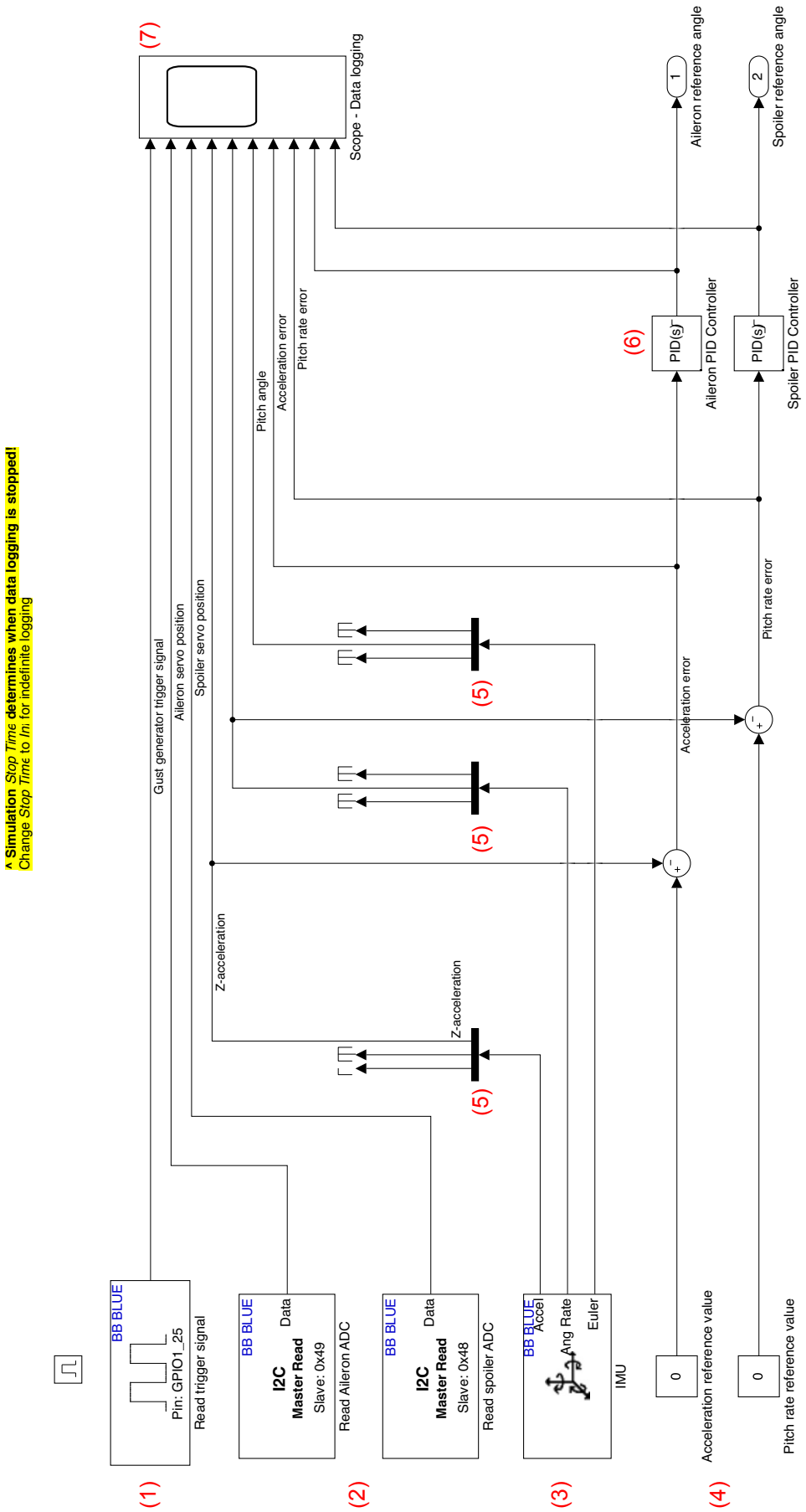

Figure 4.19: *Simulink block diagram of the run subsystem.*

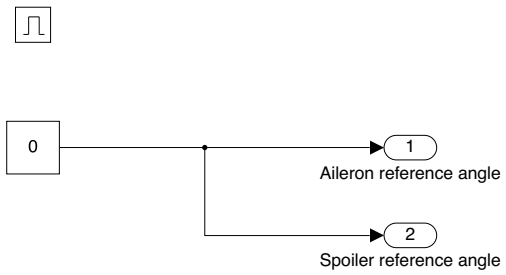

Figure 4.20: *Simulink block diagram of the shutdown subsystem.*

(2) *Saturation* blocks are placed both before the lookup table and servo actuator blocks. The first prevents that out of bounds values are requested from the lookup tables. If an out of bounds value gets through to the servo actuators, they are still protected by the latter saturation block, ensuring the servo actuators stay within their physically safe limits, preventing damage to the hardware.

(3) An additional offset is used to map the servo actuator input signal to the appropriate range, as the input for the servo actuator block ranges from 0 deg to 180 deg and the actual servo actuators range from −60 deg to 60 deg,

(4) The *servo actuator* blocks relay the input signals to the servo actuator headers on the BeagleBone.

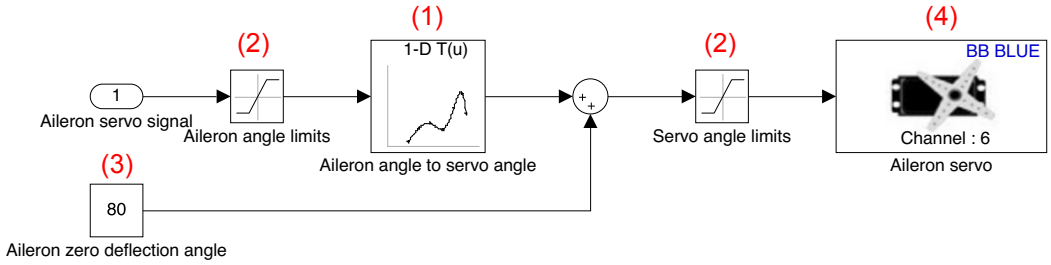

Figure 4.21: *Simulink block diagram of the aileron subsystem.*

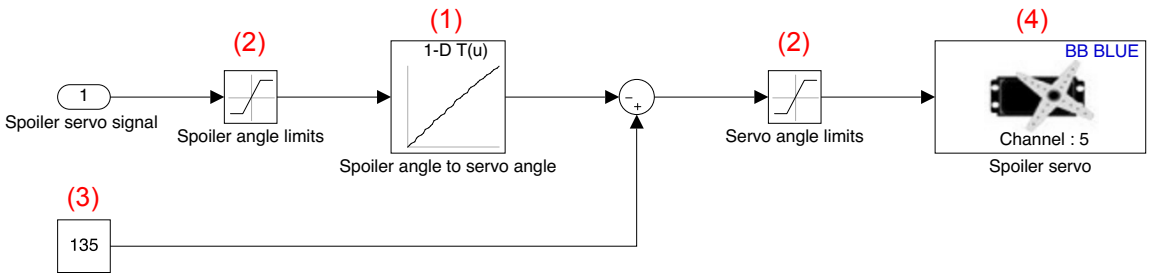

Figure 4.22: *Simulink block diagram of the spoiler subsystem.*

4.6. Manufacturing of the Wing Section

This section details the production of the wing section. The production of the skeleton is discussed in section 4.6.1. This is followed by the production of the composite wing skins in section 4.6.2. Section 4.6.3 treats the final assembly and shows the finished product.

4.6.1. Manufacturing of the Frames

The skeleton is designed to consist of strictly 2-dimensional components, such that these can be laser cut from a sheet of 3 mm thick, aircraft grade, birch plywood. The individual part outlines, with an additional offset to account for the diameter of the laser beam, are collected in a CATIA drawing after which the drawing is processed to the required format for laser cutting. The finished laser cut product can be seen in fig. 4.23.

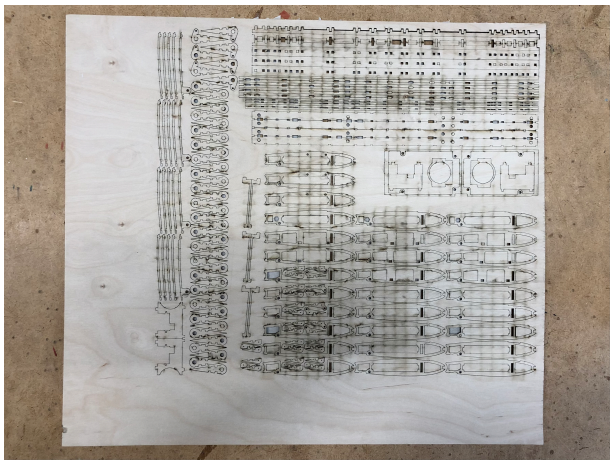

Figure 4.23: *The components of the wooden skeleton laser cut from a sheet of aircraft grade plywood.*

The main advantage of this method is its quick turnaround time - generally 48 hours between submission and pickup - allowing for the rapid prototyping of a sturdy skeleton at relatively low cost. One note of caution though, the diameter of the laser beam must be taken into account when creating the part outlines for cutting.

After the laser cutting is finished, the cut parts are removed from the sheet, inspected and cleaned using sandpaper to remove the soot and residue produced by the laser. All laser cut parts are then dry fitted, removing any necessary material using sandpaper or scalpel if the fit is too tight. The fit of the different bearings is also checked at this point. When the whole assembly properly fits together, wood glue is applied to the joints to fix the parts in place. For the assembly of the aileron, additional steps are required. The leading edge of the aileron was made by gluing pieces balsa rod to the skeleton after which these balsa pieces are sanded smooth to match the curvature of the aileron ribs.

4.6.2. Production of the Skins

To produce the skins of the wing and control surfaces, a mold was machined out of polyurethane tooling foam (SikaBlock(R) M945). The mold was prepped with wax, followed by a layer of polyvinyl alcohol (PVA). The machining of the mold leaves behind a very fine texture, which hinders the undamaged removal of the laminate from the mold. The layer of water-soluble PVA ensures proper separation between the laminate and the mold.

Using wet lay-up, four layers of 100 gram/m^2 glass fiber sheets were used to produce a 0.5 mm thick laminate, with alternating layers with a fiber direction 0/90 deg and ±45 deg. Following the wet lay-up, the laminate is covered with peel-ply, perforated release foil and bleeder material, after which the mold with laminate is put into a vacuum bag and cured in an oven. After curing the laminate was carefully separated from the mold using a brush and water. Afterwards, any remaining PVA film on the laminate is cleaned off.

The laminates are larger than the actual skin components and therefore need to be cut and trimmed to size. Patterns on the skins were traced out using the wooden frames as a guide. The individual parts, such as the bottom cover and control surface skins, were then cut out using a scalpel. Where necessary the parts were further adjusted with sanding paper. Any open edges on the laminate were filled up with cyanoacrylate glue to prevent delamination and sanded smooth.

As mentioned in section 4.2.1, the bottom part of the wing skin is removable to access the internals of the wing. The production of this cover requires additional steps in addition to the process detailed above. The skins act as the aerodynamic fairing of the wing section, hence extra care should be taken

to produce a smooth seem between the leading edge skin and the cover, as any discontinuities may trigger early flow separation. First, the cover itself was produced. Magnets are used to connect the bottom cover to the wing section. To accomplish this, a steel shim was laminated between the third and fourth layer of the laminate. Once cured, the cover trimmed and placed back into the mold and masked with tape and protective foil. The bottom leading edge was laid up, overlapping the bottom cover. After the first layer of fiberglass, the magnets were placed, lining up with the steel shim, followed by another three layers of fiber glass.

4.6.3. Final Assembly of the Wing Section

With the individual components completed, the model can be assembled. Before the skins can be glued in place, the soldered wiring harness is installed. First the top skin was glued to the skeleton using 30-minute epoxy, by placing the skin in the mold, placing the skeleton with epoxy onto the skin and weighing the combination down to prevent movement.

With structure of the wing fully assembled, the 3D-printed pushrod cover was glued to the bottom cover. Any gaps in the skin were filled with either a mix of ground glass fibers and epoxy or polyester putty. This was followed by multiple layers of spray putty and sanding to create a smooth surface, after which the wing section is coated with a matte black finish. The bearings were pushed in place, the servo actuators, freeplay mechanism, ADCs and BBBLue were installed and hooked up and the control surfaces were connected to their respective servo actuators. Finally, the mounting assemblies were installed, followed by the aerodynamic endplates. The assembled product can be seen in figs. 4.24 and 4.25.

Figure 4.24: *Side view of the wing section with the spoiler and aileron deflected. The right endplate is removed in this picture.*

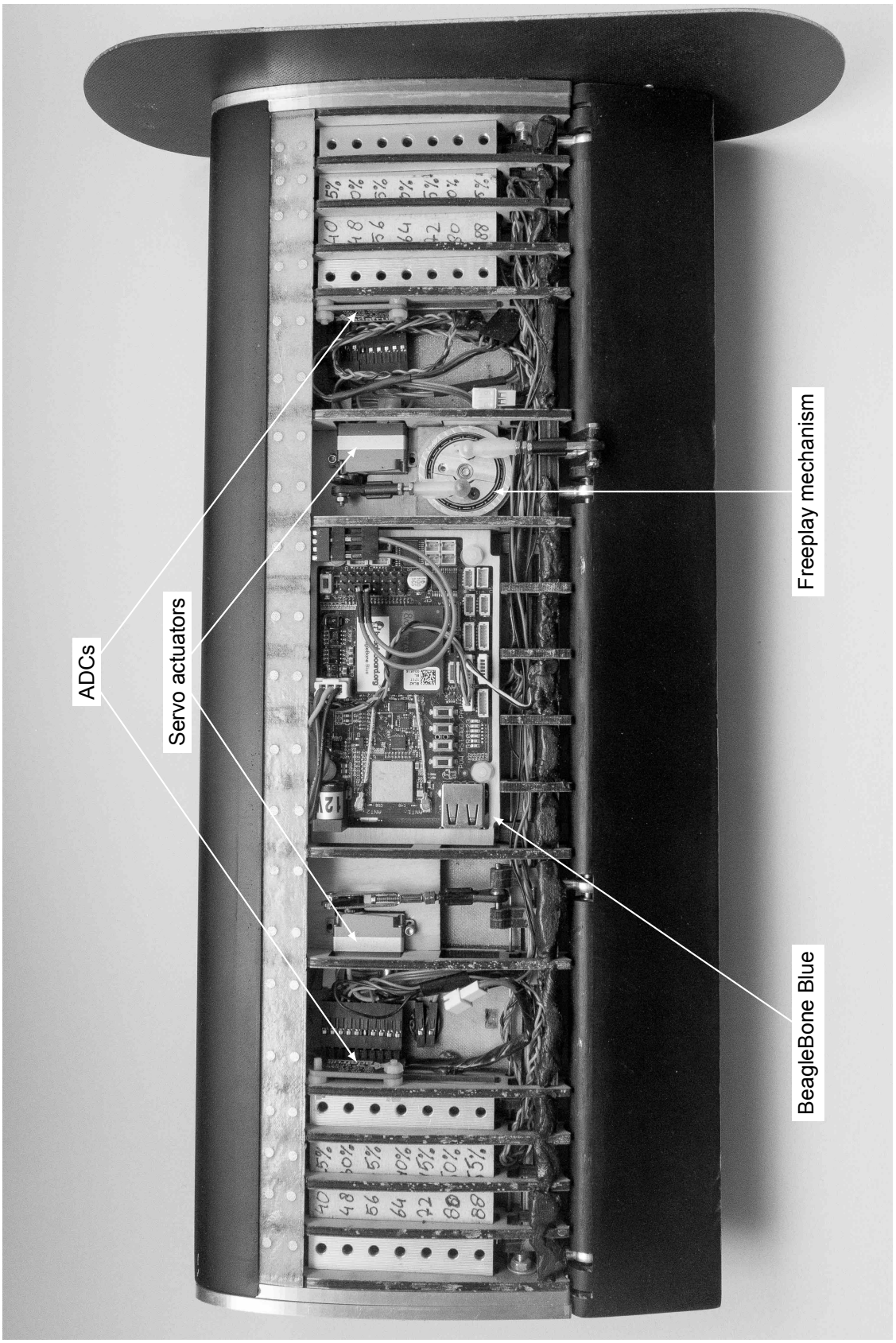

Figure 4.25: *Bottom view of the wing section with the cover and right endplate removed.*

5

Experimental Setup

In this chapter, all topics concerning the experimental setup will be discussed. This will start with the wind tunnel in section 5.1. Following the wind tunnel setup, the aeroelastic test apparatus (ATA) is shown in section 5.2. Finally, the test plan is laid out in section 5.3.

5.1. Wind Tunnel Setup

The wind tunnel tests were performed using the M-tunnel at the Low Speed Wind Tunnel Laboratory of Delft University of Technology. The M-tunnel has a 0.4 m by 0.4 m cross-section and is unique in the way that it can be operated as both an open-section or closed-section wind tunnel. The M-tunnel has a relatively low turbulence level, due to its large contraction ratio [65]. For the purpose of this investigation, the wind tunnel is run in the open-section configuration. In this configuration, the maximum attainable velocity is 35 m/s. An overview of the test setup is shown in fig. 5.1.

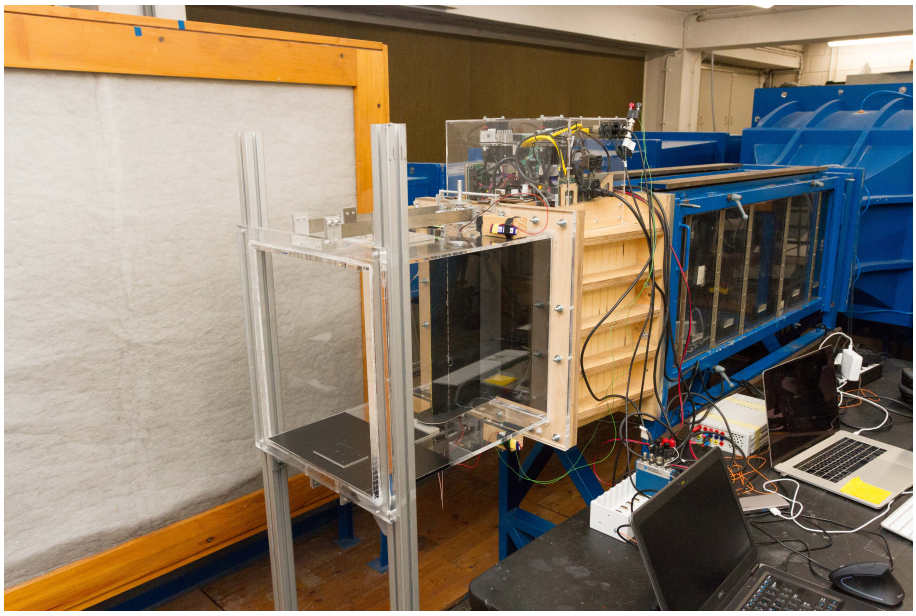

Figure 5.1: *Wind tunnel setup in the M-tunnel. From left to right are visible: the inlet filter, aeroelastic test apparatus, gust generator and wind tunnel itself.*

The M-tunnel by itself does have the capability to produce gusts. Therefore, to subject the wing section to gusts, an addition to the wind tunnel is necessary; the gust generator (GG). This miniaturized gust generator was specifically developed for the M- and W-tunnel by J.A. Geertsen [66].

The gust generator is mounted between the wind tunnel outlet and the inlet of the aeroelastic test apparatus. To account for the different widths of the wind tunnel and ATA, the gust generator has a contracting cross-section. A pair of gust vanes is mounted in this contraction. These vanes have a NACA0018 profile with a chord lenght of 80 mm. A schematic overview of the setup is given in fig. 5.2.

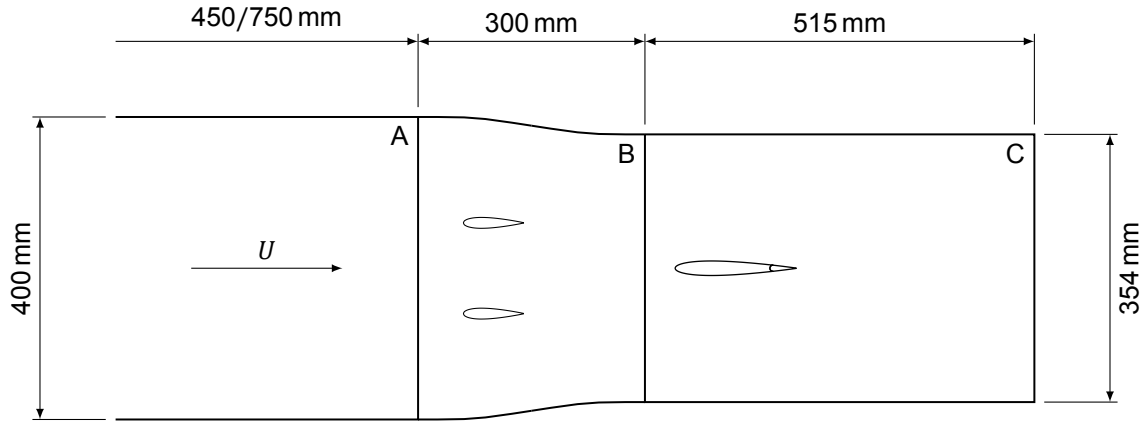

Figure 5.2: *Top view schematic of the wind tunnel (A), gust generator (B) and aeroelastic test apparatus (C). Adapted from Geertsen [66]*

The GG is controlled by a BeagleBone Green (BBG) single-board computer and is accessed as a server through the Secure Shell (SSH) protocol from the client computer. Commands to the GG, setting the gust type, amplitude, frequency, number of gusts and interval, are issued through a command-line interface on the client computer or through a shell script. The specifications of the gust generator can be found in table 5.1.

Table 5.1: *Gust generator specifications.*

Parameter	Value
Gust type	$\sin$, $1-\cos$
Amplitude	up to 15 deg
Frequency	up to 12 Hz

5.2. Aeroelastic Apparatus

The new wing section is designed to replace the current (passive) wing section in use with the aeroelastic apparatus (AA) developed by Gjerek et al [67]. As already shortly discussed in section 4.1, the AA is a device used to suspend the wing section in the wind tunnel. It consists of a rectangular, acrylic section that is mounted to the wind tunnel or gust generator and provides heave and pitch degrees of freedom. The AA is designed to closely resemble the typical section, a fundamental tool in aeroelasticity, enabling easy comparison of computational models with experimental data. By incorporating the new wing section with control surfaces and the FPM, the research capabilities using the AA are extended to include nonlinearities (control surface free play) and aeroservoelastic control.

The heave DoF is provided by two pairs of leaf springs mounted on the top and bottom of the AA. By changing the setting on the clamps of the leaf springs, the spring stiffness can be adjusted. An axle is mounted between the leaf springs on each side of the AA, where bearings ensure smooth movement. The torsional spring stiffness is provided by a pulley connecting to two coil springs. The torsional stiffness of the AA can be adjusted by both changing the diameter of the pulley, where an increase in diameter increases the torsional stiffness, and exchanging the coil springs. The top view of the AA is shown in fig. 5.3, a render of the suspension mechanism is seen in fig. 5.4.

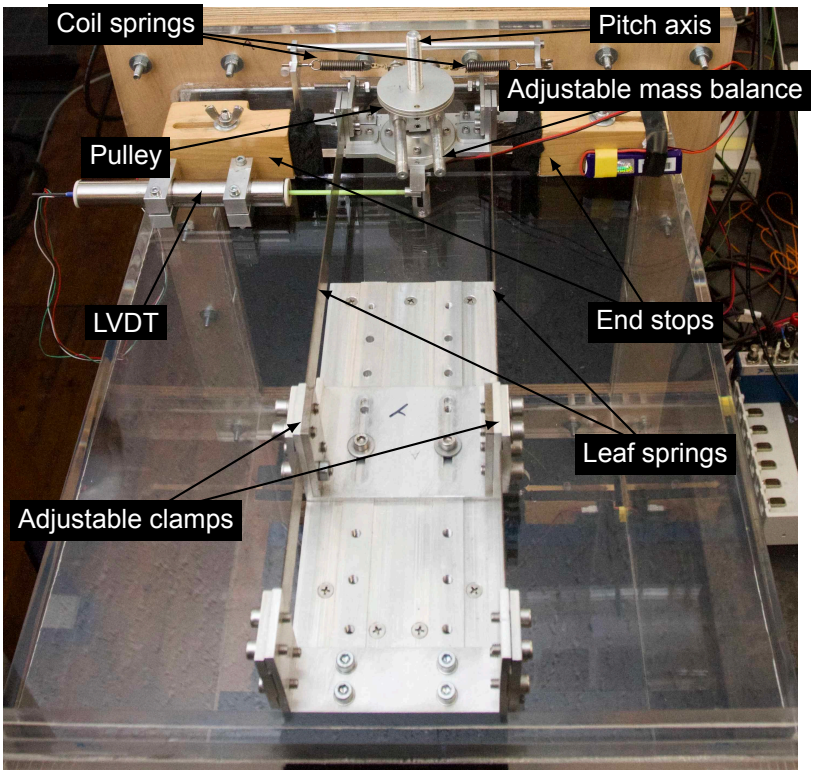

Figure 5.3: *Top view of the aeroelastic apparatus showing the heave and pitch mechanisms. N.B. the RVDT is connected to the pitch axis on bottom of the apparatus.*

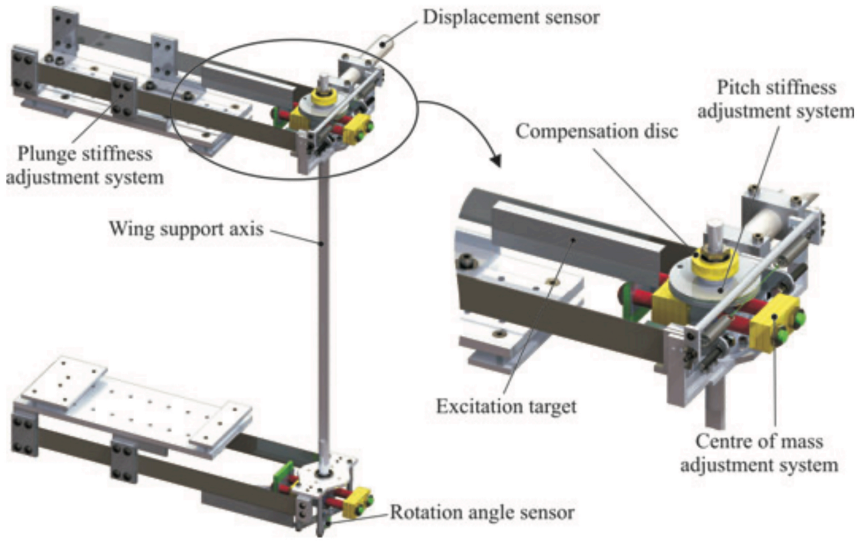

Figure 5.4: *CAD model of the pitch and heave (plunge) mechanism of the AA. Taken from Gjerek et al.[67].*

In addition to adjusting the heave and pitch stiffnesses, the combination of the AA and wing section allow for the adjustment of the pitch axis location, the center of mass and total mass and the moment of inertia of the wing. Due to the mounting assembly in the wing section, the pitch axis can be moved between 25% and 55% of the wing chord, affecting for example the divergence speed. The center of mass can be shifted forwards or backwards by the adding weights to the mass balance in front of or behind of the pitch axis, increasing or decreasing the flutter speed of the wing section.

5.3. Test Plan

The test plan describes all the tests that will be conducted in their respective order. The plan is divided into two major components. Section 5.3.1 deals with all the tests concerning system identification. In section 5.3.2, the tests for the GLA part of the investigation are laid out.

5.3.1. System Identification

System identification tests are performed to experimentally obtain the characteristics of a system. The system, in this case the wing section, is subjected to a known input, after which the response of the system is recorded. With the known input and measured output, a mathematical model of the system is obtained.

Ground Vibration Test

A ground vibration test (GVT) is performed to identify the dynamic properties of the structure. Using modal analysis, the modes shapes and their corresponding natural frequencies and damping ratios are determined. The identified frequencies will later be used to determine the parameters of the gusts used to excite the wing for the GLA part of the investigation, where large responses are expected when the wing section is excited at its natural frequencies, due to resonance.

The GVT is performed as an impact test with a roving hammer. The wing is tapped at eight different measurement points across the wing with an impact hammer. A pair of accelerometers placed on the wing, seen fig. 5.5, record the modal response of the wing section. The force and duration of the impact is recorded using a load cell in the impact hammer. The recorded impact and response data is then used to perform the modal analysis in Siemens Simcenter.

Wing Section Flutter Speed

Due to the potential destructive nature of flutter, the speed at which flutter occurs should be determined before proceeding with any of the wind tunnel experiments. At the flutter speed, coupling between the aerodynamic forces and the flexible structure produce a harmonic motion of increasing amplitude. To determine this speed, the parametric flutter margin method is utilized [68, 69]. With this method, a stabilizing mass is added to the system and the wing is excited over a range of flow velocities. At each velocity, the acceleration at the stabilizing mass is recorded using an accelerometer, which is then used to calculate the frequency response function.

Frequency response functions (FRFs) show the magnitude amplification and difference in phase of a system to an input over a range of frequencies. The known excitation and response signals are converted to the frequency domain, resulting in complex numbers called phasors, from which the magnitude $M(\omega)$ and phase $\phi(\omega)$ of the response can be determined using eqs. (5.1) and (5.2).

$$M(\omega) = 20 \log \left| \frac{M_o(\omega)}{M_i(\omega)} \right| \tag{5.1}$$

$$\phi(\omega) = \phi_o(\omega) - \phi_i(\omega) \tag{5.2}$$

The phase crossover frequency ω_{pco} is defined as the frequency at which the phase of the FRF is zero, eq. (5.3). With this frequency known, its corresponding magnitude and the flutter margin FM, defined by eq. (5.4), can be determined. The flutter margin indicates how the quantity of the stabilizing mass should be changed for flutter to occur, where $FM > 0$ dB indicates a stable system and $FM < 0$ dB indicates an unstable system. Therefore it can be concluded that flutter of the unmodified system occurs at $FM = 0$ dB. This procedure is performed for all tested flow velocities, after which the obtained flutter margin and phase crossover frequencies are plotted as a function of flow velocity. The flutter speed of the unmodified system is then found at the point where the resulting curve crossed 0 dB.

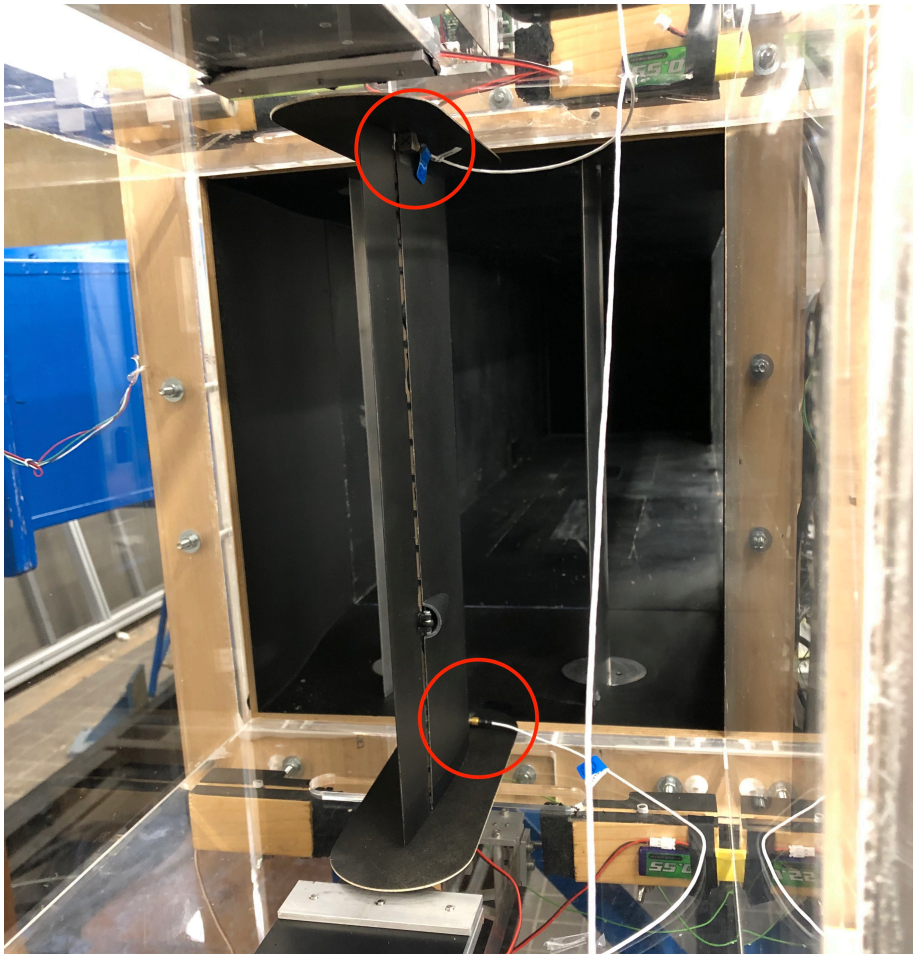

Figure 5.5: *Accelerometers (encircled in red) placed on the wing section in the wind tunnel.*

$$\phi(\omega_{pco}) = 0 \tag{5.3}$$

$$FM = -M(\omega_{pco}) \tag{5.4}$$

Actuator and Control Surface Frequency Response Functions

Previously frequency response functions were used to obtain the flutter speed of the wing section. For this part FRFs are used to both identify the dynamic behavior and create a mathematical model of the servo actuator and control surface actuation mechanisms.

To obtain the FRF for the servo actuator, a control signal of increasing frequency (chirp signal) is fed to the servo, oscillating the output shaft of the servo between ±45 deg, of which the position is recorded using the ADC. The input and output signals are converted to the frequency domain and the magnitude and phase are again determined using eqs. (5.1) and (5.2). The same procedure is repeated for the control surface actuation mechanisms, but with the control signal commanding oscillating aileron deflections between ±25 deg and spoiler deflections between 0 deg and 90 deg.

With the FRFs determined, they can be used to create a mathematical models. For future research, these mathematical models can be added aeroelastic models to correctly reflect the actuator dynamics. Depending on the form required for the aeroelastic model, the FRFs can be fitted to either transfer functions or state-space systems using a minimization algorithm (such as FMINCON), where the quantity minimized is the difference between the measured response and the simulated response of the estimated system.

Control Surface Aerodynamic Response
For the final part of the system identification, the aerodynamic response of the wing due to deflection of the control surfaces is determined. One at a time, the control surfaces are swept through a range of deflections at fixed increments. At each step, the control surface deflection is held constant and the resulting deflection and rotation are measured using the LVDT and RVDT respectively. With the bending and torsional stiffnesses known, the force and moment generated by the control surface deflection can be determined, according to eqs. (5.5) and (5.6). Then, with the flow velocity, air density and the geometrical parameters of the wing known, the lift and moment coefficients can be calculated using eqs. (5.7) and (5.8).

$$F = K_h h \tag{5.5}$$

$$M = K_\theta \theta \tag{5.6}$$

$$C_L = \frac{2F}{\rho U^2 bc} \tag{5.7}$$

$$C_M = \frac{2M}{\rho U^2 bc^2} \tag{5.8}$$

5.3.2. Gust Response

With all the system identification tests completed, the tests involving GLA are performed. First the open-loop gust response are determined and will serve as a baseline when comparing the closed-loop gust response.

Open-Loop
To determine the open-loop gust response of the wing, the control system is fed with zero-degree deflection commands for the entire duration of the run to keep the control surfaces is their undeployed position. The wing is subjected to ten gusts at and near with a gust frequency at or near the natural frequency of the first modes in bending and torsion identified during the ground vibration test. Using the recorded trigger signal of the gust generator, the test data can be averaged to a mean response over time, to assess the repeatability of the response.

Closed-Loop
For the closed-loop gust response, two different experiments are performed: 1) using only the aileron and 2) using only the spoiler. For each experiment, the wing is excited by a series of ten gusts. The gains of the PID controller have not yet been determined. Cassaro et al. [22] tuned the gains for their wing section with spoiler by trial and error, but indicate this was a lengthy process. To this end, a more structured approach was chosen:

1. The first test is run with propertional gain $K_p = 1$, integral gain $K_i = 0$, and differential gain $K_d = 0$.
2. Depending on the response of the system, the K_p is either increased if the system remains stable due to the control and the amplitude of the response is decreased, or K_p is decreased if the system is destabilized.
3. Based on the previous step, K_p is further increased or decreased until a gain value is reached where the amplitude of the response is no longer decreasing.
4. This process is repeated for the K_i and K_d, where the value of K_p is fixed at the value producing the minimum amplitude.

6

Results & Discussion

The results of the previously detailed test campaign will be shown and discussed in this chapter. The chapter is split in three parts; The validation of the spoiler aerodynamic model is treated in fig. 6.1. Section 6.2 deals with the experimental characterisation of the wing. In the final part, section 6.3 the open- and closed-loop gust responses of the wing are discussed.

6.1. Spoiler Aerodynamics Validation

In this section, the spoiler aerodynamic model from chapter 3 is validated. A comparison can only be made for the $C_L - \delta$ curve shown in fig. 3.9, as the angle of attack cannot be set accurately with the current test setup.

As mentioned in chapter 3, the aerodynamic model requires empirical input in the form of the cavitation number K or base pressure coefficient behind the spoiler. These values were not obtained during the wind tunnel tests, therefore the cavitation numbers given by Bernier [4] were already used for the verification of the spoiler model in chapter 3 and will be used as a basis. The values from Bernier are however for a non-symmetric Clark Y airfoil. Results using a NACA 0015 airfoil are given by Tam Doo [70], albeit only for a 0.097c spoiler at various chordwise locations.

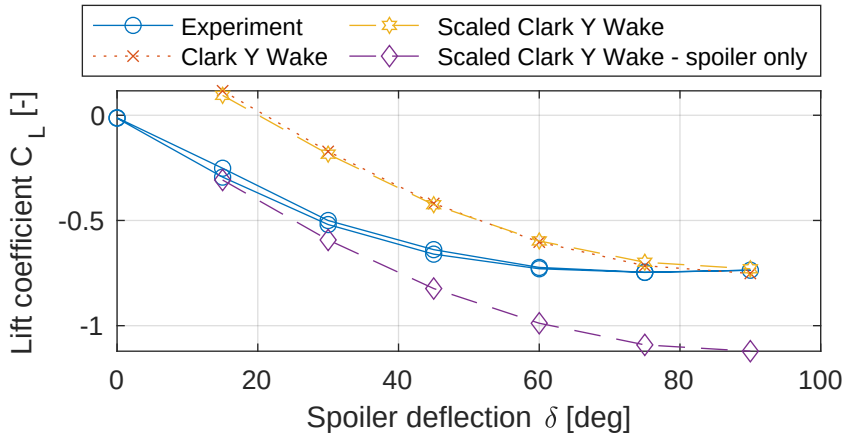

Figure 6.1: *Comparison of the experimental and computational $C_L - \delta$ curves at $\alpha = \beta = 0$ deg and Re=1.26E5.*

Figure 6.1 shows the experimentally obtained $C_L - \delta$ curve at $\alpha = \beta = 0$ deg. The test was performed

at $U = 12\,\text{m/s}$ and $\rho = 1.18\,\text{kg/m}^3$, given a chord-based Reynolds number of 1.26E5. The spoiler deflection was increased from 0 deg to 90 deg and back to 0 deg, in 15 deg increments. Some hysteresis is visible in the curve, but the amount is negligible. At $\delta = 0\,\text{deg}$, the experimental result $C_L = 0$, as is expected for a symmetric airfoil at $\alpha = 0\,\text{deg}$. $C_{L_{min}} = -0.74$ is obtained at $\delta = 75\,\text{deg}$. More observations regarding the control surface effectiveness will be given later in section 6.2.4.

For the computed $C_L - \delta$ curve, wake length is calculated using the base pressure coefficients of the Clark Y airfoil. These values are then scaled using the pressure coefficient of the NACA 0015 airfoil at $\delta = 90\,\text{deg}$. The $C_L - \delta$ curve is plotted in fig. 6.1 for both the original and scaled Clark Y data. Scaling of the wake with the NACA 0015 has negligible effect on the results. Due to the linearized model, this curve is a superposition of the spoiler and thickness contributions, the other components are zero (i.e. no camber, incidence or aileron deflection). The contribution of the spoiler itself is also plotted. For $\delta = 15\,\text{deg}$ and $\delta = 30\,\text{deg}$, the individual contribution of the spoiler agrees well with the experimental results. For $\delta = 90\,\text{deg}$ however, the total C_L shows close agreement.

The validation of the spoiler aerodynamic model remains inconclusive. Based on the current assumptions, the model has a difference up to $C_L = 0.35$ or 140 % with the experimental data. The assumption that the wing section of NACA 0014 airfoil has a similar wake length at the same spoiler deflections as a 14% Clark Y airfoil therefore seems invalid and further research is required.

6.2. System Identification

In this section the experimental results of the system identification are treated. The GVT results are treated first in section 6.2.1. This is followed by the parametric flutter margin in section 6.2.2. The frequency response functions, showing in section 6.2.3. Finally, section 6.2.4 shows the effectiveness of the control surfaces.

6.2.1. Ground Vibration Test

The results for the ground vibration test are given in table 6.1. For the purpose of this work, only the first three modes are considered, due to both limits on the gust generator and the control system of the wing section. The maximum attainable gust frequency with the gust generator is 12 Hz. The first identified mode is the first bending (heave) mode at 3.55 Hz. The second identified mode is the first torsional (pitch) mode at 6.39 Hz. The third and final mode is the asymmetric rocking mode at 11.10 Hz. These three modes are visualized in fig. 6.2.

Table 6.1: *Structural modes identified during the ground vibration test*

Mode		Frequency [Hz]	Damping coefficient [-]
1	Heave	3.55	0.072
2	Pitch	6.39	0.099
3	Rocking	11.10	0.037

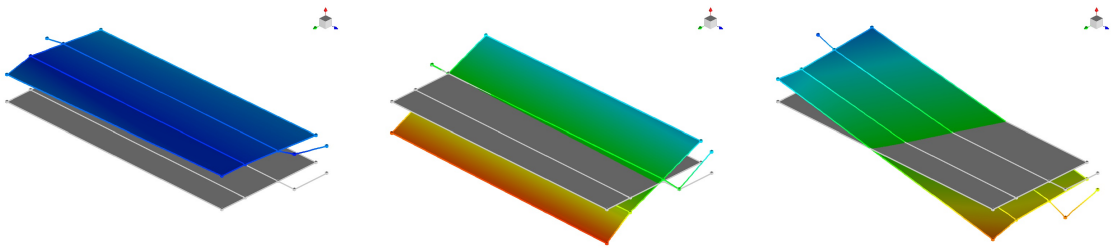

(a) *Heave.* **(b)** *Pitch.* **(c)** *Rocking.*

Figure 6.2: *The first three structural modes.*

Based on the obtained results, the gust frequencies could be determined. Five frequencies were chosen; below, at and above the frequencies of the first two modes. This means the gust frequencies at the structural modes are chosen as close as possible to the modal frequency, as the minimum step size

in gust frequency is limited to 0.5 Hz by the gust generator. This gives the following gust frequencies: 2.0 Hz, 3.5 Hz, 5.0 Hz, 6.5 Hz and 7.0 Hz. It is expected that the wing section shows an amplified response when excited at (or close to) the frequencies of the structural modes, i.e. an amplified response in heave for a 3.5 Hz gust and an amplified response in pitch for a 6.5 Hz gust.

6.2.2. Parametric Flutter Margin

Next are the result of the flutter tests. The frequency response functions were obtained for flow velocities ranging from 5 m/s to 14 m/s. The obtained phase crossover frequencies and their corresponding flutter margins are plotted in figs. 6.3a and 6.3b. Flutter occurs when the flutter margin curve in fig. 6.3a crosses the horizontal axis at 0 dB, giving a flutter speed $v_f = 12.8$ m/s. The flutter frequency is determined by taking the intersection of the flutter velocity and the frequency curve in fig. 6.3b, resulting in a flutter frequency $\omega_f = 3.95$ Hz. For the remainder of the experiment the wind tunnel velocity will be set to 12 m/s.

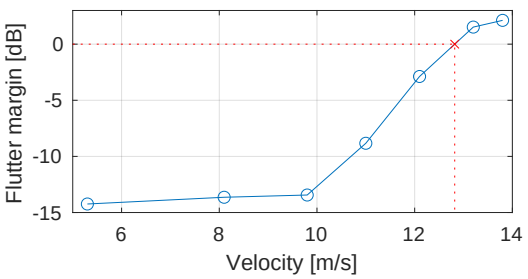

(a) *Flutter margin versus velocity. Flutter happens when the flutter margin switches sign from negative to positive at* 12.82 m/s.

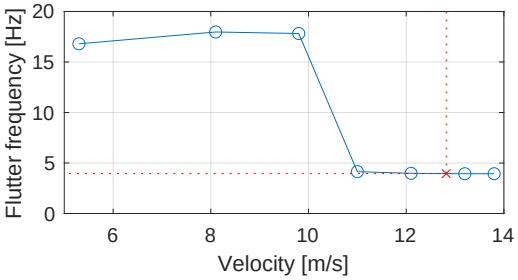

(b) *Flutter frequency versus velocity. At the flutter boundary of* 12.82 m/s, *the wing section flutters with a frequency of* 3.95 Hz.

Figure 6.3: *Parametric flutter margin results.*

6.2.3. Actuator and Control Surface Frequency Response Functions

First, the dynamic response of the servo actuator itself is discussed, together with the mathematical models obtained to describe this behavior. This is followed by the dynamic response of the control surface actuation mechanisms.

Servo Actuator Frequency Response Function

To obtain the frequency response function of the BMS-A10V servo actuator, it was subjected to a chirp signal of frequencies ranging from 0.1 Hz to 10 Hz. To show the effect of the oscillation amplitude on the response of the servo actuator, this experiment was performed for amplitudes of 15 deg and 45 deg. The output of the servo was measured across its internal potentiometer, which is accordingly scaled thereafter to reflect the output angle. The input and output signals for the 15 deg and 45 deg oscillations are plotted in figs. 6.4 and 6.5 respectively.

Comparing these figures, it becomes clear that the usable bandwidth of the servo is larger for oscillations of smaller amplitude, as can be expected. For both oscillations the amplitude of the response starts decaying between 20 s and 25 s, but the response of the 15 deg oscillation still reaches approximately 80% of the commanded deflection at 10 Hz. For the 45 deg oscillation, the response is only able to reach 30% of the commanded deflection at 10 Hz.

The time domain data is converted to the frequency domain and shown in the Bode plot in fig. 6.6. The magnitude plot shows little degradation in amplitude frequency response for both responses up to 3 Hz. The frequency of the chirp signal as a function of time is given by eq. (6.1), where f_0 and f_1 are the initial and final frequency of the signal and T is the signal length. Using this equation, it is found that the 3 Hz frequency corresponds to the time where the time domain responses start to lag. Finally, converting magnitude values of -2 dB and -10 dB at 10 Hz show these values are the percentages of commanded response of 80 % and 30 % respectively, found in the previous paragraph. The phase frequency response again shows similar performance for both 15 deg and 45 deg up to 3 Hz, with the lag already present at low frequencies, increasing to -25 deg at 3 Hz. Beyond 3 Hz, the phase frequency response is similar to the magnitude frequency response, with the 45 deg oscillation lagging

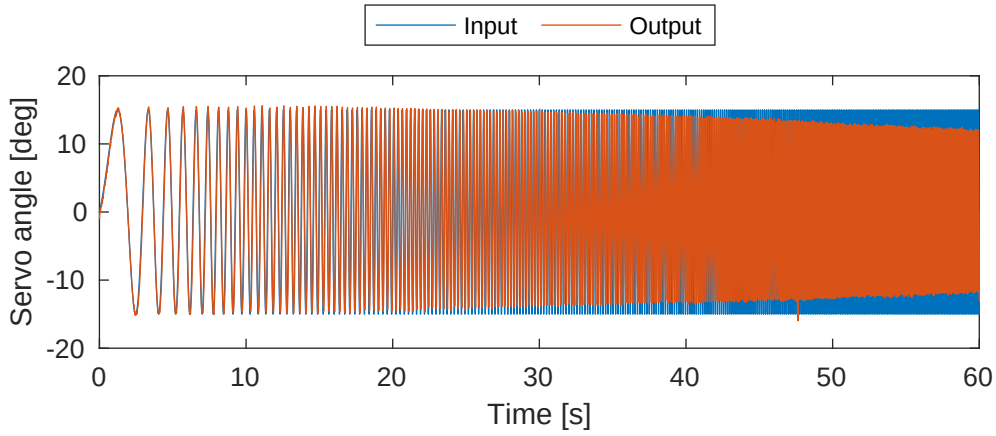

Figure 6.4: *Servo input and output as a function of time for a* 15 deg *amplitude oscillation.*

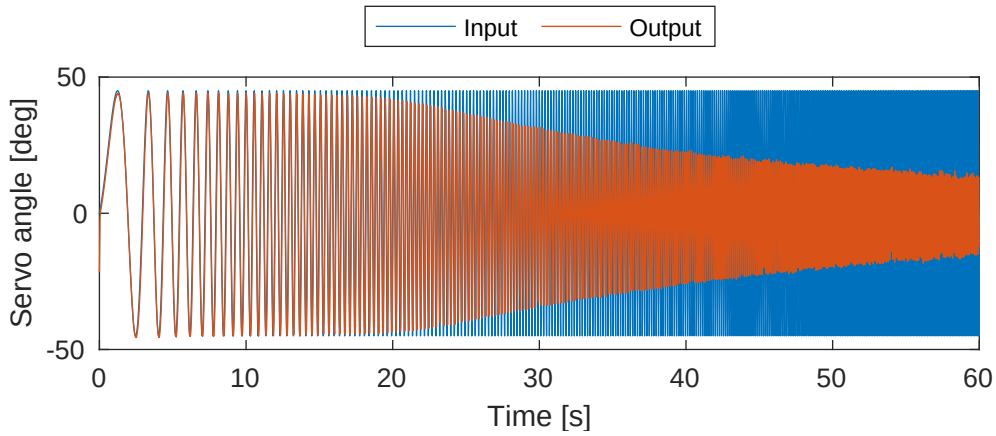

Figure 6.5: *Servo input and output as a function of time for a* 45 deg *amplitude oscillation.*

up to −105 deg at 10 Hz. For the 15 deg oscillation, the response is still lagging, but only reaching a phase difference of −70 deg at 10 Hz.

$$f(t) = ct + f_0, \text{ with } c = \frac{f_1 - f_0}{T} \tag{6.1}$$

$$\begin{aligned} \dot{x} &= \begin{bmatrix} 0 & 1 \\ a_{21} & a_{22} \end{bmatrix} x + \begin{bmatrix} 0 \\ b_2 \end{bmatrix} u \\ y &= \begin{bmatrix} 1 & 0 \end{bmatrix} + 0u \end{aligned} \tag{6.2}$$

The data is converted to the frequency domain and then fitted with a second order state space system given by eq. (6.2), with $x = [\beta\ \dot{\beta}]^{\mathrm{T}}$ and $u = \beta_{ref}$, where β, $\dot{\beta}$ and $\ddot{\beta}$ are the servo output angle and its time derivatives and β_{ref} is the servo input signal. The data is fitted to this specific form of system such that it can be incorporated into the state-space system of a 3-DoF typical section, such as presented by Dimitriadis [71]. The coefficients of the estimated state-space systems are given in table 6.2.

Table 6.2: *Coefficients of the estimated state-space systems.*

Amplitude [deg]	$a21$	$a22$	$b2$
15	-8.387	10	-0.6268
45	-1.214	2.221	-7.559E-3

Bode plots of the estimated systems are compared to the measured data in figs. 6.7 and 6.8. For

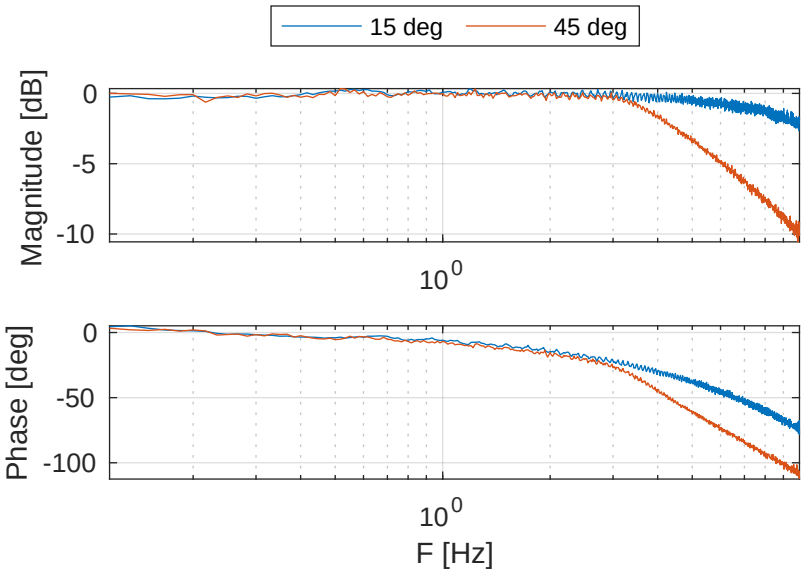

Figure 6.6: *Bode plot of the servo actuator response.*

the 15 deg oscillation, both magnitude and frequency responses of the estimated system follow the experimental data closely. For the 45 deg oscillation this is however not the case. The distinct cutoff frequency around 3 Hz is not clearly visible in the magnitude nor in the phase response, with both responses instead showing a more gradual increase in lag.

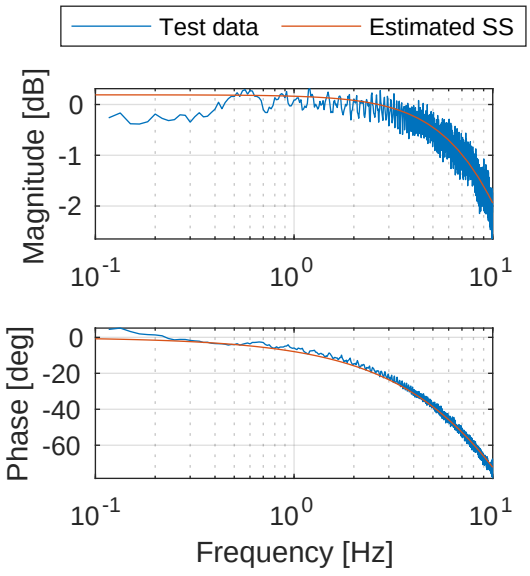

Figure 6.7: *Bode plot comparison of the estimated system and experimental data for* 15 deg.

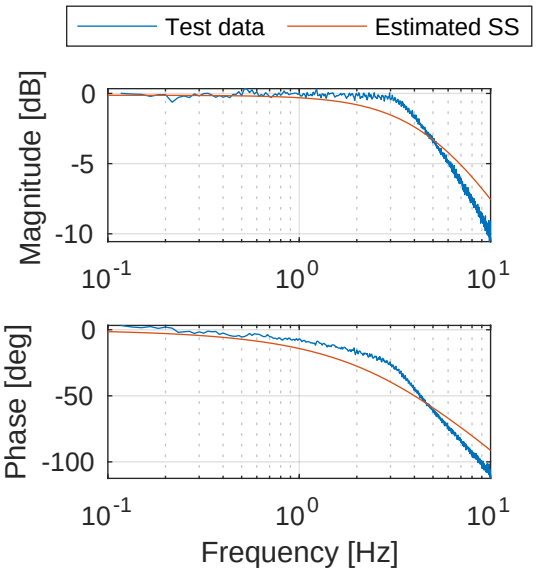

Figure 6.8: *Bode plot comparison of the estimated system and experimental data for* 45 deg.

Control Surface Frequency Response Functions

The process detailed in the previous paragraphs is now repeated to determine the frequency response of the aileron and spoiler control surfaces at the test conditions, $U = 12\,\mathrm{m/s}$. The servomotors are now connected to their respective control surface actuation mechanisms and are again controlled with a chirp signal, its frequency ranging from 0.1 Hz to 8 Hz. It should be noted here that the control surface

deflection angles are not measured directly at their hinges, but at the servo. The actuation mechanisms are assumed to be rigid and do not contain any free play.

The time response of the aileron is seen in fig. 6.9, that of the spoiler in fig. 6.10. The commanded deflection of the aileron is between -25 deg and 25 deg, for the spoiler this is between 0 deg and 90 deg. A clear distinction is visible between the aileron and spoiler. After about 20 s, the amplitude of the aileron output starts to decrease, attaining only about 50% of the commanded amplitude at the end of the run. The spoiler on the other hand performs better for the entire duration, even though it has a maximum deflection almost double to that of the aileron. This can be explained when looking back at figs. 4.4 and 4.8. The structure of the aileron has a mass that is four times higher than that of the spoiler. In addition, the mass moment of inertia of the aileron structure alone is an order of magnitude larger compared to the spoiler. The inertia of the aileron actuation mechanism is further increased by the moving masses of the freeplay mechanism, compared to direct, lightweight pushrod connection for the spoiler actuation mechanism. Another important factor in the differences between these responses is the ratio between control surface deflection and actual servo deflection, shown in figs. 4.7 and 4.9. The spoiler deflects approximately 1.5 deg per deg of servo actuator deflection, whereas the aileron deflects approximately 0.5 deg per degree of aileron deflection. To increase this ratio, enabling a faster aileron response, the distance between the output shaft of the servo actuator and pushrod connecting the servo horn to the FPM can be increased. Increasing this distance however comes with the disadvantage of decreasing the rigidity of the actuation mechanism due to the larger forces exerted on the plastic servo horn.

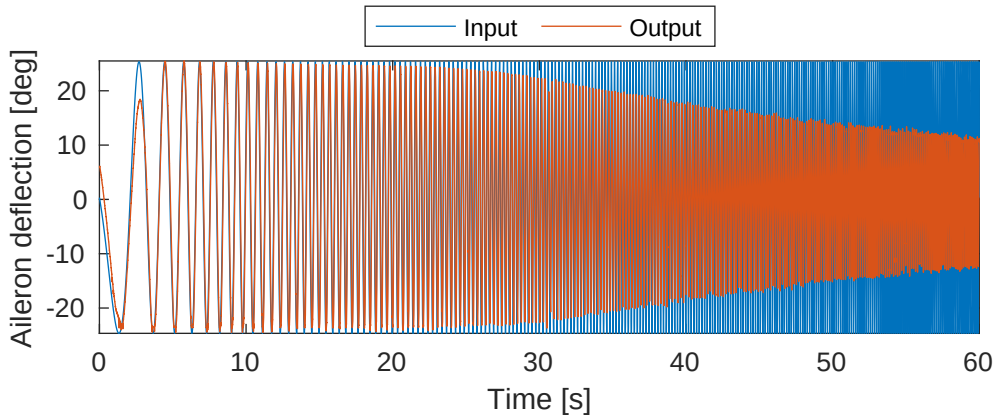

Figure 6.9: *Aileron commanded deflection and actual deflection as a function of time.*

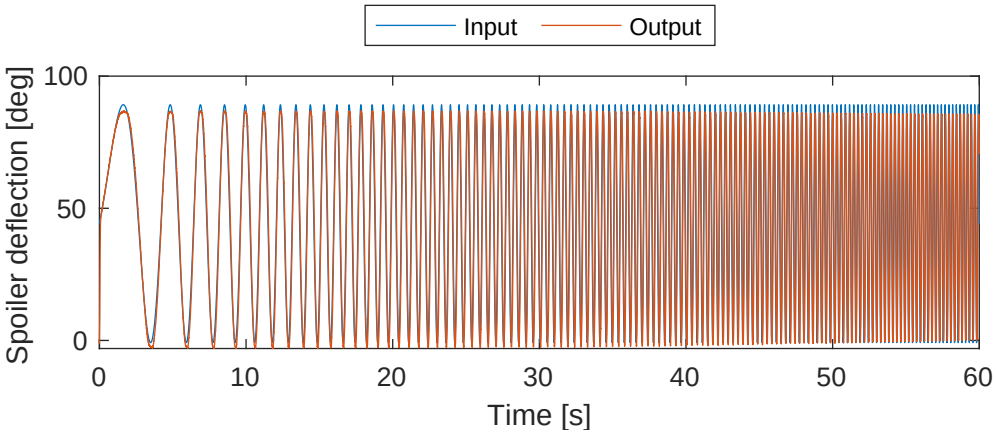

Figure 6.10: *Spoiler commanded deflection and actual deflection as a function of time.*

The frequency response of both are compared in fig. 6.11. Here too the difference is visible between

the aileron and spoiler. The magnitude frequency response of both remains steady at 0 dB up to 4 Hz. The aileron has a cutoff frequency of 6.65 Hz. For the spoiler response, the response becomes noisy after 4 Hz. Upon further inspection of the data, it was found that the final frequency of the chirp signal had been set to 4 Hz, therefore nothing conclusive can be said the higher frequencies of the spoiler. Similarly the aileron magnitude response shows noise for frequencies larger than that of the chirp signal, in that case 8 Hz. The phase frequency response shows multiple large peaks. These peaks have a value approximately 360 deg higher than their neighboring values, meaning that these values are simply anomalies due to the data processing. Both spoiler and aileron responses show a gradual decrease in phase angle, indicating lag. The spoiler frequency response again turns noisy after 4 Hz, but has a phase angle of approximately -30 deg at that frequency. The lag of the aileron is 15 deg larger, being -45 deg at 4 Hz. The phase angle of the aileron is approximately -100 deg at 8 Hz.

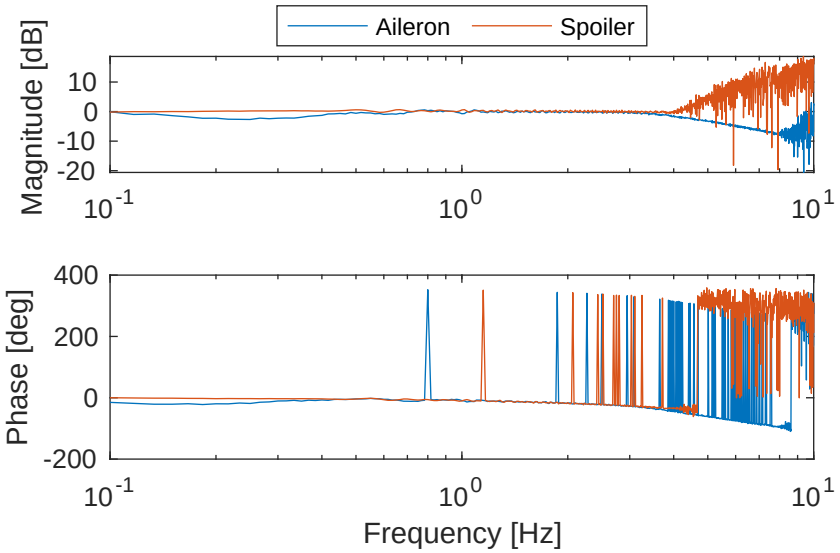

Figure 6.11: *Bode plot comparison of the aileron and spoiler response to a chirp input signal.*

6.2.4. Control Surface Aerodynamic Response

The results for the control surface aerodynamic response are presented in this section. The effectiveness of the control surfaces is defined as the slope of their respective lift curves, that is the change in lift coefficient per degree of change in control surface deflection, $\Delta C_L/\Delta *$, where $*$ denoted the aileron or spoiler. Figure 6.12 shows the $C_L - \beta$ curves at $\alpha = 0$ deg for spoiler deflections ranging from 0 deg to 90 deg in 15 deg increments. The curve for $\delta = 0$ deg is as expected, showing a linear trend.

The curve for $\delta = 15$ deg already shows a decrease in aileron effectiveness for approximately -10 deg $\leq \beta \leq 0$ deg. The next curve, $\delta = 30$ deg, shows a negative slope for -20 deg $\leq \beta \leq -10$ deg. This phenomenon, where the aerodynamic response is reversed for a certain control surface deflection, is called aerodynamic reversal. Loss of control surface effectiveness, where a change in deflection does not result in a change of lift ($\Delta C_L/\Delta\beta = 0$), occurs between 15 deg $\leq \delta \leq$ 30 deg. The decrease, loss and reversal of aileron effectiveness is a result of the interaction of the aileron with the turbulent wake created by the spoiler.

The curves for $\delta \geq 30$ deg all show a similar trend, showing control reversal for -20 deg $\leq \beta \leq -10$ deg and a linear trend - similar to the $\delta = 0$ deg curve - for $\beta \geq -5$ deg. Interestingly, spoiler deflections of $\delta \geq 60$ deg are all not only similar in trend, but the difference in magnitude is negligible. This can be attributed to the fact that the influence of the spoiler is linked the vertical height of the spoiler, or projection height. The spoiler projection height does not change significantly beyond spoiler deflections of 60 deg, due to the kinematics of the spoiler deployment.

Figure 6.13 shows the $C_L - \delta$ curve at $\alpha = \beta = 0$ deg. A linear trend is visible for 0 deg $\leq \delta \leq$ 30 deg, after which the spoiler response is highly nonlinear. Similar to fig. 6.12, the curve shows little difference in C_L for $\delta \geq 60$ deg. The minimum and maximum lift coefficients and corresponding control surface

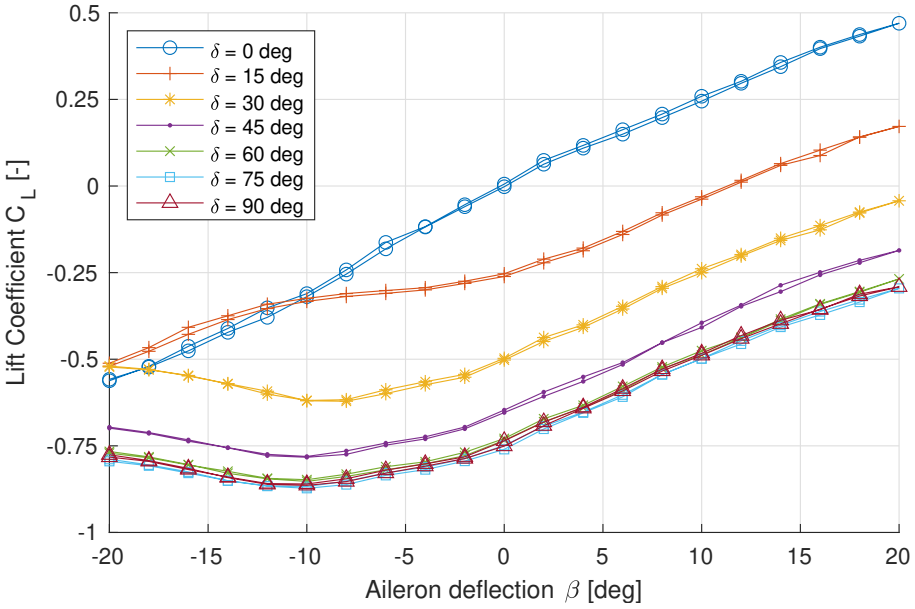

Figure 6.12: *Lift coefficient versus aileron deflection angles for different spoiler deflection angles at α = 0 deg, Re=1.26E5.*

deflections are summarized in table 6.3. This table indeed shows that the minimal lift coefficient values as a function of aileron deflection are obtained at $\beta = -10$ deg, and are within ±1.5% of each other, a negligible difference. As such, limiting the maximum spoiler deflection to 60 deg to increase the response time is justified.

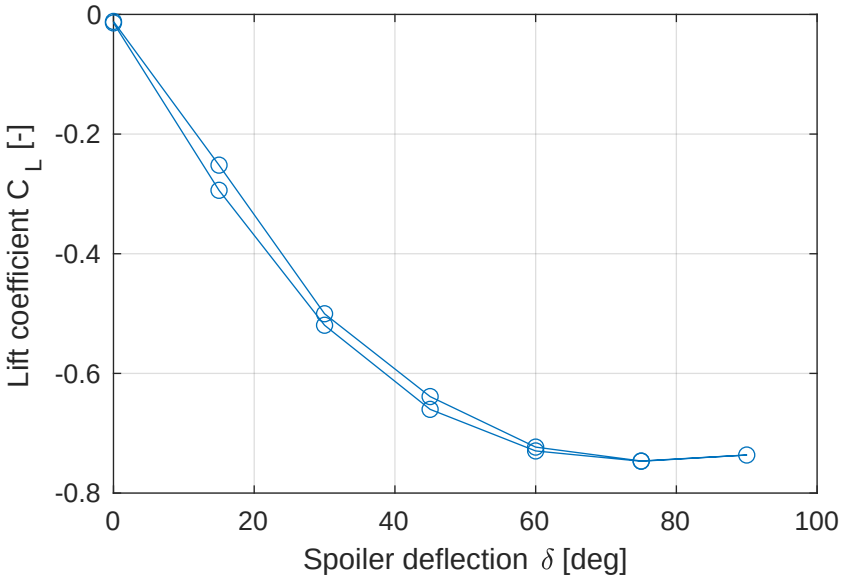

Figure 6.13: *Lift coefficient versus spoiler deflection at $\alpha = \beta$ = 0 deg, Re=1.26E5.*

Comparing the linear parts of the lift curves in figs. 6.12 and 6.13, it is clear that the aileron has the greater control surface effectiveness of the two. As will become clear in the next section, this does not necessarily mean it will provide better aerodynamic control. While the aileron has greater effectiveness, its deflection is limited to ±20 deg, thus generating a $\Delta C_{L_{\max}} \approx \pm 0.5$. The spoiler on the other hand has a lower control surface effectiveness, but its maximum deflection angle allows for a $\Delta C_{L_{\max}} \approx -0.75$. As the sign indicates however, the spoiler is only useful to decrease lift, whereas the aileron can be used to both increase and decrease lift.

Table 6.3: *Comparison of control surface effectiveness of the aileron and spoiler.*

Aileron	δ [deg]	$C_{L_{\min}}$ [-]	$\beta_{\min}$ [deg]	$C_{L_{\max}}$ [-]	$\beta_{\max}$ [deg]
	0	-0.56	-20	0.47	20
	15	-0.52	-20	0.17	20
	30	-0.62	-8	-0.04	20
	45	-0.78	-10	-0.19	20
	60	-0.85	-10	-0.27	20
	75	-0.87	-10	-0.30	20
	90	-0.86	-10	-0.29	20
Spoiler	β [deg]	$C_{L_{\min}}$ [-]	$\delta_{\min}$ [deg]	$C_{L_{\max}}$ [-]	$\delta_{\max}$
	0	-0.75	75	-0.01	0

6.3. Gust Load Alleviation using Aileron and Spoiler with PID Control

In this final section of the results, the open- and closed-loop gust responses will be treated. As mentioned in section 6.2.1, the wing will be subjected to gusts of 2 Hz, 3.5 Hz, 5 Hz, 6.5 Hz and 7 Hz to see how the wing behaves when excited near and at (as close as possible) its heave and pitch mode. A graphic representation of $1 - \cos$ profiles that the wing will be subjected to versus time and distance is plotted in fig. 6.14. As can be seen, the slowest gust (2 Hz) has a gust length of 6 m and takes 0.5 s to pass. The fastest gust (7 Hz) takes 0.14 s to pass and has a gust length of 1.71 m. The reduced frequency k, a measure of the unsteadiness of the flow (eq. (6.3)), ranges from 0.08, indicating quasi-steady flow, to 0.29, indicating highly unsteady flow.

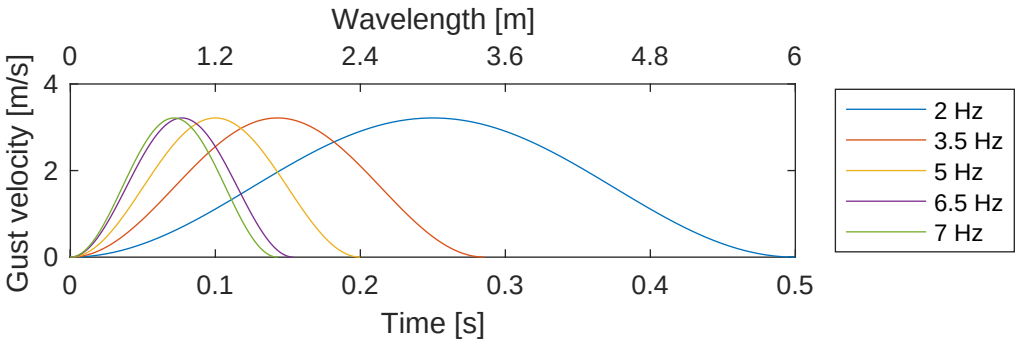

Figure 6.14: *Gust profiles for gust frequencies of* 2 Hz, 3.5 Hz, 5 Hz, 6.5 Hz *and* 7 Hz *at* $U = 12$ m/s.

$$k = \frac{\omega b}{U} = \frac{\pi f c}{U} \tag{6.3}$$

For each combination of gust frequency and gain value, ten runs were recorded. Important characteristics for the gust response are the maximum amplitude and damping coefficient. To show statistical significance, the mean and standard deviation of the time response were calculated. The maximum amplitude was determined by finding the maximum of the absolute value of the gust response, i.e. $A_{\max} = \max|h|$. The damping coefficient was calculated using the logarithmic decrement δ, defined by eq. (6.4), where $h(t_1)$ and $h(t_2)$ are values of two peaks spaced one period from each other, that is $t_2 = t_1 + T$, where T is the period. A graphic representation of this method is shown in fig. 6.15.

The damping ratio ranges from $\zeta = 0$ for an undamped system, $0 < \zeta < 1$ for an underdamped system, $\zeta = 1$ for a critically damped system and $\zeta > 1$ indicating an overdamped system and is calculated using eq. (6.5).

$$\delta = \ln \frac{h(t_1)}{h(t_2)} \tag{6.4}$$

$$\zeta = \frac{\delta}{\sqrt{\delta^2 + (2\pi)^2}} \tag{6.5}$$

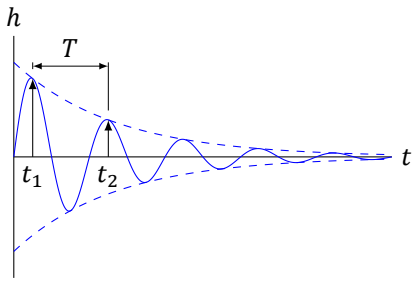

Figure 6.15: *Points used to calculate the logarithmic decrement.*

All graphs on the next several pages show the mean data taken over all the runs for the same conditions. As mentioned before, both the mean and standard deviation of the response are calculated at each time step, where a lower standard deviation indicates a more repeatable response. In the graphs containing the time responses, the standard deviation is shown as a shaded band around the mean line. For the plots comparing the amplitude and damping, error bars are used to indicate the standard deviation.

One final note regarding the results; even though both the heave and pitch DoFs were recorded, only the results for the heave DoF will be shown and discussed. The pitch data is deemed unusable due to a presumed faulty calibration and high noise on the signal. The source of the faulty calibration is assumed to be a wrong factor scaling the sensor voltage to deflection. The high noise on the signal was determined to originate from the motor driving the wind tunnel fan, transmitted to the sensors over the power grid. This noise is also present in the heave data, but could be filtered out relatively well. For the pitch data however, the noise was an order of magnitude larger than the measured deflection.

6.3.1. Open-Loop Gust Response

The open-loop gust response results are shown in figs. 6.16 to 6.18. The responses all show the behavior of a damped harmonic signal, indicating the open-loop system is stable. As seen in fig. 6.18, the open-loop response is greatly underdamped, with the damping coefficient close to zero, the undamped case. As the gust wavelength is at least ten times larger than the wing of the chord, the wing experiences a nearly constant gust velocity along its entire chord. Due to this nearly constant gust velocity, the first half period of the transient response closely follows the shape of the gust profiles shown in fig. 6.14, indicating the response is driven by the gust excitation. Following this initial response, the remainder of the response oscillates with a frequency of approximately 3.5 Hz, showing this part of the response is driven by the heave mode.

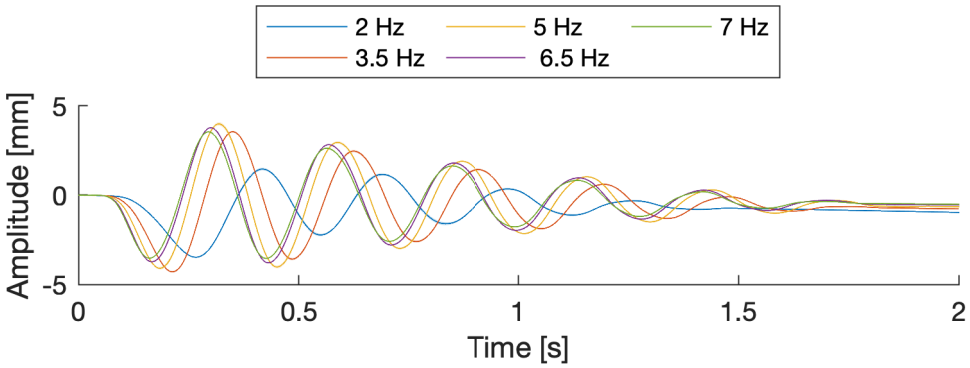

Figure 6.16: *The open loop displacement response for increasing gust frequencies.*

The influence of the gust excitation dies out within the first period, after which the system starts oscillating with a frequency around 3.5 Hz, identified earlier as the first mode in heave of the wing. Expectedly, the largest amplitude can also be found near the heave mode, with a gust excitation of 3.5 Hz as seen infig. 6.17. The 2 Hz gust gives the response with both the smallest amplitude and damping. Figure 6.18 shows that the open-loop response for 5 Hz is the least damped, also visible in fig. 6.16, showing the largest secondary peak.

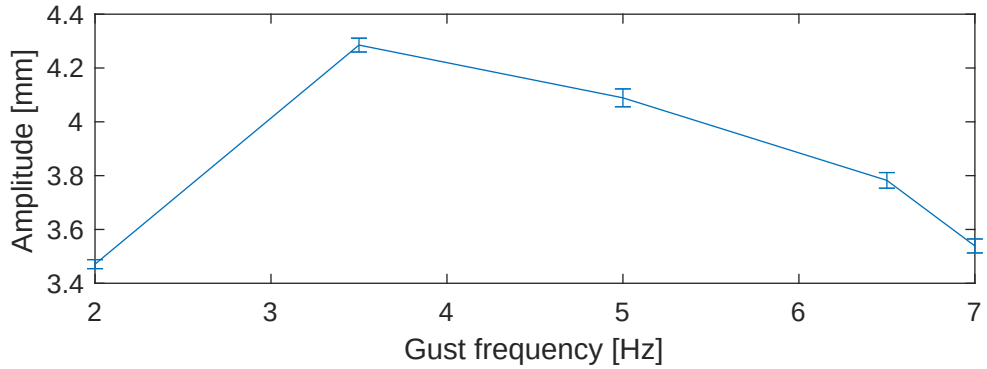

Figure 6.17: *Maximum amplitude comparison of the open-loop response.*

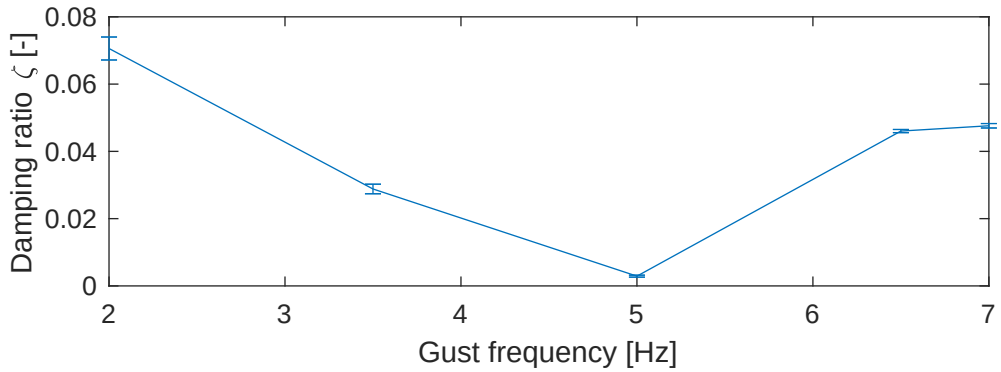

Figure 6.18: *Damping ratio comparison of the open-loop response.*

In addition to the time domain analysis, the data was analyzed in the frequency domain, to gain insight in the dominant frequency components of the open-loop response. The power spectral density plots for the open-loop responses are shown in fig. 6.19. Indicated in these plots are the both the peaks in the spectrum as by the dotted lines, as well as the gust excitation frequency by the dashed lines.

All open-loop responses show peaks near frequencies of 3.5 Hz and 11 Hz, respectively corresponding to the bending and rocking modes of the wing section. The largest peak is seen at 3.5 Hz for all gust frequencies, indicating the transient response is dominated by the bending mode. As expected, the peak of the 3.5 Hz gust coincides with the frequency of the bending mode, however a peak around frequency of the torsional mode is missing, indicating weak coupling between the heave and pitch modes. This peak is expected to be found in the PSDs of the pitch response. Distinct peaks at the other gust frequencies are clearly missing. This may be explained by the earlier mentioned fact that the wavelength of the gust is at least 10 times larger than the wing chord, subjecting the wing to a nearly constant gust velocity along its chord. If the wavelength of the gust were to be smaller (thus a higher frequency gust) than the wing chord, it is more likely that a peak would show up at that gust frequency in the frequency spectrum.

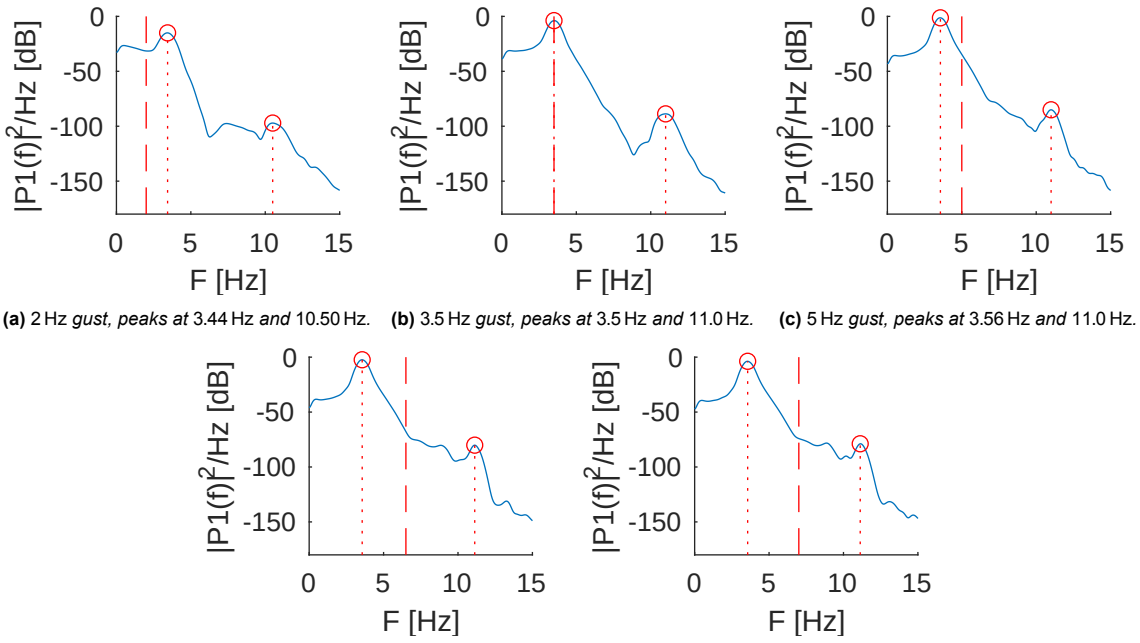

(a) 2 Hz *gust, peaks at* 3.44 Hz *and* 10.50 Hz. **(b)** 3.5 Hz *gust, peaks at* 3.5 Hz *and* 11.0 Hz. **(c)** 5 Hz *gust, peaks at* 3.56 Hz *and* 11.0 Hz.

(d) 6.5 Hz *gust, peaks at* 3.56 Hz *and* 11.13 Hz. **(e)** 7 Hz *gust, peaks at* 3.56 Hz *and* 11.13 Hz.

Figure 6.19: *Power spectral densities. The gust frequencies are indicated by the dashed red line in each plot, peaks are indicated by the red dotted lines.*

6.3.2. Closed-Loop Gust Response

The next several pages will show the results of the closed-loop gust response. A total of four different cases will be compared; proportional control using aileron versus spoiler, for gust frequencies of 3.5 Hz and 6.5 Hz. These gust frequencies were chosen as they are close to the heave and pitch modes of the wing. Furthermore, since the wing is controlled using the acceleration in heave direction, the differential gain of the PID controller, K_D is set to zero. If this gain were to be set at a non-zero value, this would mean part of the response is controlled by a fourth-order derivative of the displacement, likely resulting in a quickly saturating control signal. Results with proportional-integral control were also obtained, however the results were discarded due to a bias in the accelerometer, resulting in non-zero steady state displacement.

Aileron - Proportional Control

Figures 6.20 and 6.21 show the comparisons of mean closed-loop response for GLA with proportional aileron control with the open-loop response at gust frequencies of 3.5 Hz and 6.5 Hz. As can be seen in these figures, the effect of the implemented control is limited, giving only a 10% reduction in amplitude for $F_g = 3.5$ Hz, for $F_g = 6.5$ Hz a reduction in amplitude of 15% is achieved, also shown in the comparison in fig. 6.22. Looking at fig. 6.23, the closed-loop damping increases up to 145% for $F_g = 3.5$ Hz. At $F_g = 6.5$ Hz however, the damping is worse compared to the open-loop. This means that while the amplitude may be decreased by the use of the aileron, the movement of the aileron can also be considered as an additional harmonic excitation of the system. It adds additional energy to the system, reducing the damping and therefore prolonging the oscillations.

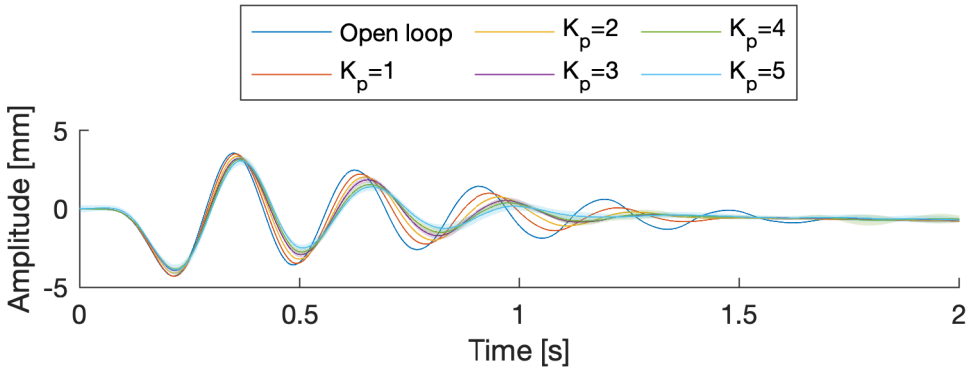

Figure 6.20: *Mean closed-loop aileron response with P control, gust frequency 3.5 Hz.*

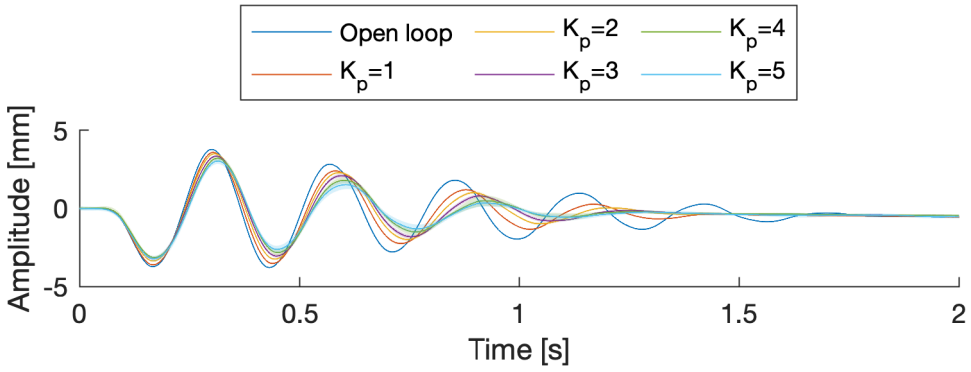

Figure 6.21: *Mean closed-loop aileron response with P control, gust frequency 6.5 Hz.*

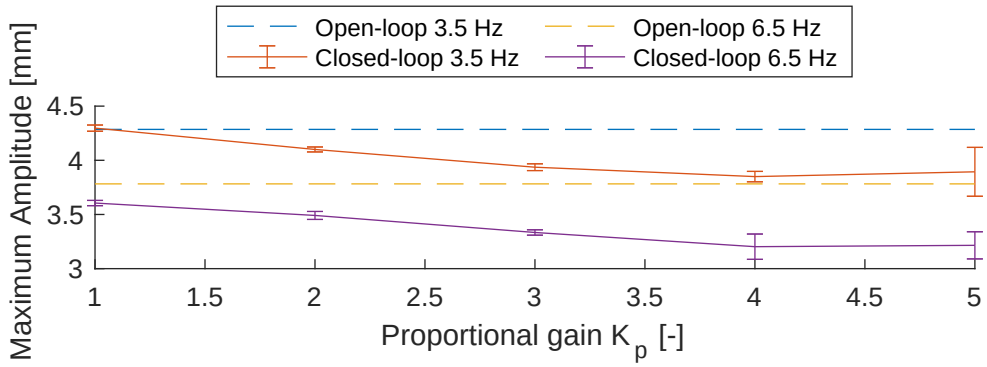

Figure 6.22: *Maximum amplitude comparison for the aileron response with P control.*

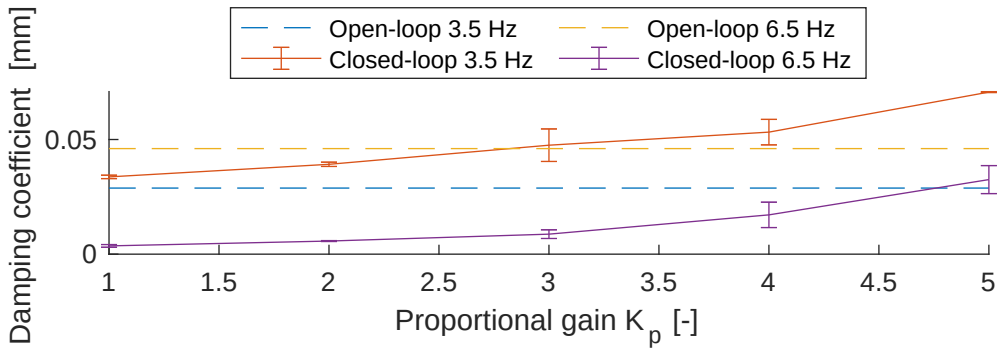

Figure 6.23: *Damping coefficient comparison for the aileron response with P control.*

Spoiler - Proportional Control

The data for GLA using proportional control show the most interesting results. The response over time, shown in figs. 6.24 and 6.25, both show little effect in amplitude and damping for $K_p = 1$, with the response almost equal to the open-loop response. For the higher gain values, the maximum deflection is halved for a gust of 3.5 Hz at both $K_p = 15$ and $K_p = 20$, as also visible in fig. 6.26. The overall greatest improvements in damping coefficient are obtained at $K_p = 20$; for the 6.5 Hz gust an absolute increase of $\zeta = 0.42$ and a relative increase in damping coefficient of 1300% for the 3.5 Hz gust, as seen in fig. 6.27.

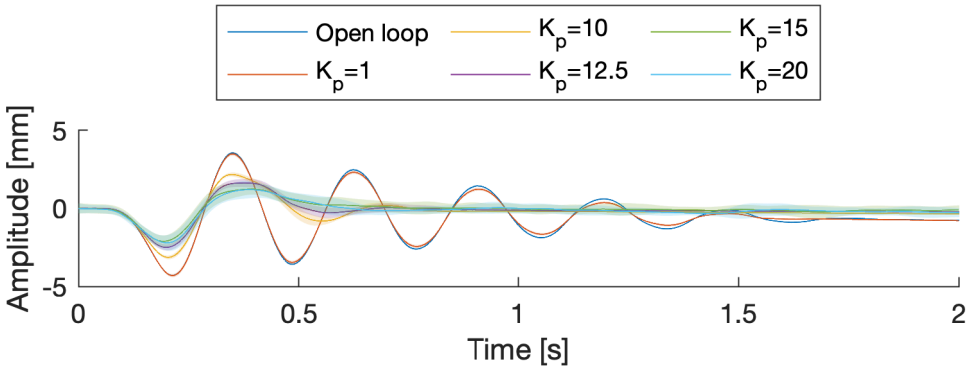

Figure 6.24: *Mean closed-loop spoiler response with P control, gust frequency 3.5 Hz.*

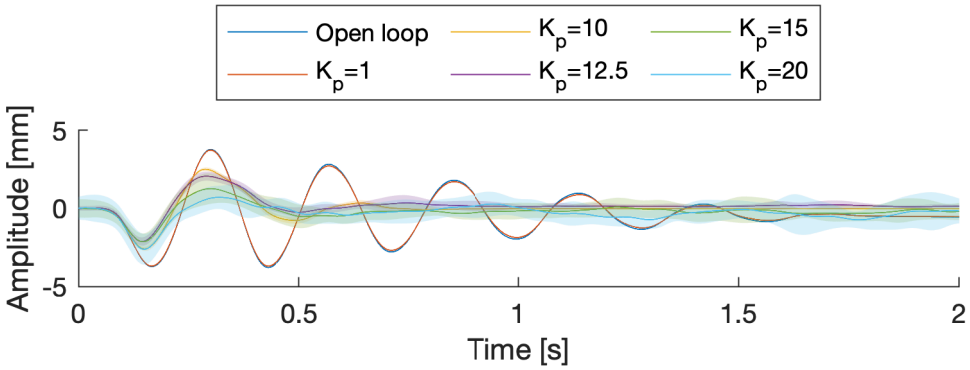

Figure 6.25: *Mean closed-loop spoiler response with P control, gust frequency 6.5 Hz.*

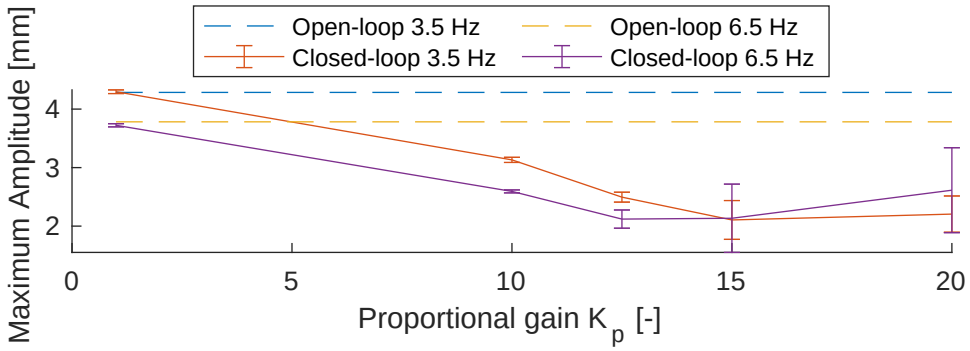

Figure 6.26: *Maximum amplitude comparison for the spoiler response with P control.*

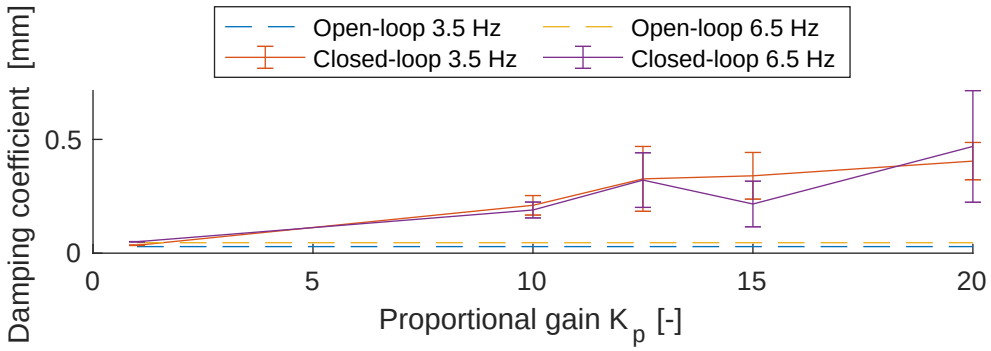

Figure 6.27: *Damping coefficient comparison for the spoiler response with P control.*

6.3.3. Discussion of GLA Results

Looking at the time response in figs. 6.20, 6.21, 6.24 and 6.25, several observations can be made. Comparing the aileron response with the spoiler response, the spoiler response is shown to be the most effective for the tested conditions. This can be attributed to two facts; as discussed earlier, a larger maximum change in lift coefficient can be achieved using the spoiler. Additionally, due to both inertia and kinematics of the mechanism, the spoiler has a faster response time compared to the aileron.

Several interesting observation can be made when looking at the standard deviation of the responses. Comparing the aileron and spoiler responses, it is clear that the aileron responses have a smaller standard deviation. This can be attributed to the fundamental differences induced on the flow by the deflection of the aileron and spoiler. The aileron changes the effective camber of the wing, thereby changing the pressure distribution along the wing and increasing or decreasing the generated lift. For small to moderate deflections, the flow can be assumed to remain attached, for higher deflection angles the flow may detach due to adverse pressure gradients. Spoilers however create large regions of separated flow together with vortices. In turn this produces more turbulent wakes, leading to the increased stochastic response.

7

Conclusion & Recommendations

7.1. Conclusions

This thesis set out to present the design and development of a parametric wing section with aileron and spoiler control surfaces to facilitate research in aeroelastic topics such as (active) gust load alleviation and flutter suppression. The wing section is to be used with the existing facilities at the Faculty of Aerospace Engineering of Delft University of Technology, such as the aeroelastic apparatus, gust generator and M- and W-tunnels.

Relatively little literature was found on the use of spoilers for aeroelastic control. To this end, a linearized potential theory for spoilers was chosen from multiple available methods and implemented. While the method is computationally inexpensive, it has the disadvantage of requiring empirical input in the form of a base pressure coefficient of the wake developed behind the spoiler. The verification of the aerodynamic model showed good agreement with previous experimental results. As the empirical input for the current wing section is missing, the base pressure coefficients were assumed to match those of different experiments for the purpose of validation. The results however show that this assumption is invalid. The base pressure coefficients should therefore be experimentally obtained for the wing section itself and used to recalculate the results to validate the aerodynamic model.

The wing section was designed to replace the current wing section, which lacks control surfaces. The final product is a wing section with 160 mm chord, 378 mm span and a NACA 0014 airfoil, equipped with a $0.25c$ aileron and $0.135c$ spoiler at $0.68c$. A freeplay mechanism is included the aileron actuation mechanism, allowing for aeroelastic research with control surface free play. The second parametric feature is the movable axis of rotation of the wing. The wing section is a self-contained package, with a single-board computer (BeagleBone Blue), instrumentation and power supply integrated into the wing. The control architecture that is run on the BeagleBone Blue is programmed using Simulink.

A host of system identification tests were performed to gain knowledge of the dynamic behavior of the both the servomotor and wing section. Though the aileron shows a greater control surface effectiveness for steady aerodynamics, its dynamic response is reduced due to the larger inertia of the aileron actuation mechanism. Control surface effectiveness tests show a reduction, loss and reversal of aileron control occurring for spoiler deflections between $15\,\text{deg} \leq \delta \leq 30\,\text{deg}$. Differences in ΔC_L are shown to be negligible for $\delta \geq 60\,\text{deg}$.

Finally, as a proof of concept, several gust load alleviation tests were performed using PID control with aileron and spoiler control. Open-loop results show the largest effect of the gust excitation for a gust frequency of 3.5 Hz, near the first structural mode. GLA using spoiler control shows the greatest improvement with respect to the open-loop results, showing a 50% reduction in amplitude and a 13-fold increase of damping coefficient. Linking back to the previous paragraph, limiting the maximum spoiler deflection to 60 deg should further improve this response by enabling a faster reaction.

7.2. Recommendations

Based on both experiences obtained during the manufacturing of and testing with the wing, as well as the results presented in the previous chapter, the following recommendations are made:

Several parametric features are incorporated into the wing. However, tests were performed for only a single condition, the axis of rotation at $0.4c$ and zero aileron free play. It is recommended to perform the system identification test for all possible configurations, such that the operational limits of wing section can be cataloged. Additionally, the effect of limiting the control surface deflections and the ratio of servo actuator deflection to control surface deflection can be considered, to investigate the effect of the control surface deflection rate on GLA.

The aerodynamic model implemented for the spoiler shows great potential. The model has one disadvantage, requiring empirical input, the base pressure coefficient, for each spoiler deflection. This input was missing for this work, proving it to be impossible to validate the aerodynamic model at this time. It is therefore recommended to determine and catalog the base pressure coefficient over a range of operating conditions, by placing a pressure tap in the region behind the spoiler, as well as measuring the static pressure upstream of the wing section, as done in the experiments by Brown [72]. In addition, PIV and CFD studies can be performed to both identify the wake structures developed by the spoiler, giving additional verification and validation data. Furthermore, the aerodynamic model for the spoiler is similar to that of Theodorsen. Additional effort should be made to convert it in a form compatible with a state-space representation, allowing for quicker methods to determine the aero(servo)elastic response of a wing (section) in preliminary design stages.

The GLA results presented in this work relied on a relatively crude control system with PID control, to serve as a proof of concept. The results are therefore likely to be far from optimal. Because the model is programmed using Simulink, it should be possible to implement newer, more effective control strategies such as model predictive control (MPC), model reference adaptive control (MRAC) or incremental nonlinear dynamic inversion (INDI). With such control strategies implemented, it is recommended to redo the GLA tests and compare the results of GLA using aileron and spoiler control again. In addition to research into GLA, it is also recommended to implement these control strategies to investigate flutter suppression.

Another recommendation with respect to the GLA results is increasing the period between the individual gusts. Results show an increase in standard deviation for increasingly aggressive control responses. This is particularly noticeable for responses with the spoiler, which produces a turbulent wake, impacting consecutive responses. By increasing the period between gusts, the turbulence should dissipate and the deviation should decrease.

Finally, some recommendations are made with respect to the wing section and test setup itself. The wing section is designed to be a self-sufficient package. In itself not an issue, but due to the limited size of the wing, little space is available for the batteries. The two 550 mAh LiPo batteries allow for approximately 15 minutes of uninterrupted testing, after which the system has to be shut down, the batteries have to be replaced and the system has to be rebooted again. This sequence can cost up to 10 minutes, assuming sufficient charged batteries are available. A disadvantage of LiPo batteries is that they should not be discharged below a certain voltage, as this may damage the batteries. This requires the user to keep an eye on the voltage level, or include an automatic shutdown if this threshold voltage is reached. As wind tunnel slots are a valuable and expensive resource, efficient use of time is desirable. The possibility of incorporating an external power supply is therefore highly recommended.

The possibility to investigate the effect of control surface free play is incorporated in the wing section. With the current wing section, it is however not possible to measure the aileron deflection directly, as this is obtained through the measured servo actuator deflection. Therefore if free play is introduced, an uncertainty exists between the actual and measured aileron angle. The recommendation is made to measure the actual aileron deflection on either the output shaft of the FPM or an the axle of the aileron hinge itself. Preferably this is done using a low-friction method - to minimize influence on the system - such as with a rotary encoder Hall effect sensor. Additionally, for the purpose of this work, the control surface actuation mechanisms were assumed to be rigid. Unfortunately this is not the real case, as the plastic servo horns allow for some flexibility in the mechanisms. The effects of this flexibility are negligible for the purpose of this work, but it is recommended to reinforce (or replace) the servo horns to eliminate this source of uncertainty when performing additional research on control.

As mentioned in section 4.4, sensor input is provided by the 9-axis IMU of the BBBLue. This input can be noisy and has a bias, requiring additional filtering. To determine the displacement of the wing,

this data has to be numerically integrated, invariably introducing drift of the displacement. This issue not only counts for the displacement obtained from the acceleration, but also for the pitch angle, obtained by integrating the pitch rate. To counteract these issues, the external LVDT and RVDT are recommended to be connected to the BBBLue, allowing for direct measurement of the heave and pitch DOFs.

Continuing on the recommendation made in the previous paragraph, an overhaul of the Simulink program and data acquisition method is also recommended. The program was run in what is called “external mode” for these tests. This the program runs on both the BBBLue and a PC, maintaining an active connection between each other. This also allows measured signals to be monitored on scopes and parameters to be changed during execution of the program.

The final recommendation concerns the aeroelastic apparatus. The aeroelastic provides both the heave and pitch DOFs for the wing section. This is fine for aeroelastic testing, however to fully characterize the aerodynamic behavior of a wing section it is desirable to have some sort of control over the pitch angle. With the current setup, this can be done by adjusting the nuts and bolts that serve as end stops for the pitching motion. This is certainly not an accurate way to set angles within a certain degree of accuracy. The development of a form of pitch control with servo actuators is recommended for this purpose.

Bibliography

[1] Wykes, J. H., Mori, A. S., and Borland, C. J., "B-1 structural mode control system," *4th Aircraft Design, Flight Test, and Operations Meeting*, AIAA, Los Angeles, CA, 1972, pp. 1–8. doi:10.2514/6.1972-772, URL https://arc.aiaa.org/doi/10.2514/6.1972-772.

[2] Britt, R., Volk, J., Dreim, D., and Applewhite, K., "Aeroelastic Characteristics of the B-2 Bomber and Implications for Future Large Aircraft," *RTO Meeting in Ottowa*, 2000, pp. 1–12.

[3] Brown, G. P., and Parkinson, G. V., "A linearized potential flow theory for airfoils with spoilers," *Journal of Fluid Mechanics*, Vol. 57, No. 4, 1973, pp. 695–719. doi:10.1017/S0022112073001965.

[4] Bernier, R., "Steady and Transient Aerodynamics of Spoilers on Airfoils," Ph.D. thesis, University of British Columbia, 1977. URL https://open.library.ubc.ca/cIRcle/collections/ubctheses/831/items/1.0094036.

[5] ICAO, "20 Year Passenger Forecast," , 2021. URL https://www.iata.org/pax-forecast/, retrieved January 14th, 2022.

[6] on Climate Change Secretariat, U. N. F. C., "Paris Agreement," , 2015. URL https://unfccc.int/files/meetings/paris_nov_2015/application/pdf/paris_agreement_english_.pdf, retrieved January 14th, 2022.

[7] Transportation Safety Board of Canada, "Severe turbulence encounter," , 2019. URL https://www.tsb.gc.ca/eng/enquetes-investigations/aviation/2019/a19f0176/a19f0176.html, retrieved November 1st, 2021.

[8] Major Aircraft Accident Investigation Board (Strategic Air Command), "Accident Report "Buzz One Four"," USAF Accident/Incident Report, United States Air Force, June 1964.

[9] Raad voor de Luchtvaart, "Uitspraak van de Raad voor de Luchtvaart inzake het ongeval op 6 oktober 1981 nabij Moerdijk overkomen aan het vliegtuig PH-CHI," , 1983.

[10] Wright, J. R., and Cooper, J. E., "Gust and Turbulence Encounters," *Introduction to Aircraft Aeroelasticity and Loads*, John Wiley & Sons Ltd, Chichester, UK, 2015, Chap. 14, 2nd ed., pp. 299–335. doi:10.1002/9781118700440.ch14, URL http://doi.wiley.com/10.1002/9781118700440.ch14.

[11] Department of Transportation, Federal Aviation Administration, "14 CFR, Part 25, §25.341, Gust and turbulence loads," , November 2020. URL https://www.ecfr.gov/cgi-bin/retrieveECFR?gp=&SID=4442d02114dfe195b54c5df6376a9797&mc=true&r=PART&n=pt14.1.25#se14.1.25_1341, retrieved February 10th, 2021.

[12] Regan, C. D., and Jutte, C. V., "Survey of Applications of Active Control Technology for Gust Alleviation and New Challenges for Lighter-weight Aircraft," Tech. rep., NASA, Edwards, CA, 2012. URL https://ntrs.nasa.gov/archive/nasa/casi.ntrs.nasa.gov/20120013450.pdf.

[13] Burris, P., and Bender, M., "Aircraft Load Alleviation and Mode Stabilization (LAMS) - B-52 System Analysis, Synthesis, and Design," Technical Report AFFDL-TR-68-161, Air Force Flight Dynamics Laboratory, Dayton, OH, 1971.

[14] Arnold, J. I., and Murphy, F. B., "B-52 Control Configured Vehicles: Flight Test Results," *Advanced Control Technology and Its Potential for Future Transport Aircraft*, Dryden Flight Research Center, Edwards, CA, 1976, pp. 75–89.

[15] Disney, T., and Eckholdt, D., "Historical Review of C-5A Lift Distribution Control Systems," *Proceedings of NASA Sponsored Symposium on Advanced Control Technology and Its Potential for Future Transport Aircraft*, NASA, 1969, pp. 295–323.

[16] Disney, T., "The C-5A Active Load Alleviation System," *Aircraft Systems and Technology Meeting*, AIAA, Reston, VA, 1975, pp. 1–8. doi:10.2514/6.1975-991, URL http://arc.aiaa.org/doi/10.2514/6.1975-991.

[17] Hargrove, W. J., "The C-5A Active Lift Distribution Control System," *Proceedings of NASA Sponsored Symposium on Advanced Control Technology and Its Potential for Future Transport Aircraf*, National Aeronautics and Space Administration, 1975, pp. 325–351.

[18] Hönlinger, H., Zimmerman, H., Sensburg, O., and Becker, J., "Structural Aspects of Active Control Technology," *Active Control Technology: Applications and Lessons Learned*, AGARD, Turin, 1995, pp. 18–1–18–10.

[19] Wykes, J. H., and Knight, R. J., "Progress report on a gust alleviation and structural dynamic stability augmentation system (GASDSAS) design study," *AIAA 3rd Annual Meeting*, AIAA, Boston, MA, 1966, pp. 1–17. doi:10.2514/6.1966-999, URL http://arc.aiaa.org/doi/10.2514/6.1966-999.

[20] Bonnema, K. L., and Smith, S. B., "AFTI/F-111 Mission Adaptive Wing flight research program," *4th Flight Test Conference*, American Institute of Aeronautics and Astronautics, Reston, VA, 1988, pp. 155–161. doi:10.2514/6.1988-2118, URL http://arc.aiaa.org/doi/10.2514/6.1988-2118.

[21] Vipperman, J. S., Clark, R. L., Conner, M., and Dowell, E. H., "Experimental Active Control of a Typical Section Using a Trailing-Edge Flap," *Journal of Aircraft*, Vol. 35, No. 2, 1998, pp. 224–229. doi:10.2514/2.2312, URL https://arc.aiaa.org/doi/10.2514/2.2312.

[22] Cassaro, M., Nágy, A., Marzocca, P., Battipede, M., and Ahmadi, G., "Novel Active Control Strategy for LCO and Flutter Suppression by a Coordinated Use of Multiple Distributed Surface Actuators," *Volume 1: Advances in Aerospace Technology*, Vol. 1, American Society of Mechanical Engineers, 2014, p. 7. doi:10.1115/IMECE2014-36905, URL https://asmedigitalcollection.asme.org/IMECE/proceedings/IMECE2014/46421/Montreal,Quebec,Canada/261292.

[23] Cassaro, M., Battipede, M., Marzocca, P., and Ahmadi, G., "Aeroelastic System Control by a Multiple Spoiler Actuation and MRAC Scheme," *56th AIAA/ASCE/AHS/ASC Structures, Structural Dynamics, and Materials Conference*, AIAA, Reston, VA, 2015, pp. 1–14. doi:10.2514/6.2015-1851, URL http://arc.aiaa.org/doi/10.2514/6.2015-1851.

[24] Lancelot, P., and De Breuker, R., "Passively actuated spoiler for gust load alleviation," *27th International Conference on Adaptive Structures and Technologies*, 2016. URL https://repository.tudelft.nl/islandora/object/uuid%3A29f86d2a-7cd1-4159-96a2-c880a5b9c53d?collection=research.

[25] Quenzer, J. D., Zongolowicz, A., Hinson, K. A., Barzgaran, B., Livne, E., Mesbahi, M., and Morgansen, K., "Model for Aeroelastic Response to Gust Excitation," *AIAA Scitech 2019 Forum*, American Institute of Aeronautics and Astronautics, Reston, Virginia, 2019, p. 23. doi:10.2514/6.2019-2031, URL https://arc.aiaa.org/doi/10.2514/6.2019-2031.

[26] Barzgaran, B., Quenzer, J. D., Zongolowicz, A., Hinson, K., Mesbahi, M., Morgansen, K., and Livne, E., "Low-cost wind tunnel studies of gust alleviation control techniques," *International Forum on Aeroelasticity and Structural Dynamics 2019, IFASD 2019*, Savannah, GA, 2019, pp. 1–18.

[27] Cheung, R. C., Rezgui, D., Cooper, J. E., and Wilson, T., "Testing of Folding Wingtip for Gust Load Alleviation of Flexible High-Aspect-Ratio Wing," *Journal of Aircraft*, Vol. 57, No. 5, 2020, pp. 876–888. doi:10.2514/1.C035732, URL https://arc.aiaa.org/doi/10.2514/1.C035732.

[28] Obert, E., "Lift Spoiling Control Surfaces (Spoiler Panels)," *Aerodynamic Design of Transport Aircraft*, IOS Press, Amsterdam, 2009, Chap. 34, pp. 433–440.

[29] Raymer, D. P., "Control-Surface Sizing," *Aircraft Design: A Conceptual Approach*, edited by J. A. Schetz, American Institute of Aeronautics and Astronautics, Reston, Va., 2006, Chap. 6, 4th ed., pp. 123–126.

[30] Whitford, R., *Design for Air Combat*, IHS Jane's, London, 1987.

[31] Naval Air Systems Command, "F-14D NATOPS Flight Manual," , 2004.

[32] , ???? URL https://i.stack.imgur.com/5AUQi.jpg, retrieved October 26th, 2021.

[33] Dempster, J. B., and Roger, K. L., "Evaluation of B-52 structural response to random turbulence with various stability augmentation systems," *3rd Annual Meeting*, American Institute of Aeronautics and Astronautics, Reston, VA, 1966, p. 14. doi:10.2514/6.1966-998, URL http://arc.aiaa.org/doi/10.2514/6.1966-998.

[34] Roskam, J., Kohlman, D. L., and Wentz, W. H. J., "Spoilers for roll control of light airplanes," *Mechanics and Control of Flight Conference*, American Institute of Aeronautics and Astronautics, Reston, VA, 1974, p. 13. doi:10.2514/6.1974-861, URL http://arc.aiaa.org/doi/10.2514/6.1974-861.

[35] Kohlman, D. L., "Flight Test Results for an Advanced Technology Light Airplane," *Journal of Aircraft*, Vol. 16, No. 4, 1979, pp. 250–255. doi:10.2514/3.58513, URL https://arc.aiaa.org/doi/10.2514/3.58513.

[36] Friend, E. L., and Sakamoto, G. M., "Flight Comparison of the Transonic Agility," Tech. rep., NASA, Washington, D.C., 1978.

[37] Trujll, B., Meyer, R., Jr., and Chiles, H., "Techniques used in the F-14 variable-sweep transition flight experiment," *4th Flight Test Conference*, American Institute of Aeronautics and Astronautics, Reston, VA, 1988, pp. 529–548. doi:10.2514/6.1988-2110, URL http://arc.aiaa.org/doi/10.2514/6.1988-2110.

[38] Balas, G. J., Packard, A. K., Renfrow, J., Mullaney, C., and M'Closkey, R. T., "Control of the F-14 aircraft lateral-directional axis during powered approach," *Journal of Guidance, Control, and Dynamics*, Vol. 21, No. 6, 1998, pp. 899–908. doi:10.2514/2.4323.

[39] Bulfer, B., *737NG Cockpit Companion*, Leading Edge Publishing, Merced, CA, 1998.

[40] Wentz, W. H. J., "Wind tunnel tests of the GA(W)-2 airfoil with 20% aileron, 25% slotted flap, 30% Fowler flap and 10% slot-lip spoiler," Contractor Report CR-145139, National Aeronautical and Space Administration, 1977. URL https://ntrs.nasa.gov/search.jsp?R=19790001850.

[41] Mack, M. D., Seetharam, H. C., Kuhn, W. G., and Bright, J. T., "Aerodynamics of spoiler control devices," *Aircraft Systems and Technology Meeting*, AIAA, American Institute of Aeronautics and Astronautics, Reston, VA, 1979, pp. 1–18. doi:10.2514/6.1979-1873, URL http://arc.aiaa.org/doi/10.2514/6.1979-1873.

[42] Pfeiffer, N. J., and Zumwalt, G. W., "A computational model for low speed flows past airfoils with spoilers," *19th Aerospace Sciences Meeting*, Vol. 20, No. 3, 1981, pp. 376–382. doi:10.2514/6.1981-253, URL http://arc.aiaa.org/doi/10.2514/6.1981-253.

[43] McLachlan, B., Karamcheti, K., and van Leynseele, F., "Experimental study of the flowfield of an airfoil with deflected spoiler," *20th Aerospace Sciences Meeting*, American Institute of Aeronautics and Astronautics, Reston, Virigina, 1982, p. 8. doi:10.2514/6.1982-126, URL http://arc.aiaa.org/doi/10.2514/6.1982-126.

[44] Bodapati, S., Karamcheti, K., and Mack, M. D., "Basic studies of the flow fields of airfoil-flap-spoiler systems," *20th Aerospace Sciences Meeting*, American Institute of Aeronautics and Astronautics, Reston, VA, 1982, p. 9. doi:10.2514/6.1982-173, URL http://arc.aiaa.org/doi/10.2514/6.1982-173.

[45] Lee, C. S., and Bodapati, S., "A comparison between theoretical and experimental flow fields of an airfoil with deflected spoiler," *23rd Aerospace Sciences Meeting*, American Institute of Aeronautics and Astronautics, Reston, VA, 1985, p. 10. doi:10.2514/6.1985-269, URL http://arc.aiaa.org/doi/10.2514/6.1985-269.

[46] Consigny, H., Gravelle, A., and Molinaro, R., "Aerodynamic characteristics of a two-dimensional moving spoiler in subsonic and transonic flow," *Journal of Aircraft*, Vol. 21, No. 9, 1984, pp. 687–693. doi:10.2514/3.45015, URL https://arc.aiaa.org/doi/10.2514/3.45015.

[47] Tou, H. B., and Hancock, G. J., "Part IV: Oscillatory aerofoil/spoiler characteristics," *The Aeronautical Journal*, Vol. 91, No. 909, 1987, pp. 410–428. doi:10.1017/S0001924000021655, URL https://www.cambridge.org/core/product/identifier/S0001924000021655/type/journal_article.

[48] Tou, H. B., and Hancock, G. J., "Part II: Steady aerofoil-spoiler characteristics," *The Aeronautical Journal*, Vol. 91, No. 908, 1987, pp. 359–366. doi:10.1017/S0001924000021540, URL https://www.cambridge.org/core/product/identifier/S0001924000021540/type/journal_article.

[49] Tou, H. B., and Hancock, G. J., "Part III: On an incremental problem related to the steady flow about an aerofoil/spoiler configuration," *The Aeronautical Journal*, Vol. 91, No. 909, 1987, pp. 406–410. doi:10.1017/S0001924000021643, URL https://www.cambridge.org/core/product/identifier/S0001924000021643/type/journal_article.

[50] Tou, H. B., and Hancock, G. J., "Part V: Steady and oscillatory aerofoil-spoiler-flap characteristics," *The Aeronautical Journal*, Vol. 91, No. 910, 1987, pp. 479–492. doi:10.1017/S0001924000050661, URL https://www.cambridge.org/core/product/identifier/S0001924000050661/type/journal_article.

[51] Tou, H. B., and Hancock, G. J., "Part VI: The rapid deployment of a spoiler on a two-dimensional aerofoil," *The Aeronautical Journal*, Vol. 91, No. 910, 1987, pp. 492–498. doi:10.1017/S0001924000050673, URL https://www.cambridge.org/core/product/identifier/S0001924000050673/type/journal_article.

[52] Geisbauer, S., and Löser, T., "Towards the Investigation of Unsteady Spoiler Aerodynamics," *35th AIAA Applied Aerodynamics Conference*, American Institute of Aeronautics and Astronautics, Reston, Virginia, 2017, pp. 1–19. doi:10.2514/6.2017-4229, URL https://arc.aiaa.org/doi/10.2514/6.2017-4229.

[53] Wentz, W. H. J., Ostowari, C., and Seetharam, H. C., "Effects of design variables on spoiler control effectiveness, hinge moments, and wake turbulence," *19th Aerospace Sciences Meeting*, American Institute of Aeronautics and Astronautics, Reston, VA, 1981, pp. 418–424. doi:10.2514/6.1981-72, URL http://arc.aiaa.org/doi/10.2514/6.1981-72.

[54] Vos, R., and Farokhi, S., "Pressure Distribution Over Nonlifting Bodies," *Introduction to Transonic Aerodynamics*, edited by A. Thess, Springer, Dordrecht, 2015, Chap. 6, pp. 279–286.

[55] Geisbauer, S., "Numerical Simulation and Validation of the Aerodynamics of Static and Dynamic Spoilers," *AIAA AVIATION 2020 FORUM*, Vol. 1 PartF, American Institute of Aeronautics and Astronautics, Reston, VA, 2020, pp. 1–23. doi:10.2514/6.2020-2776, URL https://arc.aiaa.org/doi/10.2514/6.2020-2776.

[56] Zumwalt, G. W., and Naik, S., "An Analytical Model for Highly Separated Flow on Airfoils at Low Speed," Tech. rep., National Aeronautics and Space Administration, Hampton, VA, 1977. URL https://ntrs.nasa.gov/citations/19770016107.

[57] Pfeiffer, N. J., and Zumwalt, G. W., "A computational model for low speed flows past airfoils with spoilers," *19th Aerospace Sciences Meeting*, American Institute of Aeronautics and Astronautics, Reston, Virigina, 1981. doi:10.2514/6.1981-253, URL http://arc.aiaa.org/doi/10.2514/6.1981-253.

[58] Tou, H. B., and Hancock, G. J., "Part I: Some experiences on simple panel methods applied to attached and separated flows," *The Aeronautical Journal*, Vol. 91, No. 908, 1987, pp. 350–359. doi:10.1017/S0001924000021539, URL https://www.cambridge.org/core/product/identifier/S0001924000021539/type/journal_article.

[59] Pfeiffer, N. J., "Analysis of Jet Transport Wings with Deflected Control Surfaces by using a Combination of 2- and 3-D Methods," *ICAS Proceedings 1982*, ICAS, Seattle, 1982, pp. 1454–1458.

[60] Pfeiffer, N. J., "Modeling of wings with deflected spoilers using potential flow," *16th AIAA Applied Aerodynamics Conference*, 1998, pp. 640–647. doi:10.2514/6.1998-2739.

[61] Theodorsen, T., "Report No. 496, general theory of aerodynamic instability and the mechanism of flutter," *Journal of the Franklin Institute*, Vol. 219, No. 6, 1935, pp. 766–767. doi:10.1016/S0016-0032(35)92022-1, URL https://linkinghub.elsevier.com/retrieve/pii/S0016003235920221.

[62] Woods, L., "Theory of Aerofoil Spoilers," Tech. rep., Aeronautical Research Council, London, 1956.

[63] Barnes, C., "A Developed Theory of Spoilers on Aerofoils," Tech. rep., Aeronautical Research Council, London, 1966.

[64] Kridner, J., "BeagleBone Blue Balloons," , 2017. URL https://github.com/beagleboard/beaglebone-blue/blob/master/docs/BeagleBone_Blue_balloons.pdf, retrieved January 14th, 2022.

[65] Department, A., "M-Tunnel," , 2020. URL https://www.tudelft.nl/lr/organisatie/afdelingen/aerodynamics-wind-energy-flight-performance-and-propulsion/facilities/low-speed-wind-tunnels/m-tunnel, retrieved January 14th, 2022.

[66] Geertsen, J. A., "Development of a Gust Generator for a Low Speed Wind Tunnel," Master's thesis, ETH Zürich, 2020.

[67] Gjerek, B., Drazumeric, R., and Kosel, F., "A Novel Experimental Setup for Multiparameter Aeroelastic Wind Tunnel Tests," *Experimental Techniques*, Vol. 38, No. 6, 2014, pp. 30–43. doi:10.1111/j.1747-1567.2012.00839.x, URL http://doi.wiley.com/10.1111/j.1747-1567.2012.00839.x.

[68] Roizner, F., and Karpel, M., "Parametric Flutter Margin Method for Aeroservoelastic Stability Analysis," *AIAA Journal*, Vol. 56, No. 3, 2018, pp. 1011–1022. doi:10.2514/1.J056514, URL https://arc.aiaa.org/doi/10.2514/1.J056514.

[69] Sodja, J., Roizner, F., De Breuker, R., and Karpel, M., "Experimental characterisation of flutter and divergence of 2D wing section with stabilised response," *Aerospace Science and Technology*, Vol. 78, 2018, pp. 542–552. doi:10.1016/j.ast.2018.05.014, URL https://doi.org/10.1016/j.ast.2018.05.014.

[70] Tam Doo, P. A., "A Prediction Method for Spoiler Performance," Ph.D. thesis, University of British Columbia, 1977. doi:10.14288/1.0081013, URL https://open.library.ubc.ca/cIRcle/collections/ubctheses/831/items/1.0081013.

[71] Dimitriadis, G., *Introduction to Nonlinear Aeroelasticity*, 1st ed., John Wiley & Sons, Ltd, Chichester, UK, 2017. doi:10.1002/9781118756478, URL http://doi.wiley.com/10.1002/9781118756478.

[72] Brown, G. P., "Steady and Nonsteady Potential Flow Methods for Airfoils with Spoilers," Ph.D. thesis, University of British Columbia, 1971. URL https://open.library.ubc.ca/cIRcle/collections/ubctheses/831/items/1.0101512.

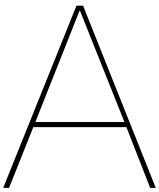

Analog-to-Digital Converter Settings

The tables below give the config register setting used during wind tunnel testing. Table A.1 shows the setting for reading the servo output, table A.2 shows the settings for reading the LVDT/RVDT.

Table A.1: *ADS1015 config register settings for single-ended, continuous mode, used to read the servo output.*

Bit	Description	Setting	
15	Operational status	0	No effect/performing conversion
14:12	Input multiplexer configuration	100	AIN_p = AIN0, AIN_n = GND
11:9	PGA configuration	001	±4.096V
8	Device operating mode	0	Continuous mode
7:5	Data rate	111	3300 SPS
4	Comparator mode	0	Traditional comparator
3	Comparator polarity	0	Active low
2	Latching comparator	0	Nonlatching comparator
1:0	Comparator queue and disable	11	Disable

Table A.2: *ADS1015 config register settings for differential, continuous use, used to read the LVDT/RVDT.*

Bit	Description	Setting	
15	Operational status	0	No effect/performing conversion
14:12	Input multiplexer configuration	000	AIN_p = AIN0, AIN_n = AIN1
11:9	PGA configuration	001	±4.096V
8	Device operating mode	0	Continuous mode
7:5	Data rate	111	3300 SPS
4	Comparator mode	0	Traditional comparator
3	Comparator polarity	0	Active low
2	Latching comparator	0	Nonlatching comparator
1:0	Comparator queue and disable	11	Disable

B

Spoiler Aerodynamic Model MATLAB Code

Listing B.1: *CalcMappingConst, eqs.* (3.12) *and* (3.13).

```
function [a, b] = CalcMappingConst(wake_length,chord,s,h)
% Calculate the constants for the conformal mapping of the z'-plane to
% the upper half of the nu-plane, according to the method by Brown.
%
% (c) R.R.M. Schildkamp, 2021

a = sqrt((wake_length - chord) ./ chord);

% Constant b
b = a .* sqrt((s + h) ./ (wake_length - s - h));

end
```

Listing B.2: *CalcAngularPos, eqs.* (3.14) *to* (3.16).

```
 function [theta_0, theta_1, theta_2] = CalcAngularPos(a,b,wake_length,
    chord,chord_aileron,s)
% Calculate the angular position of the leading edge, spoiler base and
% flap hinge point in the zeta-plane on the unit circle, according to
% the method by Brown.
%
% (c) R.R.M. Schildkamp, 2021

% Leading edge
theta_0 = acos((1 - b) / (1 + b));

% Spoiler base
theta_1 = acos(tmp_func1(b) * (a * sqrt(s / (wake_length - s)) + ...
    tmp_func2(b)));

```

```
% Flap hinge point
theta_2 = acos(tmp_func1(b) * (tmp_func2(b) - a * ...
    sqrt((chord - chord_aileron) / ...
    (wake_length - chord + chord_aileron) ) ));


% Local functions
    function y = tmp_func1(b)
        y = 2 / (1 + b);
    end

    function y = tmp_func2(b)
        y = (1 - b) / 2;
    end

end
```

Listing B.3: *CalcInfPt, eq.* (3.28).

```
function zeta_inf = CalcInfPt(a,b)
% Calculate the point at infinity in the zeta-plane, according to
% the method by Brown.
%
% (c) R.R.M. Schildkamp, 2021

% Intermediate term 1
tmp_1 = 2 / (1 + b);

% Intermediate term 2
tmp_2 = 1i * a + 0.5 * (1 - b);

% Point at infinity
zeta_inf = tmp_1 * tmp_2 + sqrt(tmp_1^2 .* tmp_2^2 - 1);

end
```

Listing B.4: *CalcLaurentCoeff.*

```
function [a_0, a_1] = CalcLaurentCoeff(a,b)
% Calculate the Laurent expansion coefficients, according to
% the method by Brown.
%
% (c) R.R.M. Schildkamp, 2021

% Intermediate values
tmp_1 = (1 - b) / (1 + b);
tmp_2 = (1i * a) / (1 + b);

% a0
a_0 = tmp_1 + 2 * tmp_2 + sqrt((tmp_1 + 2 .* tmp_2).^2 - 1);

% a1
a_1 = tmp_2 .* (1 + (tmp_1 + 2 .* tmp_2) ./ sqrt((tmp_1 + 2 .* ...
    tmp_2).^2 - 1));

end
```

Listing B.5: *CalcLambda, eqs.* (3.31) *and* (3.32).

```
function [lambda_1, lambda_2] = CalcLambda(zeta_inf,theta_0)
% Calculate constants lambda_1 and lambda_2 to solve the boundary
% condition at infinity, according to the method by Brown.
%
% (c) R.R.M. Schildkamp, 2021

% Lambda_1
lambda_1 = 1i * (tmp_func(zeta_inf,theta_0) + ...
    tmp_func(zeta_inf,-theta_0) + 1);

% Lambda_2
lambda_2 = 1i * (zeta_inf - (1 / zeta_inf));

% Local function
    function y = tmp_func(zeta,theta)
        y = 1 / (zeta * exp(1i * theta) - 1);
    end

end
```

Listing B.6: *CalcNCoeff, eqs.* (3.21) *and* (3.22).

```
function [N0, Nn] = CalcNCoeff(theta_0,wake_length,a,b,chord,thickness,
    airfoil,m,p,n_max)
% Calculate the Fourier series coefficients Nn from 0 to n_max for the
% contribution of the thickness to the linearized aero model
%
% (c) R.R.M. Schildkamp, 2021


% Check input
if nargin < 10
    n_max = 10;
end

if nargin < 7
    airfoil = clarky;
    m = [];
    p = [];
end

% Create vector from 1 to n_max
n = 1:n_max;

% Create anonymous integrand function
fun = @(theta) IntFuncNn(theta, n, theta_0, wake_length, a, b, chord, ...
    thickness, airfoil, m, p);

% Integrate from 0 to pi, ArrayValued true to calculate for all n
int = integral(fun, 0, pi, 'ArrayValued', true);

% Calculate N0, Nn
N0 = 2 / pi * int(1);
Nn = 4 / pi * int(2:n_max+1);

```

```
end
```

Listing B.7: *IntFuncNn.*

```
function y = IntFuncNn(theta,n,theta_0,wake_length,a,b,chord,thickness,
    airfoil,m,p)
% Create the integrand function for the Fourier series coefficients Nn
%
% (c) R.R.M. Schildkamp, 2021

% Check input
if nargin < 9
    airfoil = clarky;
end

% Map angular position theta in zeta-plane to x-coordinates in z-plane
x = MapZetaToZ(wake_length, a, b, theta);

% Get derivative of the airfoil thickness distribution
if strcmp(airfoil,clarky)
    [~, ~, dydx, ~] = ClarkYSeries2(x, chord, thickness);
elseif strcmp(airfoil,naca)
    [~, dydx, ~] = NACA4Series(x, chord, thickness, m, p);
end

% Calculate integrand for N0, Nn
y0 = dydx .* (cos(theta_0) - cos(theta));
yn = y0 .* cos(n .* theta);

% Output
y = [y0, yn];

end
```

Listing B.8: *MapZetaToZ.*

```
function x = MapZetaToZ(wake_length,a,b,theta)
% Map unit circle in the zeta-plane to the airfoil in the z-plane,
% according to the method by Brown.
%
% (c) R.R.M. Schildkamp

% Intermediate term
tmp = 0.5 * (b + 1) .* cos(theta) - 0.5 * (1 - b);

% x-coordinate
x = (wake_length ./ a.^2 * tmp.^2) ./ (1 + (1 ./ a.^2) .* tmp.^2);

end
```

Listing B.9: *ClarkYSeries2.*

```
function [yt, yc, dytdx, dycdx] = ClarkYSeries2(x,chord,thickness,scale)
% Calculate the thickness and camber distributions of a Clark Y series
% airfoil of specified chord and thickness
%
% (c) R.R.M. Schildkamp, 2021
```

```
6
7  if nargin < 4
8      scale = 0;
9  end
10
11 % Normalize x with respect to chord
12 x = x / chord;
13
14 % Convert thickness from percentage to fraction
15 t = thickness / 100;
16
17 % Thickness distribution (of Gottingen 398 airfoil)
18 yt = (t / 0.1) * (0.29690 .* sqrt(x) - 0.12600 .* x - ...
19     0.35160 .* x.^2 + 0.28430 .* x.^3 - 0.10150 .* x.^4);
20
21 % Derivative of thickness distribution
22 dytdx = (t / 0.1) * (0.14845 ./ sqrt(x) - 0.12600 - ...
23     0.70320 .* x + 0.8529 .* x.^2 - 0.406 .* x.^3);
24
25 % Camber
26 % yc = zeros(size(x));
27 % yc(x<=0.3) = 0.0585 .* x(x<=0.3);
28 % yc(x>0.3) = -0.1117 .* sqrt(x(x>0.3)) + 0.3970 .* x(x>0.3) - ...
29 %     0.5549 .* x(x>0.3).^2 + 0.3943 .* x(x>0.3).^3 - 0.1239 .* x(x>0.3)
       .^4;
30
31 yc = -0.0593 .* sqrt(x) + 0.4359 .* x - 0.8395 .* x.^2 + ...
32     0.7172 .* x.^3 - 0.2549 .* x.^4;
33
34 % Camber
35 % beta = [0.000313817351758; 0.160387765068850; -0.163328632532524];
36 beta =  [-0.163328632532524; 0.160387765068850; 0.000313817351758];
37 %
38 yc = polyval(beta, x);
39
40 % Camber derivative
41 dycdx = 2 .* beta(1) .* x + beta(2);
42
43 % Scale with chord
44 if scale == 1
45     yt = yt * chord;
46     dytdx = dytdx * chord;
47
48     yc = yc * chord;
49     dycdx = dycdx * chord;
50 end
51
52 end
```

Listing B.10: *NACA4Series.*

```
1  function [y, dytdx, dycdx] = NACA4Series(x,chord,thickness,m,p,scale)
2  % Calculate the thickness distribution and its derivate of a NACA
3  % 4-series airfoil of specified chord and thickness
4  %
5  % (c) R.R.M. Schildkamp, 2021
6
```

```
% Input:
% x - airfoil x-coordinates
% chord - airfoil chord length
% thickness - airfoil thickness in %
% m - maximum thickness first digit of NACA designation i.e. x000
% p - location of maximum thickness

if nargin < 6
    scale = 0;
end

% Normalize x with respect to chord
x = x / chord;

% Convert from percent to fraction
t = thickness / 100;

% Thickness distribution
y = 5 * t .* (0.2969 .* sqrt(x) - 0.1260 .* x - ...
    0.3516 .* x.^2 + 0.2843 .* x.^3 - (0.1036 - 0.5/112) .* x.^4);

% Derivative of thickness distribution
dytdx = 5 * t .* (0.14845 ./ sqrt(x) - 0.1260 - 0.7032 .* ...
    x + 0.8529 .* x.^2 - 0.4060 .* x.^3);

% Derivative of camber distribution
dycdx = zeros(size(x));

dycdx(x<=p) = 2 * m / p^2 * (p - x(x<=p));
dycdx(x>p) = 2 * m / ((1 - p)^2) * (p - x(x>p));

% Scale with chord
if scale == 1
    y = y * chord;
    dytdx = dytdx * chord;
end

end
```

Listing B.11: *CalcMcoeff, eq.* (3.19).

```
function [M0, Mn] = CalcMcoeff(wake_length,a,b,chord,thickness,airfoil,m,p
    ,n_max)
% Calculate the Fourier series coefficients Mn from 0 to n_max for the
% contribution of the camber to the linearized aero model
%
% (c) R.R.M. Schildkamp, 2021

% Check input
if nargin < 7
    n_max = 10;
end

if nargin < 6
    airfoil = clarky;
    m = [];
    p = [];
```

```
end

% Create vector from 1 to n_max
n = 1:n_max;

% Create anonymous integrand function
fun = @(theta) IntFuncMn(theta, n, wake_length, a, b, chord, thickness, ...
    airfoil, m, p);

% Integrate from 0 to pi, ArrayValued true to calculate for all n
int = 2 / pi * integral(fun, 0, pi, 'ArrayValued', true);

% Calculate M0, Mn
M0 = int(1);
Mn = int(2:n_max+1);

end
```

Listing B.12: *IntFuncMn.*

```
function y = IntFuncMn(theta,n,wake_length,a,b,chord,thickness,airfoil,m,p
    )
% Create the integrand function for the Fourier series coefficients Mn
%
% (c) R.R.M. Schildkamp, 2021

if nargin < 8
    airfoil = clarky;
end

% Map angular position theta in zeta-plane to x-coordinates in z-plane
x = MapZetaToZ(wake_length, a, b, theta);

% Get derivative of the airfoil camber distribution
if strcmp(airfoil,clarky)
    [~, ~, ~, dydx] = ClarkYSeries2(x, chord, thickness);
elseif strcmp(airfoil,naca)
    [~, ~, dydx] = NACA4Series(x, chord, thickness, m, p);
end

% Calculate integrand for M0, Mn
y0 = dydx;
yn = y0 .* cos(n .* theta);

% Output
y = [y0, yn];

end
```

Listing B.13: *CalcComplexAccel*

```
function [F, Fcomp] = CalcComplexAccel(zeta,theta0,theta1,theta2,Mn,N0,Nn,
    delta,eta)
% Calculate the complex acceleration potential components, based on the
    method of Brown.
%
% (c) R.R.M. Schildkamp, 2021
```

```
5
6  % Camber
7  Fc = CalcComplexAccelC(zeta,Mn);
8
9  % Thickness
10 Ft = CalcComplexAccelT(zeta,theta0,N0,Nn);
11
12 % Spoiler
13 Fs = CalcComplexAccelS(zeta,delta,theta0,theta1);
14
15 % Flap
16 Ff = CalcComplexAccelF(zeta,eta,theta0,theta2);
17
18 % Output
19 Fcomp = [Fc, Ft, Fs, Ff];
20 F = sum(Fcomp);
21
22 end
23
24 function F_c = CalcComplexAccelC(zeta,Mn,n_max)
25 % Calculate the contribution of the airfoil camber to the complex
26 % acceleration potential
27 %
28 % (c) R.R.M. Schildkamp, 2021
29
30 % Check input
31 if nargin < 3
32     n_max = 10;
33 end
34
35 % Create vector from 1 to n_max
36 n = 1:n_max;
37
38 % Calculate complex acceleration potential
39 F_c = -1i * sum(Mn ./ (zeta.^n));
40
41 end
42
43 function F_t = CalcComplexAccelT(zeta,theta_0,N0,Nn,n_max)
44 % Calculate the contribution of the airfoil thickness to the complex
45 % acceleration potential
46 %
47 % (c) R.R.M. Schildkamp
48
49 % Check input
50 if nargin < 5
51     n_max = length(Nn);
52 end
53
54 % Vector from 0 to n_max
55 n = 0:n_max;
56
57 % Calculate constant term
58 tmp = 1i * zeta / (tmp_func(theta_0,zeta) * tmp_func(-theta_0,zeta));
59
60 % Calculate acceleration potential
```

```
61  F_t = tmp * sum([N0, Nn] ./ (zeta.^n));
62
63  % Local function
64      function y = tmp_func(theta,zeta)
65          y = zeta - exp(1i * theta);
66      end
67
68  end
69
70  function F_s = CalcComplexAccelS(zeta,delta,theta_0,theta_1)
71  % Calculate the contribution of the spoiler to the complex acceleration
72  % potential
73  %
74  % (c) R.R.M. Schildkamp
75
76  % Calculate complex acceleration potential
77  F_s = sin(delta) / pi * (tmp_func1(theta_0,theta_1,zeta) + ...
78      tmp_func1(-theta_0,theta_1,zeta) + ...
79      log(tmp_func2(theta_1,zeta) / tmp_func2(-theta_1,zeta)));
80
81  % Local functions
82  % Func 1
83      function y = tmp_func1(theta_0,theta_1,zeta)
84          y = 1i * theta_1 / (zeta * exp(1i * theta_0) - 1);
85      end
86
87  % Func 2
88      function y = tmp_func2(theta_1,zeta)
89          y = zeta - exp(1i * theta_1);
90      end
91  end
92
93  function F_f = CalcComplexAccelF(zeta,eta,theta_0,theta_2)
94  % Calculate the contribution of the airfoil flap to the complex
95  % acceleration potential
96  %
97  % (c) R.R.M. Schildkamp
98
99  % Calculate complex acceleration potential
100 F_f = eta / pi * (tmp_func1(theta_0,theta_2,zeta) + ...
101     tmp_func1(-theta_0,theta_2,zeta) + ...
102     log(tmp_func2(theta_2,zeta) / tmp_func2(-theta_2,zeta)));
103
104 % Local functions
105 % Func 1
106     function y = tmp_func1(theta_0,theta_2,zeta)
107         y = 1i * (theta_2 - pi) / (zeta * exp(1i * theta_0) - 1);
108     end
109
110 % Func 2
111     function y = tmp_func2(theta_2,zeta)
112         y = zeta - exp(1i * theta_2);
113     end
114 end
```

Listing B.14: *CalcCavitationNumberK, eq.* (3.35).

```
function [K, Kcomp] = CalcCavitationNumberK(l,a0,a1,l1,l2,theta0,theta1,
    theta2,F,alpha,delta,eta,M0,Mn,N0,Nn)
% Calculate the components of the cavitation number
%
% (c) R.R.M. Schildkamp, 2021

% Calc denominator
Kden = CalcKden(l,a0,a1,l1,l2,theta0);

% Calc incidence contribution
Kalpha = CalcKalpha(l,a0,a1,l1,l2,theta0,Kden,alpha);

% Calc camber contribution
Kc = CalcKc(l,a0,a1,l1,l2,theta0,Kden,F(1),M0,Mn);

% Calc thickness contribution
Kt = CalcKt(l,a0,a1,l1,l2,theta0,Kden,F(2),N0,Nn);

% Calc spoiler contribution
Ks = CalcKs(l,a0,a1,l1,l2,theta0,Kden,F(3),theta1,delta);

% Calc flap contribution
Kf = CalcKf(l,a0,a1,l1,l2,theta0,Kden,F(4),theta2,eta);

Kcomp = [Kalpha, Kc, Kt, Ks, Kf];

K = sum(Kcomp);

end

function Kden = CalcKden(l,a0,a1,l1,l2,theta0)
% Calculate the denominator of the cavition number K
%
% (c) R.R.M. Schildkamp, 2021

Kden = real( l * a1 * (1i * tmp_func1(l2,l1) * ...
    (tmp_func2(a0,theta0) + tmp_func2(a0,-theta0)) - ...
    1i * tmp_func1(l1,l2) * (1 + (1/(a0^2))) ));


% Local functions
    function y = tmp_func1(x1,x2)
        y = imag(x1) / (real(x1) * imag(x2) - imag(x1) * real(x2));
    end

    function y = tmp_func2(a,theta)
        y = exp(1i * theta) / (a * exp(1i * theta) - 1)^2;
    end

end

function K_alpha = CalcKalpha(l,a0,a1,l1,l2,theta0,Kden,alpha)
% Calculate incidence contribution to cavition number K
%
% (c) R.R.M. Schildkamp, 2021
```

```
55
56  K_alpha = 2 * real(l * a1 * (1i * (1 + (1 /(a0^2) ) ) * ...
57      alpha * tmp_func1(l1,l2) - 1i * (tmp_func2(a0,theta0) + ...
58      tmp_func2(a0,-theta0)) * alpha * tmp_func1(l2,l1))) / Kden;
59
60
61      function y = tmp_func1(x1,x2)
62          y = -real(x1) / (real(x1) * imag(x2) - imag(x1) * real(x2));
63      end
64
65      function y = tmp_func2(a,theta)
66          y = exp(1i * theta) / (a * exp(1i * theta) - 1)^2;
67      end
68
69  end
70
71  function Kc = CalcKc(l,a0,a1,l1,l2,theta0,Kden,Fc,M0,Mn,n)
72  % Calculate camber contribution to cavition number K
73  %
74  % (c) R.R.M. Schildkamp, 2021
75
76  % Check input
77  if nargin < 11
78      n = length(Mn);
79  end
80
81  % Convert int n to array from 1:n
82  n = 1:n;
83
84  Kc = 2 * real(l * a1 * (1i * (1 + (1 /(a0^2))) * ...
85      tmp_func1(l1,l2,Fc,M0) - 1i * (tmp_func2(a0,theta0) + ...
86      tmp_func2(a0,-theta0)) * tmp_func1(l2,l1,Fc,M0) + ...
87      sum((n .* Mn) ./ (a0.^(n+1)) ))) / Kden;
88
89      function y = tmp_func1(x1,x2,F,M)
90          y = (real(x1) * imag(-F) + real(x1) * 0.5 * M - ...
91              imag(x1) * real(-F)) /...
92              (real(x1) * imag(x2) - imag(x1) * real(x2));
93      end
94
95      function y = tmp_func2(a,theta)
96          y = exp(1i * theta) / (a * exp(1i * theta) - 1)^2;
97      end
98  end
99
100 function Kt = CalcKt(l,a0,a1,l1,l2,theta0,Kden,Ft,N0,Nn,n)
101 % Calculate thickness contribution to cavition number K
102 %
103 % (c) R.R.M. Schildkamp, 2021
104
105 % Check input
106 if nargin < 11
107     n = length(Nn);
108 end
109
110 % Convert int n to array from 1:n
```

```
111 n = 0:n;
112
113 % Add N0 to Nn
114 Nn = [N0, Nn];
115
116 Kt = 2 * real(l * a1 * (1i * (1 + (1 /(a0^2))) * ...
117     tmp_func1(l1,l2,Ft) - 1i * (tmp_func2(a0,theta0) + ...
118     tmp_func2(a0,-theta0)) * tmp_func1(l2,l1,Ft) + ...
119     sum(Nn .* ( (1-n)./a0 - tmp_func3(a0,theta0) - ...
120     tmp_func3(a0,-theta0) ) / (a0.^(n-1) * denom_func(a0,theta0) * ...
121     denom_func(a0,-theta0)) ) )) / Kden;
122
123 % Local functions
124     function y = tmp_func1(x1,x2,F)
125         y = (real(x1) * imag(-F) - imag(x1) * real(-F)) /...
126             (real(x1) * imag(x2) - imag(x1) * real(x2));
127     end
128
129     function y = tmp_func2(a,theta)
130         y = exp(1i * theta) / (a * exp(1i * theta) - 1)^2;
131     end
132
133     function y = tmp_func3(a,theta)
134         y = exp(1i * theta) / (a * exp(1i * theta) );
135     end
136
137     function y = denom_func(a,theta)
138         y = a * exp(1i * theta) - 1;
139     end
140
141 end
142
143 function Ks = CalcKs(l,a0,a1,l1,l2,theta0,Kden,Fs,theta1,delta)
144 % Calculate spoiler contribution to cavition number K
145 %
146 % (c) R.R.M. Schildkamp, 2021
147
148 Ks = 2 * real(l * a1 * (1i * (1 + (1 /(a0^2))) * ...
149     tmp_func1(l1,l2,Fs) - 1i * (tmp_func2(a0,theta0,2) + ...
150     tmp_func2(a0,-theta0,2)) * (tmp_func1(l2,l1,Fs) + ...
151      theta1 * sin(delta) / pi) + ...
152      sin(delta) / pi * (tmp_func3(a0,theta1) - ...
153      tmp_func3(a0,-theta1) ) )) / Kden;
154
155 % Local functions
156     function y = tmp_func1(x1,x2,F)
157         y = (real(x1) * imag(-F) - imag(x1) * real(-F)) /...
158             (real(x1) * imag(x2) - imag(x1) * real(x2));
159     end
160
161     function y = tmp_func2(a,theta,p)
162         y = exp(1i * theta) / (a * exp(1i * theta) - 1)^p;
163     end
164
165     function y = tmp_func3(a,theta)
166         y = 1 / (a - exp(1i * theta));
```

```
    end

end

function Ks = CalcKs(l,a0,a1,l1,l2,theta0,Kden,Fs,theta1,delta)
% Calculate spoiler contribution to cavition number K
%
% (c) R.R.M. Schildkamp, 2021

Ks = 2 * real(l * a1 * (1i * (1 + (1 /(a0^2))) * ...
    tmp_func1(l1,l2,Fs) - 1i * (tmp_func2(a0,theta0,2) + ...
    tmp_func2(a0,-theta0,2)) * (tmp_func1(l2,l1,Fs) + ...
     theta1 * sin(delta) / pi) + ...
     sin(delta) / pi * (tmp_func3(a0,theta1) - ...
     tmp_func3(a0,-theta1) ) )) / Kden;

% Local functions
    function y = tmp_func1(x1,x2,F)
        y = (real(x1) * imag(-F) - imag(x1) * real(-F)) /...
            (real(x1) * imag(x2) - imag(x1) * real(x2));
    end

    function y = tmp_func2(a,theta,p)
        y = exp(1i * theta) / (a * exp(1i * theta) - 1)^p;
    end

    function y = tmp_func3(a,theta)
        y = 1 / (a - exp(1i * theta));
    end

end
```

Listing B.15: *CalcConstantB0, eq.* (3.33).

```
function [B0, B0comp] = CalcConstantB0(l1,l2,K,F,alpha,M0)
% Calculate the components of constant B0
%
% (c) R.R.M. Schildkamp, 2021

B0alpha = CalcB0alpha(l1,l2,K(1),alpha);

B0c = CalcB0c(l1,l2,K(2),F(1),M0);

B0tsf = CalcB0tsf(l1,l2,K(3:5),F(2:4));

B0comp = [B0alpha, B0c, B0tsf];

B0 = sum(B0comp);

end

function B0alpha = CalcB0alpha(l1,l2,K,alpha)
% Calculate the incidence contribution to the constant B0.
%
% (c) R.R.M. Schildkamp, 2021

B0alpha = (-real(l1) * alpha + 0.5 * K * imag(l1)) / denom_func(l1,l2);
```

```
24
25 % Local function
26     function y = denom_func(x1,x2)
27         y = real(x1) * imag(x2) - imag(x1) * real(x2);
28     end
29
30 end
31
32 function B0c = CalcB0c(l1,l2,K,F,M0)
33 % Calculate the camber contribution to the constant B0.
34 %
35 % (c) R.R.M. Schildkamp, 2021
36
37 B0c = (real(l1) * (imag(-F) + 0.5 * M0) - imag(l1) * real(-F) + ...
38     0.5 * K * imag(l1) ) / denom_func(l1,l2);
39
40 % Local function
41     function y = denom_func(x1,x2)
42         y = real(x1) * imag(x2) - imag(x1) * real(x2);
43     end
44
45 end
46
47 function B0tsf = CalcB0tsf(l1,l2,K,F)
48 % Calculate the thickness, spoiler and aileron contributions to the
     constant B0.
49 %
50 % (c) R.R.M. Schildkamp, 2021
51
52 B0tsf = (real(l1) .* (imag(-F)) - imag(l1) .* real(-F) + ...
53     0.5 .* K .* imag(l1) ) ./ denom_func(l1,l2);
54
55 % Local function
56     function y = denom_func(x1,x2)
57         y = real(x1) * imag(x2) - imag(x1) * real(x2);
58     end
59
60 end
```

Listing B.16: *CalcConstantC0, eq.* (3.34).

```
1  function [C0, C0comp] = CalcConstantC0(l1,l2,B0,K,F)
2  % Calculate the components of constant C0
3  %
4  % (c) R.R.M. Schildkamp, 2021
5
6  C0alpha = CalcC0alpha(l1,l2,B0(1),K(1));
7
8  C0ctsf = CalcC0ctsf(l1,l2,B0(2:5),K(2:5),F(1:4));
9
10 C0comp = [C0alpha, C0ctsf];
11
12 C0 = sum(C0comp);
13
14 end
15
16 function C0alpha = CalcC0alpha(l1,l2,B0,K)
```

```
% Calculate the incidence contribution to the constant C0.
%
% (c) R.R.M. Schildkamp, 2021

C0alpha = (- B0 * real(l2) - 0.5 * K) ./ real(l1);

end

function C0ctsf = CalcC0ctsf(l1,l2,B0,K,F)
% Calculate the camber, thickness, spoiler and aileron contribution to the
    constant C0.
%
% (c) R.R.M. Schildkamp, 2021

C0ctsf = (-real(F) - B0 .* real(l2) - 0.5 .* K) ./ real(l1);

end
```

Listing B.17: *CalcLiftCoefficient, eq.* (3.38).

```
function [CL, CLcomp] = CalcLiftCoefficientCL(l,a0,a1,theta0,theta1,theta2
    ,Mn,N0,Nn,B0,C0,chord,delta,eta)
% Calculate the components of the lift coefficient.
%
% (c) R.R.M. Schildkamp, 2021
% Incidence
CLalpha = CalcCLalpha(l,a0,a1,theta0,B0(1),C0(1),chord);

% Camber
CLc = CalcCLc(l,a0,a1,theta0,B0(2),C0(2),chord,Mn);

% Thickness
CLt = CalcCLt(l,a0,a1,theta0,B0(3),C0(3),chord,N0,Nn);

% Spoiler
CLs = CalcCLs(l,a0,a1,theta0,theta1,B0(4),C0(4),chord,delta);

% Flap
CLf = CalcCLf(l,a0,a1,theta0,theta2,B0(5),C0(5),chord,eta);

% Output
CLcomp.CLalpha = CLalpha;
CLcomp.CLc = CLc;
CLcomp.CLt = CLt;
CLcomp.CLs = CLs;
CLcomp.CLf = CLf;

CL = sum([CLalpha, CLc, CLt, CLs, CLf]);

end

function CLalpha = CalcCLalpha(l,a0,a1,theta0,B0,C0,chord)
% Calculate the incidence contribution to the lift coefficient.
%
% (c) R.R.M. Schildkamp, 2021

CLalpha = 4 * pi / chord * imag(1i * B0 * l * a1 * (1 + (1 /(a0^2))) - ...
```

```
37      1i * C0 * l * a1 * (tmp_func(a0,theta0) + tmp_func(a0,-theta0) ) );
38
39  % Local functions
40      function y = tmp_func(a,theta)
41          y = exp(1i * theta) / (a * exp(1i * theta) - 1)^2;
42      end
43
44  end
45
46  function CLc = CalcCLc(l,a0,a1,theta0,B0,C0,chord,Mn,n)
47  % Calculate the camber contribution to the lift coefficient.
48  %
49  % (c) R.R.M. Schildkamp, 2021
50
51  % Check input
52  if nargin < 9
53      n = length(Mn);
54  end
55
56  n = 1:n;
57
58
59  CLc = 4 * pi / chord * imag(1i * B0 * l * a1 * (1 + (1 /(a0^2))) - ...
60      1i * C0 * l * a1 * (tmp_func(a0,theta0) + tmp_func(a0,-theta0)) + ...
61      1i * l * a1 * sum( (n .* Mn) ./ (a0.^(n+1)) ) );
62
63  % Local functions
64  function y = tmp_func(a,theta)
65          y = exp(1i * theta) / (a * exp(1i * theta) - 1)^2;
66      end
67
68  end
69
70  function CLt = CalcCLt(l,a0,a1,theta0,B0,C0,chord,N0,Nn,n)
71  % Calculate the thickness contribution to the lift coefficient.
72  %
73  % (c) R.R.M. Schildkamp, 2021
74
75  % Check input
76  if nargin < 10
77      n = length(Nn);
78  end
79
80  n = 0:n;
81
82  Nn = [N0, Nn];
83
84  CLt = 4 * pi / chord * imag(1i * B0 * l * a1 * (1 + (1 /(a0^2))) - ...
85      1i * C0 * l * a1 * (tmp_func1(a0,theta0) + ...
86      tmp_func1(a0,-theta0)) + ...
87      1i * l * a1 * sum(Nn .* ( (1-n)./a0 - tmp_func2(a0,theta0) - ...
88      tmp_func2(a0,-theta0)) ./ (a0.^(n-1) * denom_func(a0,theta0) * ...
89      denom_func(a0,-theta0) ) ) );
90
91  % Local functions
92      function y = tmp_func1(a,theta)
```

```
93          y = exp(1i * theta) / (a * exp(1i * theta) - 1)^2;
94      end
95
96      function y = tmp_func2(a,theta)
97          y = exp(1i * theta) / (a * exp(1i * theta));
98      end
99
100     function y = denom_func(a,theta)
101         y = a * exp(1i * theta) - 1;
102     end
103
104 end
105
106 function CLs = CalcCLs(l,a0,a1,theta0,theta1,B0,C0,chord,delta)
107 % Calculate the spoiler contribution to the lift coefficient.
108 %
109 % (c) R.R.M. Schildkamp, 2021
110
111 CLs = 4 * pi / chord * imag(1i * B0 * l * a1 * (1 + (1 / (a0^2) ) ) - ...
112     1i * (C0 + theta1 * sin(delta) / pi) * ...
113     l * a1 * (tmp_func1(a0,theta0) + tmp_func1(a0,-theta0) ) + ...
114     sin(delta) / pi * l * a1 * (tmp_func2(a0,theta1) - ...
115     tmp_func2(a0,-theta1)));
116
117 % Local functions
118     function y = tmp_func1(a,theta)
119         y = exp(1i * theta) / (a * exp(1i * theta) - 1)^2;
120     end
121
122     function y = tmp_func2(a,theta)
123         y = 1 / (a - exp(1i * theta));
124     end
125
126 end
127
128 function CLf = CalcCLf(l,a0,a1,theta0,theta2,B0,C0,chord,eta)
129 % Calculate the aileron contribution to the lift coefficient.
130 %
131 % (c) R.R.M. Schildkamp, 2021
132
133 CLf = 4 * pi / chord * imag(1i * B0 * l * a1 * (1 + (1 /(a0^2))) - ...
134     1i * (C0 + (theta2 - pi) * eta / pi) *...
135     l * a1 * (tmp_func1(a0,theta0) + tmp_func1(a0,-theta0)) + ...
136     eta / pi * l * a1 * (tmp_func2(a0,theta2) -...
137     tmp_func2(a0,-theta2)));
138
139 % Local functions
140     function y = tmp_func1(a,theta)
141         y = exp(1i * theta) / (a * exp(1i * theta) - 1)^2;
142     end
143
144     function y = tmp_func2(a,theta)
145         y = 1 / (a - exp(1i * theta));
146     end
147
148 end
```